Review Article

Klimarealistene
Vollsveien 109
1358 Jar
Norway
ISSN: 2703-9072

Correspondence:
roy.clark@ventura-photonics.com

Vol. 4.1 (2024)
pp. 1-73

A Nobel Prize for Climate Model Errors

Roy Clark

Ventura Photonics,
Thousand Oaks, CA, USA

Abstract

When the Royal Swedish Academy of Sciences awarded part of the 2021 Nobel Prize for Physics to Syukuro Manabe they failed to recognize that the climate models used to justify the award were invalid. When the CO_2 concentration was increased in the 1967 model developed by Manabe and Wetherald it created warming as a mathematical artifact of the simplistic steady state energy transfer assumptions that they used. The initial temperature increase was then amplified by a second artifact, the assumption of a fixed relative humidity distribution that created a water vapor feedback. When the CO_2 concentration was doubled from 300 to 600 parts per million (ppm), the 1967 model predicted an increase in equilibrium surface temperature of 2.9 °C for clear sky conditions. The equilibrium temperature increase produced by a CO_2 doubling later became known as the equilibrium climate sensitivity (ECS). The algorithms used in the 1967 model were incorporated into their 1975 global circulation model (GCM). This also had an ECS of 2.9 °C. The steady state assumption provided the foundation for the concept of radiative forcing. The water vapor feedback became part of a set of feedbacks that were used to adjust the radiative forcings. The ECS produced by the 1967 model artifacts provided a benchmark for the temperature increases to be expected in future climate models. The invalid concepts of radiative forcings, feedbacks and climate sensitivity were accepted by the UN Intergovernmental Panel on Climate Change (IPCC) and have been used in all six of the IPCC Climate Assessment Reports. A thermal engineering analysis of the interactive, time dependent surface energy transfer processes that determine the surface temperature demonstrates that it is impossible for the observed increase in atmospheric CO_2 concentration since 1800 to have caused any unequivocal change in surface temperature.

Keywords: Anthropogenic Forcing; Climate Model; Climate Sensitivity; Extreme Weather; Global Mean Temperature Record; Mission Creep; Nobel Prize; Radiative Forcing; Slab Ocean; Syukuro Manabe; Thermal Equilibrium; Time Dependent Energy Transfer; Time Integration; Water Vapor Feedback.

Submitted 2024-02-05, Accepted 2024-03-02. https://doi.org/10.53234/SCC202404/17

1. Introduction

The invalid concepts of radiative forcing, feedbacks and climate sensitivity used by the UN Intergovernmental Panel on Climate Change (IPCC) can be traced back to Table 5 of the climate modeling paper published by Manabe and Wetherald (1967). Here they claimed that a doubling of the CO_2 concentration from 300 to 600 ppm would produce an increase in the equilibrium surface temperature of the earth of 2.9 °C for clear sky conditions. A closer examination reveals that this number was largely a mathematical artifact produced by using a highly simplified one dimensional radiative convective (1-D RC) computer model. Manabe and Wetherald (M&W) failed to correct the obvious simplification errors in this paper and spent the next eight years incorporating the 1967 model algorithms into every unit cell of a highly simplified global circulation model (GCM), Manabe and Wetherald (1975). They also failed to understand that the errors associated with the numerical solution of large numbers of coupled non-linear equations used in a GCM could grow over time and seriously compromise the predictive capabilities of such a model. These issues were described by Lorenz (1963).

As funding was reduced for space exploration and later for nuclear programs, there was mission creep at various US government agencies. The steady state air column was copied by other modeling groups seeking an alternate source of funding, notably the planetary atmospheres group at NASA, Hansen et al (2000). In 1976, the NASA Goddard group copied the 1967 M&W model and created warming artifacts for ten other molecules including methane (CH_4) and nitrous oxide (N_2O), Wang et al (1976). Later, Hansen et al (1981) added a simple two layer slab ocean to the 1967 model. They ignored the wind driven evaporation at the ocean surface and assumed, incorrectly, that the ocean could be heated by a small increase in the downward long wave IR (LWIR) flux at the surface, Clark and Rörsch (2023). The slab ocean was a flat ocean without wind or waves. Hansen et al then tuned this model to simulate a global temperature record from 1880 to 1980 using a combination of increased CO_2 concentration, changes in volcanic aerosol levels and variations in the solar flux. The 1981 Hansen et al paper is one of the earliest examples of the use of a contrived set of radiative perturbations, later called radiative forcings, to tune an equilibrium climate model to match the global average temperature record.

Hansen et al also ignored the obvious 1940 peak in their global temperature record. They assumed that recent warming was caused by the increase in CO_2 concentration. In reality, there can be no CO_2 signal in the global temperature record. The observed warming may be explained as a combination of four factors. First, the dominant term, especially in the early record, is ocean oscillations, mainly the contribution from the Atlantic Multidecadal Oscillation (AMO), Akasofu (2010). Second, there are urban heat islands related to population growth that were not part of the earlier record. Third, the mix of urban and rural weather stations used to create the global record has changed. Fourth, there are so called 'homogenization' adjustments that have been made to the raw temperature data. These include the infilling of missing data and adjustments to correct for bias related to changes in weather station location and instrumentation. It has been estimated that half of the warming in the global record has been created by such adjustments. This has been considered in more detail for example by Andrews (2001a; 2017b; and 2017c), D'Aleo and Watts (2010), Berger and Sherrington (2022) and O'Neill et al (2022).

As funding for nuclear programs was reduced, mission creep spread to the Atomic Energy Commission that became part of the US Department of Energy (DOE) in 1977. An extensive report of the work on CO_2 at DOE was published in 1985 (Riches and Koomanoff, 1985; MacCracken and Luther 1985a; 1985b). The issue was how to detect the CO_2 signal in the surface air temperature record. This work gradually evolved into the Climate Model Intercomparison Project (CMIP) that became the major source of climate model results used by the IPCC. Later, in the Third Climate Assessment Report published by the UN Intergovernmental Panel on Climate change (IPCC, 2001) the radiative forcings were split into anthropogenic and natural contributions. This approach was used to claim that increases in atmospheric greenhouse gas concentrations could cause an increase in the frequency and intensity of extreme weather events.

Manabe and his group failed to recognize and correct the errors in their early climate models. They provided the foundation for the radiative forcings, feedbacks and climate sensitivities still used in the climate models today, IPCC (2021).

Section 2 gives a general description of the early development of the equilibrium models. Section 3 provides a more detailed technical analysis of selected models. Section 4 explains the energy transfer processes that determine the surface temperature and the simplification errors introduced by the climate models. Section 5 considers climate change over time including the influence of ocean oscillations and the limitations of a global mean temperature.

2. The Early Development of the Equilibrium Climate Models

Starting in the early 1960s, Manabe's group at the US Weather Bureau began the development of a GCM for climate prediction. This work is described in four main papers, Manabe and Möller (1961), Manabe and Strickler, (1964), Manabe and Wetherald, (1967) and Manabe and Wetherald (1975). For convenience these are abbreviated as MM61, MS64, MW67 and MW75. The first step was to develop a radiative transfer model that could simulate the atmospheric temperature profile. MM61 started with a one dimensional (1-D) radiative equilibrium model. MS64 was a 1-D radiative convective (1-D RC) model with a fixed absolute humidity profile. MW67 added a fixed relative humidity profile to MS64 and MW75 was a 'highly simplified' GCM that incorporated the MW67 algorithms into each unit cell of the larger model.

2.1 The 1967 Manabe and Wetherald Model

The set of assumptions used in the MW67 steady state air column model were clearly stated on the second page of the paper:

1) *At the top of the atmosphere, the net incoming solar radiation should be equal to the net outgoing long wave radiation.*
2) *No temperature discontinuity should exist.*
3) *Free and forced convection and mixing by the large scale eddies prevent the lapse rate from exceeding a critical lapse rate equal to 6.5 °C* km^{-1}.
4) *Whenever the lapse rate is subcritical, the condition of local radiative equilibrium is satisfied.*
5) *The heat capacity of the earth's surface is zero.*
6) *The atmosphere maintains the given vertical distribution of relative humidity (new requirement).*

The questions that M&W set out to answer were:

1) *How long does it take to reach a state of* ***thermal equilibrium*** *when the atmosphere maintains a realistic distribution of relative humidity that is invariant with time?*
2) *What is the influence of various factors such as the solar constant, cloudiness, surface albedo and the distributions of various atmospheric absorbers on the* ***equilibrium temperature*** *of the atmosphere with a realistic distribution of relative humidity?*
3) *What is the* ***equilibrium temperature*** *of the earth's surface corresponding to realistic values of these factors?*

The MW67 model was a mathematical platform for the development of radiative transfer and related algorithms that could be incorporated into a larger global circulation model. Given the limited spectral data that were available to M&W in 1967, the radiative transfer algorithms were quite reasonable. However, a single radiative transfer analysis only provides a snapshot of the atmospheric LWIR flux and the rates of heating and cooling for the temperature and species profiles specified in the calculation. There were two distinct temperature artifacts in the MW67 calculations. First, the steady state assumption required that the model warm up when the CO_2 concentration was increased so that the flux balance was restored at the top of the model atmosphere. Second, the fixed relative humidity assumption created a water vapor feedback that amplified the initial CO_2 warming. In addition, the time integration algorithm assumed that the small temperature changes calculated at each integration step could accumulate over time.

M&W did not consider the effects of molecular collisions and turbulence in the troposphere. Here, the additional photon energy absorbed by the increase in CO_2 concentration is transferred to the local air parcel as heat. This is then dissipated by wideband LWIR emission that maintains the flux balance at TOA. They also neglected the diurnal temperature and humidity variations related to the solar heating of the surface. These energy transfer processes are discussed in more detail in Section 4.

The equilibrium or steady state climate model was introduced by Arrhenius (1896), A96. He started with a uniform air volume at a single temperature. He also used a fixed average solar flux, a partially reflective blackbody surface with zero heat capacity and imposed an exact flux balance at the top of the model atmosphere (TOMA). When the CO_2 concentration is increased, there is a small increase in the LWIR flux to the surface and a similar decrease in the LWIR emission to space within the spectral region of the CO_2 emission bands. Arrhenius simply increased the surface temperature to restore the flux balance at TOMA. However, in the real atmosphere, any surface temperature changes that might be produced by a change in the atmospheric CO_2 concentration are too small to detect in the normal daily and seasonal temperature variations at the surface and in the adjacent turbulent boundary layer, Clark and Rörsch (2023).

M&W copied the main features of the Arrhenius model and added a 9 or 18 layer radiative transfer algorithm. Three molecules were included in the radiative transfer analysis: carbon dioxide, CO_2, water vapor, H_2O and ozone, O_3. Both LWIR absorption/emission and shorter wavelength solar absorption were calculated. The model was illuminated by a 24-hour average solar flux. The surface was a partially reflective blackbody with zero heat capacity. The magnitude of the lapse rate (vertical tropospheric temperature profile) was constrained so that it did not exceed 6.5 °C per kilometer. The relative humidity (RH) profile for the air layers was also fixed. The temperatures of the surface and air layers were adjusted iteratively until the model reached a steady state in which the temperatures were stable and the LWIR flux emitted at TOMA matched the net incoming solar flux. As various model parameters, such as the solar intensity and the surface reflectivity were varied, the steady state temperature profile was similar to an average of measured values. This was sufficient for M&W to claim that this model could simulate an equilibrium temperature of the earth. However, such a temperature is just a mathematical construct, Essex et al (2007). There is no steady state air column in the real atmosphere and both turbulent moist convection and subsurface thermal storage have to be included in the time dependent surface energy transfer analysis. Under clear sky conditions, almost all of the downward LWIR flux from the lower troposphere to the surface originates from within the first 2 km layer. (At an altitude of 2 km, the pressure is approximately 800 mbar). Almost half of this flux comes from within the first 100 m layer (Clark, 2013a; 2013b; Clark and Rörsch, 2023).

M&W extended the normal radiative transfer calculation of the LWIR flux to include the rate of cooling (or heating) at each level in their model. The net LWIR flux at each level was divided by the heat capacity to give the cooling (or heating) rate. This was multiplied by the time step, usually set to 8 hours, to derive the change in temperature for each air layer. These small temperature changes were then added to the start temperatures and the iteration procedure was repeated for the next step. The MW67 model required about a year of iteration time (time step multiplied by the number of iterations) to reach steady state (see Fig. 4c). For a CO_2 doubling from 280 to 560 ppm, modern radiative transfer calculations for low to mid latitudes give an initial decrease in the tropospheric cooling rate of up to +0.08 K per day, Iacono et al (2008). This is approximately +0.027 K per 8-hour time step (see Fig. 21c). These iterative temperature steps decrease as the model integration proceeds. In the real atmosphere, such small temperature changes cannot accumulate in the normal daily and seasonal temperature cycles.

The fixed RH assumption now added a water vapor feedback that amplified the initial CO_2 warming artifact. Relative humidity is defined as a fraction of the saturated water vapor pressure. As the temperature increases, the saturated water vapor pressure also increases. This produced an increase in the water vapor pressure in the air layers in MW67 even though the RH distribution was fixed. The resulting increases in LWIR flux related to the water vapor concentration amplified the temperature needed to reach the imposed steady state condition in MW67. This water vapor feedback led to the 2.9 K (or °C) model result. For a fixed absolute humidity, the corresponding model temperature rise was 1.36 K. In the real atmosphere near the surface there is no fixed RH, Clark and Rörsch (2023). At fixed absolute humidity, the changes in temperature over the diurnal cycle change the RH. In addition, evaporation changes the absolute humidity (see Fig. 34). Local conditions also change day by day as different weather systems pass through (see Fig. 36).

M&W failed to understand and correct their own errors and went on to incorporate the algorithms from MW67 into every unit cell of the 'highly simplified' MW75 GCM. When the atmospheric CO_2 concentration was doubled in MW75 the average increase in surface temperature was 2.93 °C. This should be compared to the 2.36 °C increase for average cloudiness conditions in MW67. This provided an invalid warming benchmark for the climate models developed by other groups. The 1979 Charney Report claimed an increase in temperature of 3 ±1.5 °C for a doubling of the CO_2 concentration, Charney et al (1979). In addition to model simplifications, there was another calculation issue that was introduced in MW75. A GCM requires the solution to large numbers of coupled nonlinear equations. Such solutions are unstable and the climate GCMs have limited predictive capabilities over the time scales used in climate studies (Lorenz, 1973; 1963). These issues were minimized in MW75 because the model was run to a steady state condition over a 2-year model time period for CO_2 concentrations of 300 and 600 ppm.

2.2 Mission Creep at NASA

Outside events now intervened. Mission creep at NASA started when funding was reduced significantly as the Apollo (moon landing) program ended in 1972. Those modeling planetary atmospheres at NASA were told to switch to earth studies, Hansen et al (2000). Melodramatic claims about climate change related to runaway greenhouse effects or air pollution were used to justify the extension of their radiative transfer studies to the earth's atmosphere. They did not conduct any independent model validation and started to use the steady state air column approach.

During the 1970s there was a global cooling scare related to the cooling phase of the Atlantic Multi-decadal Oscillation (AMO) that was coupled to the weather station record (Akasofu, 2010; Douglas, 1975). Ocean cooling was not part of the climate change narrative, so Rasool and Schneider (1971) claimed that an increase in aerosol concentration could over-ride any CO_2 induced warming and produce atmospheric cooling. If this continued, then it could trigger an Ice Age. This was based on the results from a 1-D steady state climate model. At the time, both authors were with NASA Goddard.

Ramanathan (1975) at NASA Langley then claimed a greenhouse effect or a warming for an increase in the atmospheric concentration of chlorofluorocarbons (CFCs). When the atmospheric CFC concentration was increased in his 1-D model, there was a decrease in LWIR flux at TOMA. It was claimed that this perturbed the climate equilibrium state and produced an increase in surface temperature. Later, this was recognized as the first use of radiative forcing, Ramaswamy et al (2019). The effects of molecular line broadening and surface temperature variations were not considered (see Section 4.1). In 1976, a group at NASA Goddard including Hansen, extended the MW67 1-D RC model to include another 8 minor species, N_2O, CH_4, NH_3, HNO_3, C_2H_4, SO_2, CH_3Cl and CCl_4. They also included the CFCs analyzed by Ramanathan and the original molecules, CO_2, H_2O and O_3 from MW67, Wang et al (1976), H76.

The slab ocean, the step CO_2 doubling and the calculation of a global mean temperature record were added to the 1-D RC model calculations by Hansen et al, (1981), H81. They began by tuning their model so that a CO_2 doubling from 300 to 600 ppm produced an increase in temperature of 2.8 °C. Then they introduced a slab ocean model with a mixed ocean layer 100 m thick and a thermocline layer below this. The surface energy transfer was ignored and only the time delays related to the increase in heat capacity were considered. The penetration depth of the LWIR flux into the oceans is less than 100 micron, Hale and Querry (1973). Here it is fully coupled to the wind driven evaporation or latent heat flux. The large wind driven variations in the latent heat flux overwhelm any possible heating effects produced by the increase in LWIR flux related to a CO_2 doubling, Clark and Rörsch (2023). The slab ocean was a flat ocean without wind or waves.

The H81 model was then used to calculate changes in surface temperature using a variety of forcing agents including greenhouse gases, clouds and aerosols. This was an extension of the work started in H76. The step CO_2 doubling was then introduced. The CO_2 concentration was first doubled in the 1-D RC model from 300 to 600 ppm. This produces a small decrease in the upward LWIR flux emitted to space at TOA and a small increase in the downward LWIR flux to the surface. After a few months, the H81 model stratosphere cooled by ~5 °C and the decrease in

LWIR flux at TOA was 3.8 W m^{-2}. The energy gained was used to warm the oceans. Years later, the surface temperature increased by 2.8 °C. Of this, 1.2 °C was produced by the increase in CO_2 concentration and the rest was from feedbacks. In reality, all of this is too small to detect in the normal daily and seasonal temperature variations near the surface and cannot accumulate over time. At present the annual increase in the average CO_2 concentration is near 2.4 ppm and the change in flux is 0.034 W m^{-2} per year, Harde (2017). At low pressures and temperatures in the stratosphere, there is increased cooling, but any flux changes here are small and do not propagate to the surface because of molecular line broadening at lower altitudes.

Available weather station and related data were combined and averaged into a global mean temperature record. The obvious large peak near 1940 created by the warming phase of the AMO was ignored, AMO (2022). The H81 model was 'tuned' to simulate the global temperature record. A combination of increased CO_2, solar variation and volcanic aerosols was used to fit the climate model output to the temperature record. The H81 paper is one of the earliest examples of the use of a contrived set of radiative perturbations, later called radiative forcings to tune an equilibrium climate model to match the global average temperature record.

A global average temperature is not a good measure of climate. Temperature is an intensive thermodynamic property. The temperature sum of two independent thermodynamic systems is simply a number, so is the average. A global average temperature is a mathematical construct that has no physical meaning. The temperature anomaly obtained by subtracting the mean from a time series of global temperatures is just a number series. This is discussed in detail by Essex et al (2007). Climate and climate change should be analyzed using a zonal climate approach based on the Koppen Geiger or similar classification, Kottek et al (2006). This is considered in more detail in Section 5.

Later, Hansen et al (1984), H84, applied electronic feedback theory to equilibrium climate modeling. The concept of radiative forcing was accepted by the UN Intergovernmental Panel on climate Change (IPCC) and has been used in all of the IPCC climate assessment reports, Ramaswamy (2019). None of the work at NASA was challenged by Manabe's group. They accepted the flat ocean model and calculated an ocean warming of 3.2 K in a mixed ocean layer produced by a 4x increase in CO_2 concentration (Manabe and Stouffer 1979; 1980).

2.3 The Growth of the Climate Models

As computer technology improved, the climate models became more complex, but the equilibrium climate assumption was still there, hidden in the unit cells of the GCMs. A global average planetary energy balance was used instead of the exact flux balance at TOMA in a 1-D model. However, the initial decrease in LWIR flux at TOA produced by an increase in greenhouse gas concentration still changed the energy balance of the earth, Knutti and Hegerl (2008). A greenhouse gas radiative forcing could still heat the oceans. More forcing agents were added to the climate models and the changes over time were adapted so that the global average temperature record generated by the models matched the one derived from the weather station data. Both are just number series that contain almost no information on climate change. More feedback mechanisms were also added so that the models could be tuned to give any desired result. Effective radiative forcings were introduced by Hansen et al (2005). These just added additional tuning to the climate models. The models were compared to each other using the equilibrium climate sensitivity (ECS) to a CO_2 doubling as a benchmark. The MW67 model had an ECS of 2.9 °C for clear sky conditions. The H81 model was tuned to an ECS of 2.8 °C. For the Sixth IPCC Climate Assessment, AR6 (2021), the ECS range for models in the sixth phase of the Climate Model Intercomparison Project (CMIP6) ensemble is from 1.8 to 5.6 °C, Zelinka et al (2020).

As funding for nuclear programs was reduced, mission creep spread to the Atomic Energy Commission that became part of the US Department of Energy (DOE) in 1977. An important part of the DOE climate research program has been model intercomparison. The Program for Climate Model Diagnosis and Intercomparison (PCMDI) was established at Lawrence Livermore National Laboratory (LLNL) in 1990. One of the early intercomparison efforts was the Atmospheric Model

Intercomparison Project (AMIP), Gates (1992). The Coupled Model Intercomparison Program (CMIP) started in 1996, Meehl et al (1997). Various phases of this program have been a major source of the climate model results used by the IPCC. The CMIP3 model results were used for the Fourth IPCC Climate Assessment Report, AR4, (IPCC, 2007: Meehl et al, 2007). The CMIP5 results were used for the Fifth IPCC Climate Assessment Report, AR5 (IPCC, 2013; Taylor et al, 2012) and the CMIP6 results were used for the Sixth IPCC Climate Assessment Report, AR6, (IPCC, 2021; Stouffer et al, 2017; Hausfather, 2019).

There was a significant change in the climate modeling approach that started with the Third IPCC Climate Assessment Report, TAR (2001). The time series of radiative forcings used to simulate the global mean temperature record was split into natural and anthropogenic forcings. The climate models were then rerun to create a separate natural baseline and an anthropogenic contribution to the global mean temperature. A vague statistical argument using changes to the normal distribution ('bell' or Gaussian curve) of temperature was then used to claim that the increase in temperature caused by anthropogenic forcings would cause an increase in the frequency and intensity of extreme weather events (see Section 3.5). This extreme weather argument has been incorporated into all of the later IPCC Climate Assessment Reports (see Figs. 14d through 14g and Sections 3.5 and 3.6).

3. Equilibrium Climate Models: A More Detailed Analysis

3.1 The 1967 Manabe and Wetherald Model (MW67)

The data from tables 4 and 5 of Manabe and Wetherald's 1967 paper, MW67, are shown in Figs. 1a and 1b. The increase in surface temperature for a CO_2 doubling from 300 to 600 ppm is claimed to be 2.9 K (°C) for clear sky conditions for a fixed RH distribution. The temperatures and the temperature changes for a CO_2 doubling from 300 to 600 ppm are circled in red.

a) Table 4: Equilibrium temperature of the earth's surface (K) and the CO_2 content of the atmosphere

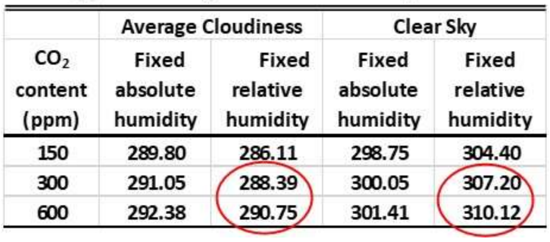

	Average Cloudiness		Clear Sky	
CO_2 content (ppm)	Fixed absolute humidity	Fixed relative humidity	Fixed absolute humidity	Fixed relative humidity
150	289.80	286.11	298.75	304.40
300	291.05	288.39	300.05	307.20
600	292.38	290.75	301.41	310.12

b) Table 5: Change of equilibrium temperature of the earth's surface corresponding to various changes of CO_2 content of the atmosphere

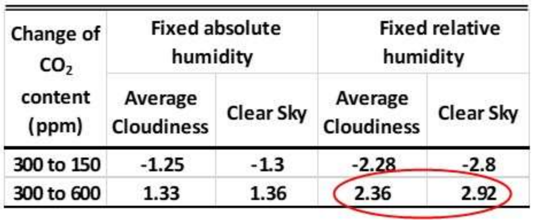

Change of CO_2 content (ppm)	Fixed absolute humidity		Fixed relative humidity	
	Average Cloudiness	Clear Sky	Average Cloudiness	Clear Sky
300 to 150	-1.25	-1.3	-2.28	-2.8
300 to 600	1.33	1.36	2.36	2.92

Figure 1: Tables 4 and 5 adapted from MW67 showing the temperatures and temperature changes produced by doubling the CO_2 concentration from 300 to 600 ppm.

The basic steady state assumptions used by M&W were the same as those used by Arrhenius in 1896. These included a fixed, average solar flux and a partially reflective blackbody surface with zero heat capacity. The effects of advection, evaporation, subsurface thermal storage and ocean transport were ignored. The Arrhenius model is illustrated in Fig. 2. (Modern symbols for Stefan's constant, σ, and the surface emissivity, ε, are used). Because of the simplifications introduced, the surface temperature depends only on the surface emissivity ε and the air column LWIR absorption β (A96, Eqn. 3). The results obtained by Arrhenius for the average annual temperature changes vs. latitude for relative CO_2 concentrations of 0.67, 1.5, 2.0, 2.5 and 3.0 are shown in Fig. 3.

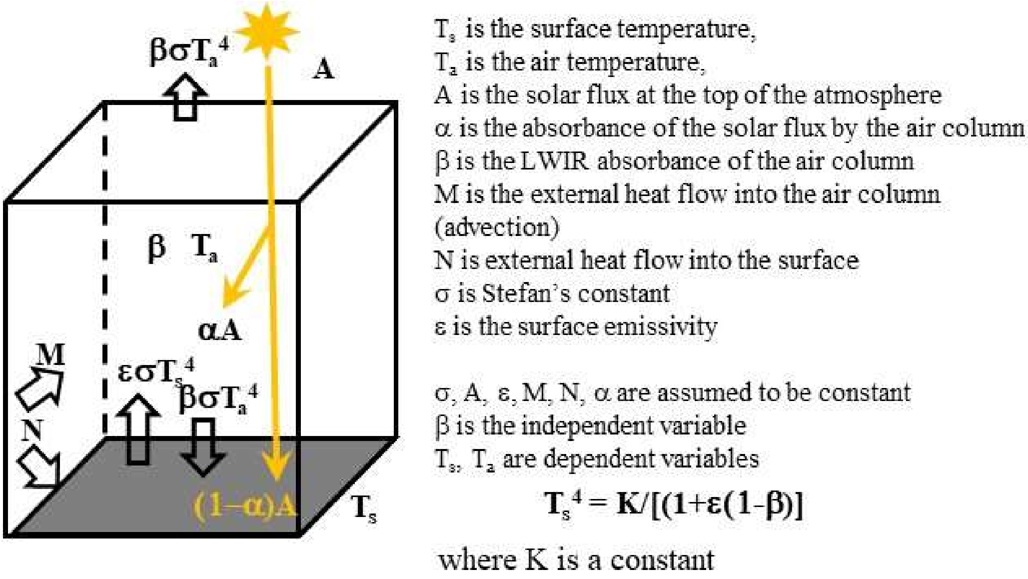

Figure 2: The 1896 Arrhenius steady state model.

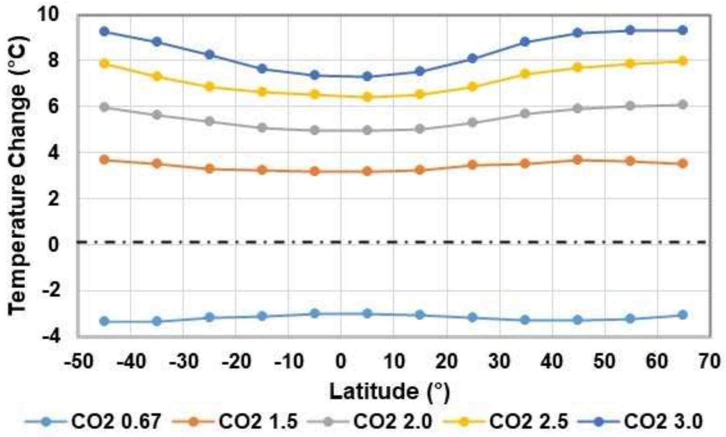

Figure 3: Annual average temperature changes vs. latitude for selected CO_2 concentrations from Arrhenius, 1896, Table VII.

The MW67 model configuration for 9 layers is illustrated in Fig. 4a. The incident solar flux at TOA for a given model run was fixed. The default was 2 Langley per minute (~1395 W m^{-2}). This was converted to a 24 hour average value (see MS64, pp. 367-368). The Langley (Ly) is an older unit of heat per unit area, 1 Ly = one calorie or 4.186 Joules per square centimeter. The surface was a partially reflective blackbody with zero heat capacity. The outline of the time marching or integration procedure is shown in Fig. 4b (MW67, fig.2). Starting from the top right box, the radiative transfer calculation was used to determine the changes in temperature for each layer during the model time step. This was usually 8 hours. The temperature changes were then added to the temperatures at the start of the step. If necessary, the model was forced to maintain the lapse rate at 6.5 K km^{-1}. The water vapor concentration was then adjusted for the new temperatures. The iteration was repeated until the model reached a steady state where the temperatures were stable and the LWIR flux at TOMA matched the net solar flux. The MW67 model required approximately one year of iteration time (step time multiplied the number of steps) to reach a steady state as shown in Fig. 4c (data from MW67, fig. 6). The computational time was much less.

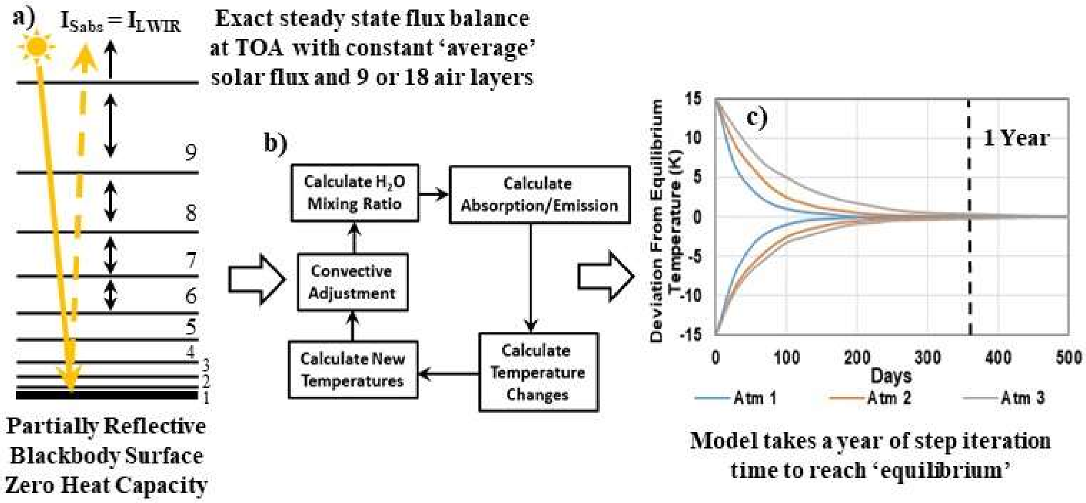

Figure 4: a) The MW67 model configuration (9 air layers shown) with a fixed average solar flux and a partially reflective blackbody surface with zero heat capacity. b) Outline of the 'time marching procedure' used to drive the MW67 model to a steady state condition where the net solar flux equals the LWIR flux at the top of the model atmosphere and the air layer temperatures are stable. c) The time required for the model to reach a steady state.

The tropospheric RH distribution used in MW67 was derived in part from the latitude-height summer and winter averages shown in Fig. 5a (data from MW67, fig, 1). The derived RH profile, h, is shown in Fig. 5b (data from MW67, fig. 3). The linear function for h vs. altitude is given in the text box. The default value for the surface RH, h*, is 0.77 (77%). The surface pressure is set to 1000 mbar. At low pressures in the stratosphere, the H_2O mixing ratio is set to a fixed value of 3 x 10^{-6} gm gm^{-1} air (grams of water vapor per gram of air). The vertical distributions of radiative convective temperature for h* values of 0.2, 0.6 and 1.0 (20%, 60% and 100%) are shown in Fig. 5c (data from MW67, fig. 11). The equilibrium surface temperature increases from approximately 280 to 300 K as h* increases from 0.2 to 1.0. Under clear sky conditions, almost all of the downward LWIR flux to the surface originates from within the first 2 km layer above the surface (see Fig. 19c, below). An altitude of 2 km is close to the 800 mbar level. Approximately half of this flux comes from the first 100 m layer closest to the surface. The 2 km or 800 mbar level is indicated by the blue dashed line in Fig. 5.

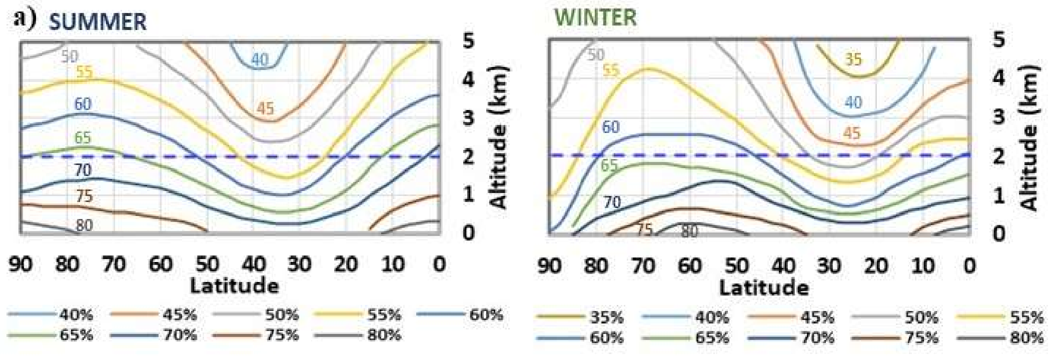

Fig. 1. Latitude-height distribution of relative humidity for both summer and winter (Telegadas and London, 1953)

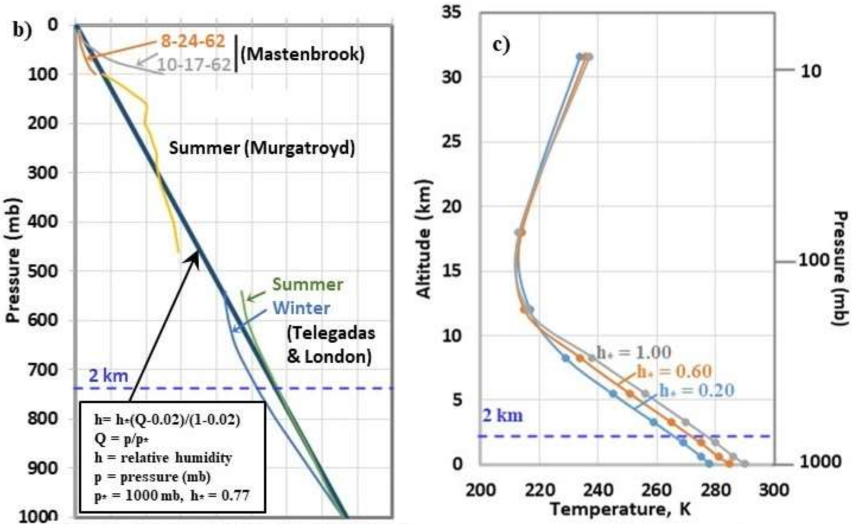

Fig. 3. Vertical distribution of relative humidity

Fig. 11. Vertical distribution of radiative convective equilibrium temperature for various distributions of relative humidity

Figure 5: *a) The latitude-height distributions of relative humidity up to 5 km used to determine the fixed RH distribution for MW67, b) the relative humidity profile used by MW67 and c) the vertical distribution of radiative convective temperature for surface RH (h_*) values of 0.2, 0.6 and 1.0 (20%, 60% and 100% RH). Almost all of the downward LWIR flux from the lower troposphere to the surface originates from within the 2 km layer indicated by the dashed blue line.*

Fig. 6a (data from MW67, fig. 8) shows the steady state temperature profiles for selected values of the solar constant. The table, inset gives the values for the solar constant in Langley per minute and in W m^{-2} and the corresponding equilibrium surface temperatures (K). Fig. 6b (data from MW67, fig. 19) shows the steady state temperature profiles for selected values of the surface albedo. The table, inset gives the values for the albedo and the corresponding equilibrium surface temperature. The results shown in Figs. 5 and 6 were accepted by M&W as sufficient to validate their equilibrium or steady state model.

Fig. 7 (data from MW67, fig. 16) shows the effect of doubling and halving the atmospheric CO_2 concentration in the MW67 model from 300 ppm. In the troposphere, an increase in CO_2 concentration from 300 to 600 ppm produces a slight increase in equilibrium temperature and a decrease to 150 ppm produces a slight decrease. At higher levels in the stratosphere, with lower pressures and temperatures, an increase in the CO_2 concentration produces a decrease in temperature. However, the downward LWIR flux from the stratosphere is absorbed by the wider molecular lines in the troposphere (see Fig. 19) and does not influence the surface temperature. In the real atmosphere there is no equilibrium and the changes in the rates of cooling have to be considered, not the changes in temperature. At low and mid latitudes, the total tropospheric LWIR cooling rate is between -2.0 and -2.5 K per day, Feldman et al (2008). A doubling of the CO_2 concentration from 300 to 600 ppm produces a decrease in the rate of cooling or a slight warming of up to +0.08 K per day (see Fig. 21), Iacono et al (2008). This is simply too small to measure in the normal daily temperature changes in the lower troposphere and cannot accumulate over time. M&W applied their time integration procedure in MW67 without any consideration of the errors involved. The fixed RH assumption amplified the initial CO_2 induced warming produced by their model. This amplification or water vapor feedback was a secondary effect in the model. The fixed RH assumption was made so that the atmospheric temperature profiles generated by MW67 were a better match to the average of the measured data compared to steady state model results obtained using a fixed absolute humidity as described in MS64.

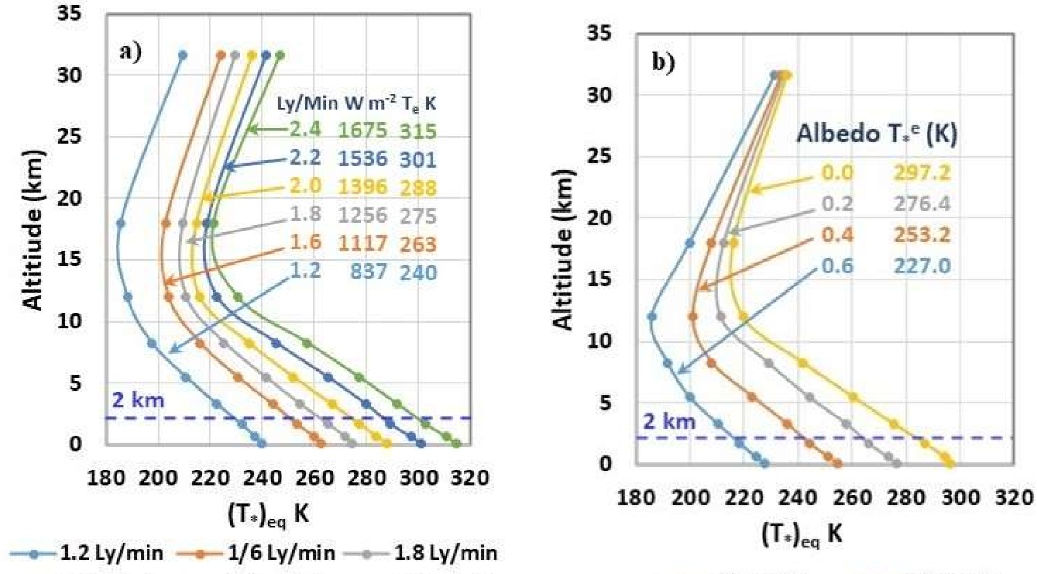

Fig. 8. Vertical Distribution of radiative convective equilibrium temperature of the atmosphere with a given distribution of relative humidity for various values of the solar constant.

Fig. 19. Vertical distributions of radiative convection equilibrium for various values of the surface albedo

Figure 6: a) Steady state temperature profiles for selected values of the solar flux. The table, inset, gives the values of the solar flux in Ly min^{-1} and W m^{-2} and the equilibrium surface temperatures. b) steady state temperature profiles for selected surface albedos. The table, inset gives the values of the albedo and the corresponding equilibrium surface temperatures. The 2 km level is indicated. Under clear sky conditions, almost all of the downward LWIR flux to the surface originates from within this 2 km layer.

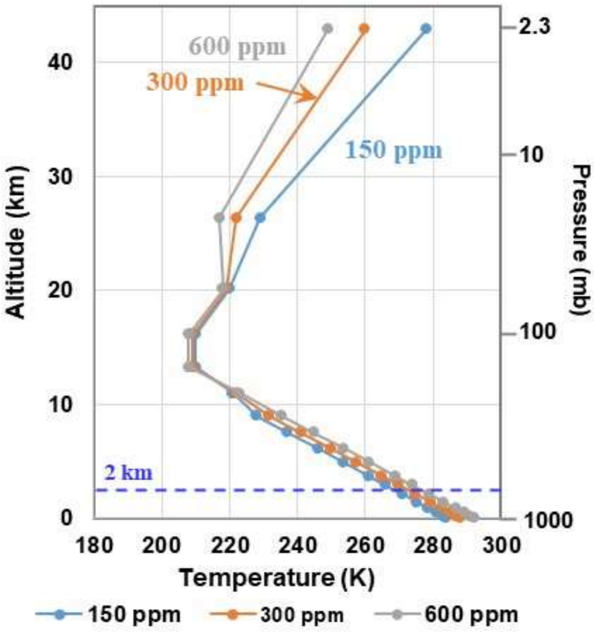

Fig. 16. Vertical distribution of temperature in radiative convective equilibrium for various values of the CO_2 content.

Figure 7: *The equilibrium temperature profiles calculated by the MW67 model for atmospheric CO_2 concentrations of 150, 300 and 600 ppm.*

3.2 The 1975 Manabe and Wetherald Model (MW75)

M&W spent the next eight years incorporating the algorithms used in the MW67 model into every unit cell of a 'highly simplified' global circulation climate model (MW75). They used the same time integration procedure and the model still required a year of model integration time to reach a steady state. This is shown in Fig. 8 (data from MW67, figs. 5 and 3). When the atmospheric CO_2 concentration was doubled from 300 to 600 ppm in MW75, the average increase in surface temperature was 2.93 °C. This should be compared to the 2.36 °C increase for average cloudiness conditions in MW67.

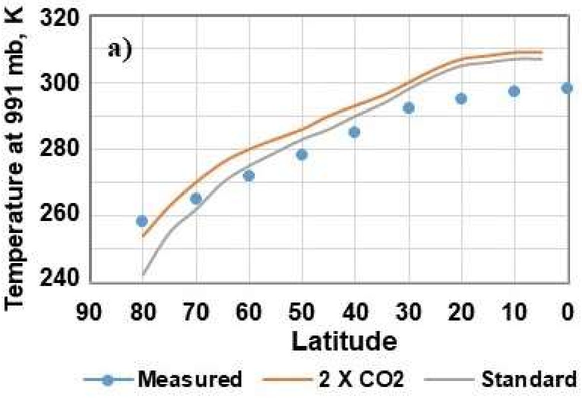

Fig. 5. Zonal mean temperature at the lowest prognostic level (i.e.~991 mb). Dots indicate the observed distribution of zonal mean surface air temperature (Oort and Rasmusson, 1977)

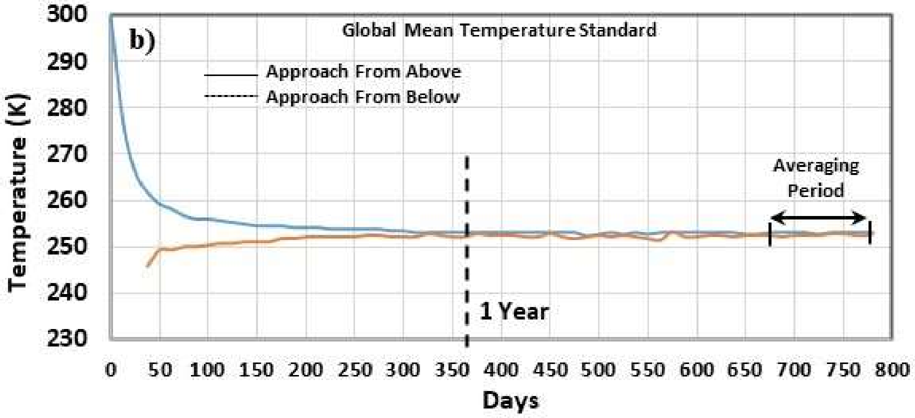

Fig. 3. Time variation of (mass-weighted) mean temperature for the entire period of the two standard runs.

Figure 8*: a) The warming generated by a CO_2 doubling in MW75 and b) the time to reach model equilibrium.*

3.3 Mission Creep: Climate Modeling at NASA

The planetary atmospheres group at NASA started to transition to the analysis of the earth's climate as the Apollo (moon landing) program ended in 1972 (Hansen, 2000; Rasool and Schneider, 1971; Wang and Domoto 1974; Ramanathan, 1975). In 1976 they added 10 minor species to the MW67 model, Wang et al (1976), H76. Their results are summarized in Fig. 9, from H76, table 3. Separate calculations were run for fixed cloud top temperature and fixed cloud top altitude. All of the temperature changes were created by the MW67 model assumptions.

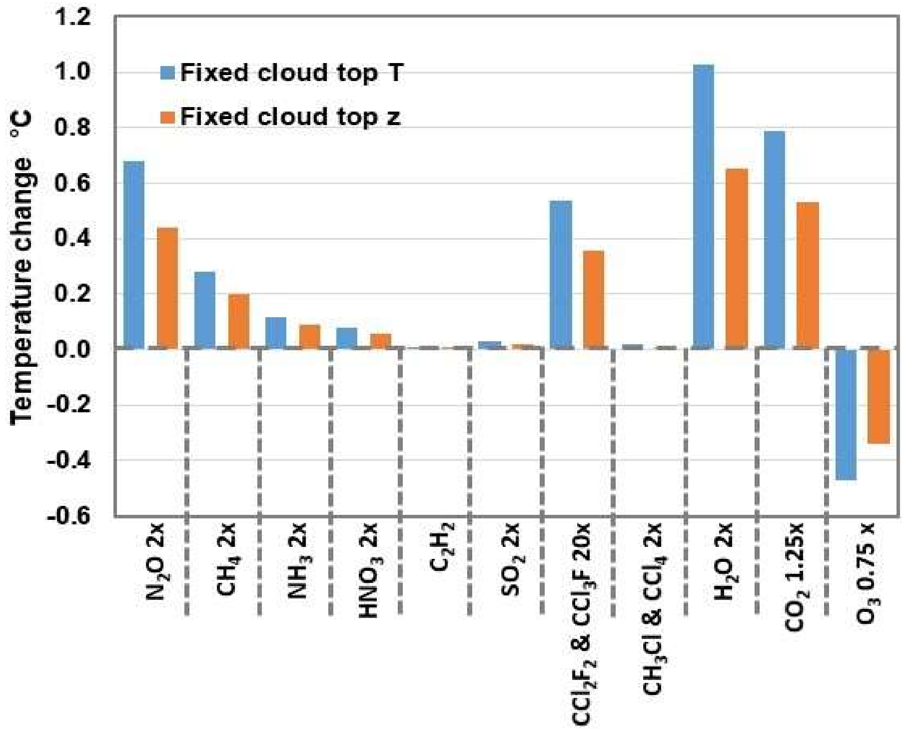

Figure 9: Calculated changes in equilibrium surface temperature obtained by using the H76 1-D RC model with changes in species concentration as shown. Separate calculations were run for fixed cloud top temperature and fixed cloud top altitude (data from H76, Table 3).

Later, in H81 Hansen et al (1981) added a slab ocean model, the step CO_2 doubling and the calculation of a global mean temperature record to the MW67 model calculations. First, they tuned their model so that a doubling of the CO_2 concentration from 300 to 600 ppm produced an increase in equilibrium surface temperature of 2.8 °C. This is shown in Fig. 10a (H81, table1). Model configuration number 4 was selected. Next, they added a two layer slab ocean to the MW67 model. This added heat capacity and a time delay, but the surface energy transfer, particularly the wind driven evaporation or latent heat flux was ignored. This was a flat ocean model without wind or waves. The calculated increase in temperature produced by increasing the CO_2 concentration in H81 for various slab ocean configurations is shown in Fig. 10b (data from H81, fig. 1). The equilibrium temperature changes produced by various radiative perturbations were then considered as shown in Fig. 10c (data from H81, fig. 2). This was a continuation of H76 that included cooling from clouds and aerosols as well as warming from greenhouse gases. Next, the step CO_2 doubling was introduced. These are the flux and temperature changes produced by the H81 model when the CO_2 concentration is first doubled from 300 to 600 ppm and the model is then allowed to return to a steady state. This is shown in Fig. 10d (data from H81, fig. 4). The global temperature record used in H81 is shown in Fig. 10e (adapted from H81 fig. 3). The increase in CO_2 concentration, Keeling (2023) has been added for reference. The 1940 peak produced by the warming phase of the AMO is indicated. The authors of H81 now claimed that they could simulate this global temperature record using a combination of warming from an increase in atmospheric CO_2 concentration, changes in solar flux and cooling produced by volcanic aerosols. This is shown in Fig. 10f (adapted from H81, figure 5). The 1940 AMO peak in Fig. 10f is indicated with a red asterisk.

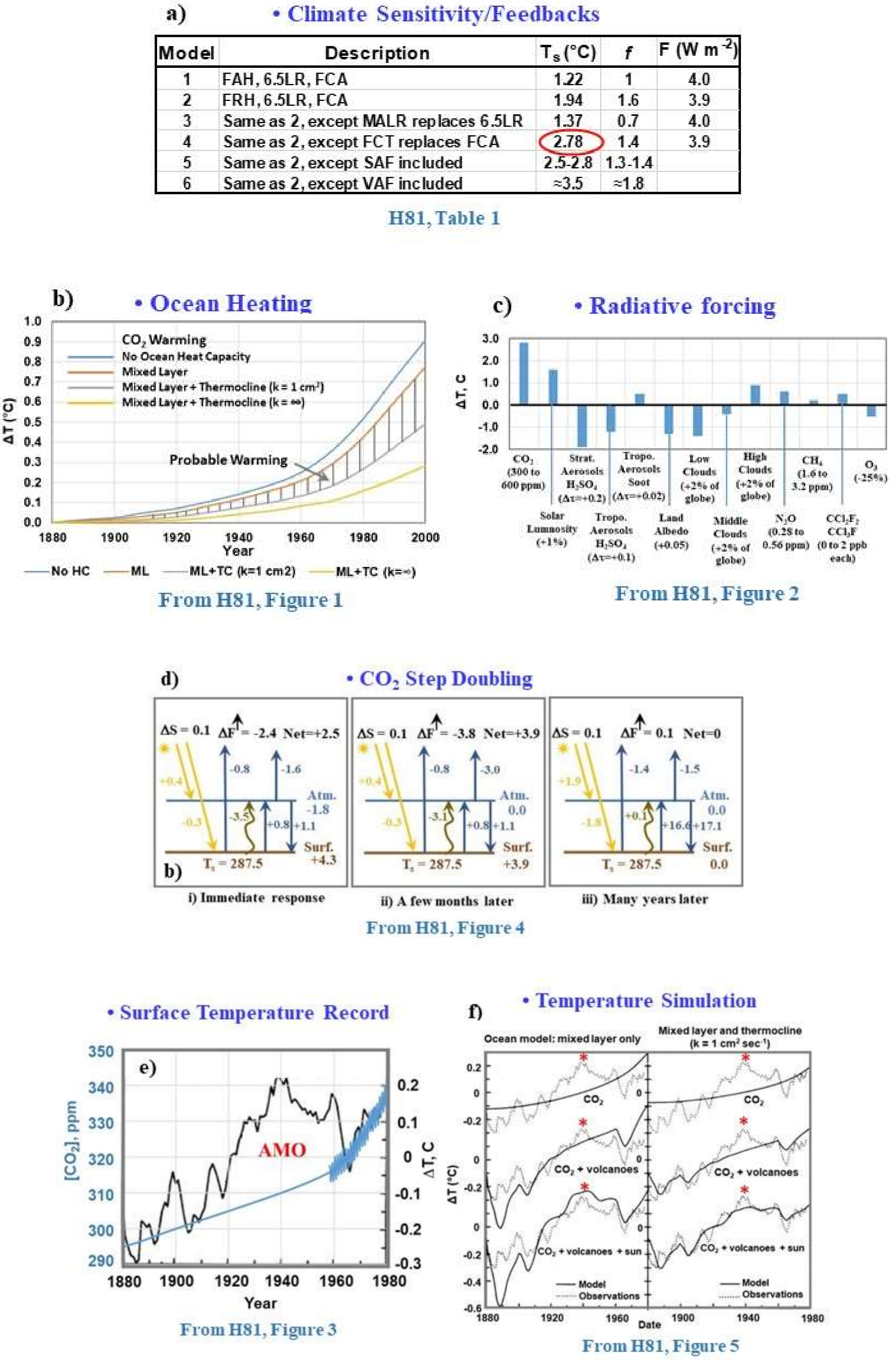

a) • Climate Sensitivity/Feedbacks

Model	Description	T_s (°C)	f	F (W m^{-2})
1	FAH, 6.5LR, FCA	1.22	1	4.0
2	FRH, 6.5LR, FCA	1.94	1.6	3.9
3	Same as 2, except MALR replaces 6.5LR	1.37	0.7	4.0
4	Same as 2, except FCT replaces FCA	2.78	1.4	3.9
5	Same as 2, except SAF included	2.5-2.8	1.3-1.4	
6	Same as 2, except VAF included	≈3.5	≈1.8	

H81, Table 1

From H81, Figure 1

From H81, Figure 2

i) Immediate response

ii) A few months later

iii) Many years later

From H81, Figure 4

From H81, Figure 3

From H81, Figure 5

Figure 10: *The foundation of the pseudoscience of radiative forcings, feedbacks and climate sensitivity established by H81. The 1940 AMO peak in the global mean temperature record from e) is indicated by an asterisk in f).*

The radiative perturbations used in H81 were later called radiative forcings. They have been used to explain climate change in all of the IPCC Climate Assessment Reports (Ramaswamy, 2019). None of the work at NASA was challenged by Manabe's group. They accepted the slab ocean model and calculated the ocean heating in a mixed ocean layer produced by a 4x increase in CO_2 concentration using a simplified GCM, Manabe and Stouffer (1979; 1980). They obtained an increase in ocean temperature of 3.2 °C. This is illustrated in Fig. 11 (data from Manabe and Stouffer, 1980, fig. 6).

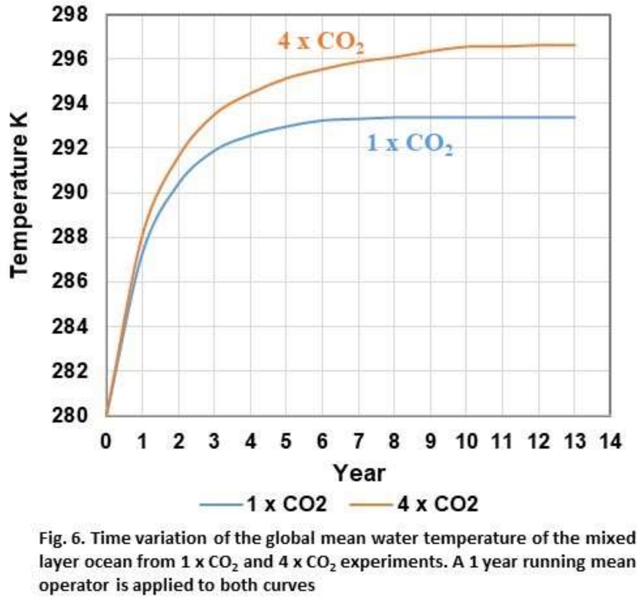

Fig. 6. Time variation of the global mean water temperature of the mixed layer ocean from 1 x CO_2 and 4 x CO_2 experiments. A 1 year running mean operator is applied to both curves

Figure 11: Ocean warming produced by a 4x increase in CO_2 concentration. (Data from fig. 6, Manabe and Stouffer, 1980).

The climate models use radiative transfer algorithms to calculate rates of LWIR cooling and solar heating that are integrated over time to determine the changes in temperature in the model. The calculation of the LWIR rates of cooling was discussed by various authors including Plass (1956a) for CO_2 only, Manabe and Strickler (1964), Stone and Manabe (1968) and Ackerman (1979). Most of this work was focused on the total LWIR cooling rate. More recent work by Feldman et al (2008) for a tropical model atmosphere gives a tropospheric cooling rate between -2.0 and -2.5 °C per day (see Fig. 21a). Ackerman provided both total cooling rates for mid latitude summer conditions and the change in cooling rates produced by a doubling of the CO_2 concentration from 300 to 600 ppm. The total cooling rates are shown in Fig. 12a (data from Ackerman, fig. 3a). They are similar to those published by Feldman et al. The 800 mbar level at approximately 2 km is indicated by the blue dotted line. Almost all of the downward LWIR flux from the lower troposphere to the surface originates from below this 2 km level. The maximum change in tropospheric cooling rate for a doubling of the CO_2 concentration from 300 to 600 ppm is near +0.08 °C per day. This is shown in Fig. 12b and on a larger scale in the inset, Fig. 12c (data from Ackerman, fig. 3b). The changes in tropospheric cooling rates are similar to those given by Iacono et al (2008) (see Fig. 21c). These are too small to detect in the normal diurnal and seasonal variations of the surface and near surface boundary layer temperatures. At a lapse rate of -6.5 °C km^{-1}, an increase in temperature of +0.08 °C is produced by a decrease in altitude near 12 meters. This is equivalent to riding an elevator down 4 floors.

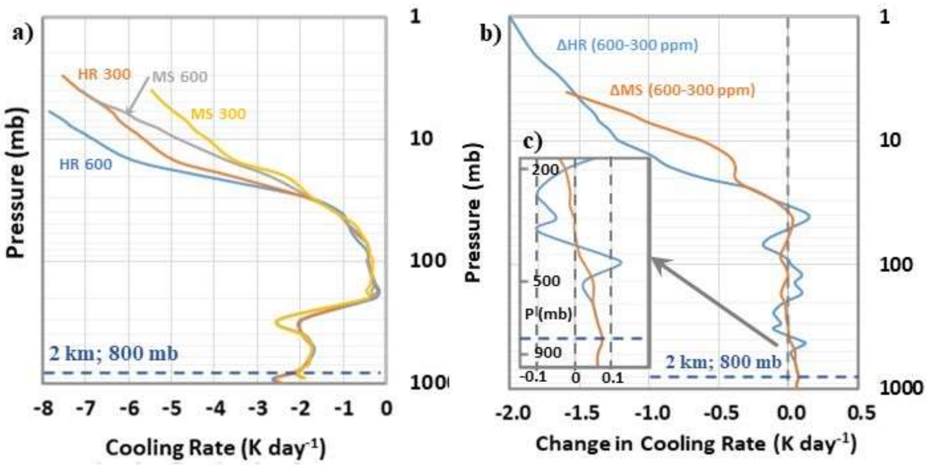

Fig. 3(a) Heating rate profiles computed with HR and MS codes for CO_2 concentrations of 300 ppm and 600 ppm using mid latitude summer profiles.

Fig. 3(b) Difference between heating rate profiles for computed CO_2 concentration of 300 ppm and 600 ppm for HR code and MS code

Figure 12: a) LWIR cooling rates for atmospheric CO_2 concentrations of 300 and 600 ppm, b) the change in these cooling rates produced by the doubling of the CO_2 concentration from 300 to 600 ppm and c) change in tropospheric cooling rates on an enlarged scale. Data from Ackerman (1979).

In H84, Hansen et al (1984) applied electronic feedback theory to climate modeling and the concept of climate sensitivity. They assumed that the amplification created by the fixed relative humidity assumption introduced in MW67 was real. Other feedbacks related to cloud cover and snow/ice extent were also included. When the flux balance at TOA was perturbed by a CO_2 doubling or a 2% increase in solar flux, their GCM would respond and restore the flux balance at TOA by adjusting the surface and air temperatures. The feedbacks altered the temperature response needed to achieve this energy balance. They also assumed that the planetary average LWIR flux emitted to space defined an effective emission temperature. In reality, there is no global average temperature, nor is there an effective emission temperature, Essex et al (2007). This is discussed in more detail in Section 5.3.

3.4 From 1-D RC Models to Coupled GCMs

As computer technology improved, the 1-D RC model was replaced by larger atmospheric GCMs and later by coupled atmosphere-ocean GCMs. The exact flux balance at TOMA in the 1-D models was replaced by an average planetary flux balance. However, the fundamental equilibrium assumption, that an increase in greenhouse gas forcings perturbed the planetary energy balance did not change, Knutti and Hegerl (2008). The surface temperature had to warm to restore the planetary flux balance. Furthermore, the initial change in LWIR flux was still amplified by a water vapor feedback. In addition, the ocean was warmed by the increase in downward CO_2 LWIR flux to the surface.

In 1979 there were only two modeling groups that provided GCM data for the Charney Report (1979). By 1995, 18 coupled climate models were available from seven different countries, Meehl et al (1997). In 2019 there were 49 modeling groups with approximately 100 different models involved in CMIP6 generating data to be incorporated into the Sixth IPCC Climate Assessment, Hausfather (2019). All of these models used the same basic approach established by MW67 and H81.

The radiative forcings, the climate model simulation of the global mean temperature record and the equilibrium climate sensitivities (ECS) published in each of the IPCC Climate Assessment Reports are shown in Figs. 13, 14 and 15 (IPCC, 2021; 2013; 2007; 2001; 1995; 1990). The simulation from H81 (fig. 5) is also shown in Fig. 14a. The 1940 AMO peak in the global mean temperature record is indicated by a red asterisk. The ECSs vary from approximately 2 to 5 °C and are indicators of the differences in the model parameters such as feedbacks that are used to tune the models to match the global mean temperature record. The IPCC uses FAR, SAR and TAR to denote the First, Second and Third Assessment Reports, then changed to AR4, AR5 and AR6 for the later reports. AR1, AR2 and AR3 labels are also included on Figs A14, A15 and A16. The ocean oscillations such as the AMO are produced by a natural imbalance between the solar heating and the wind driven cooling within the ocean gyre circulation.

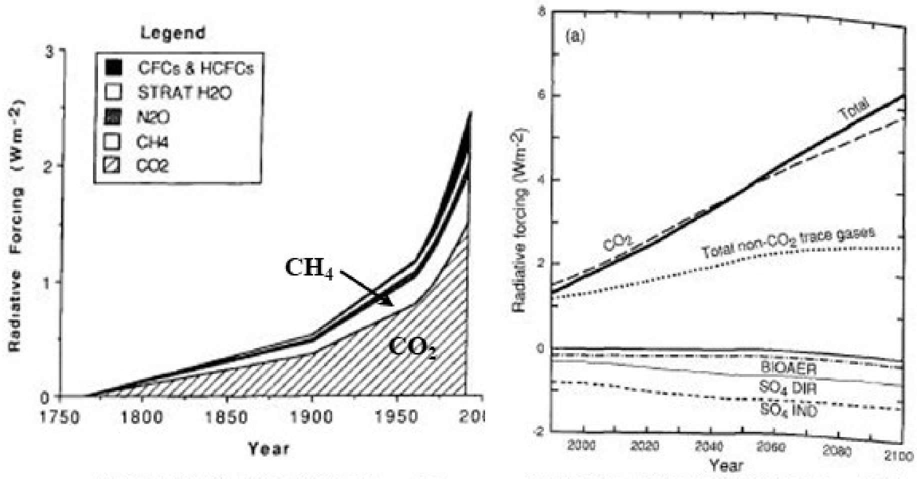

a) FAR (AR1) 1990 Fig. 2.2 **b) SAR (AR2) 1995 Fig 6.19a**

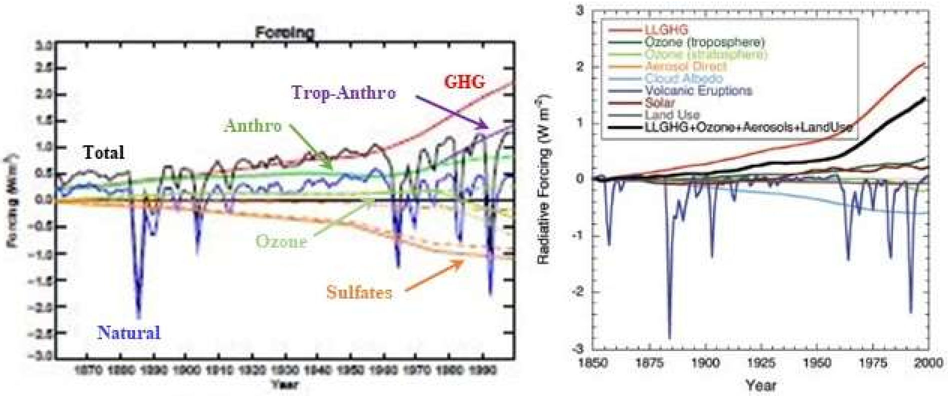

c) TAR (AR3) Tett et al, 2000, fig. 1 **d) AR4 2007 Fig 2.23**

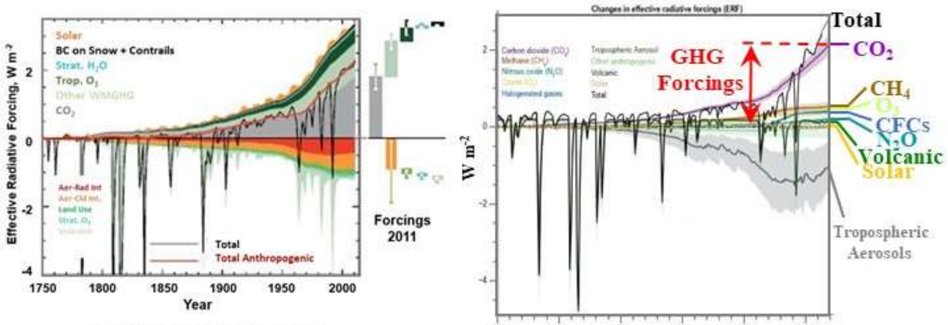

e) AR5 2013 Fig 8.18 **f) AR6 2021 Fig 2.10**

Figure 13: The time series of the radiative forcings (W m^{-2}) from the six IPCC climate assessment reports. For the Third AR, the source is Tett et al (2000). This is given as one of the sources of TAR Figure 12.7.

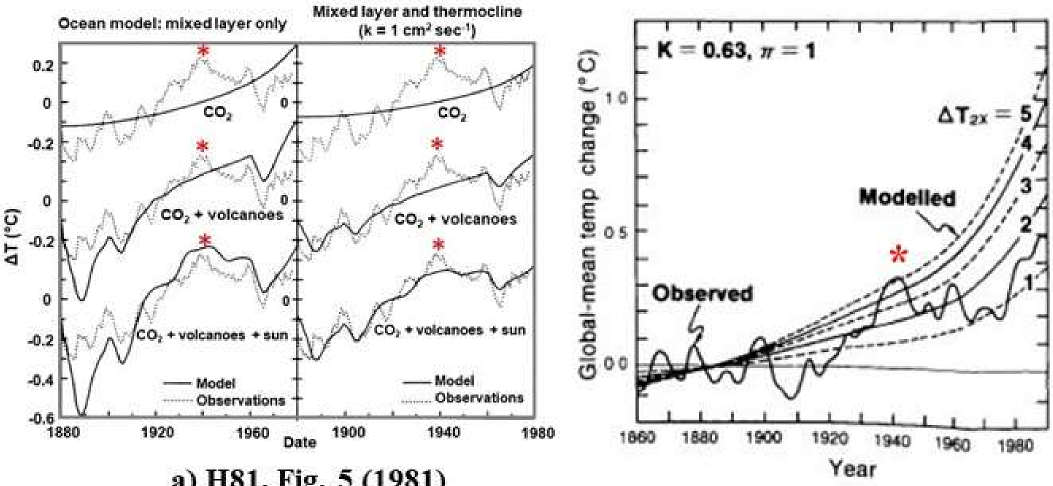

a) H81, Fig. 5 (1981)

b) FAR (AR1) Fig 8.1, Panel 1 (1990)

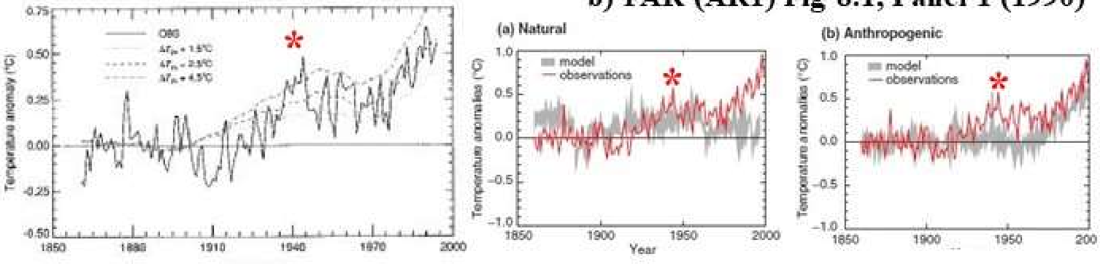

c) SAR (AR2) Fig 8.6c (1995)

d) TAR (AR3) Fig 4, SPM (2001)

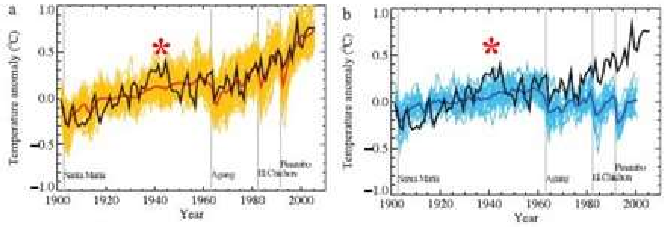

e) AR4 Fig 9.5 (2007)

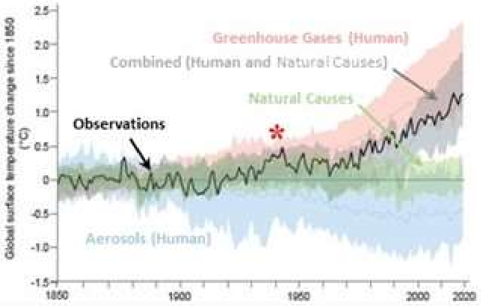

g) AR6 FAQ 3.1 Fig. 1 (2021)

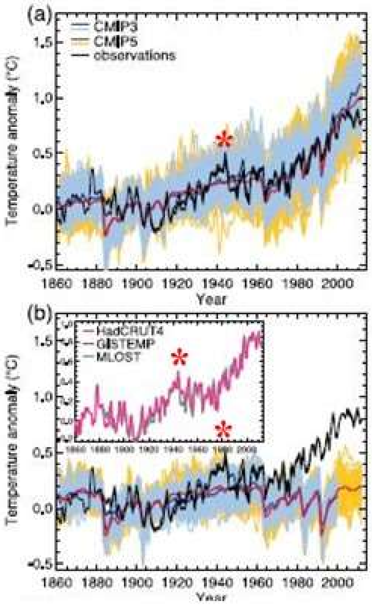

f) AR5 Fig. 10.1 (2013)

Figure 14: *Climate model simulations of the global mean temperature record from H81 to AR6. Starting with the TAR in 2001, the radiative forcings were split into natural and anthropogenic causes with separate contributions to the global mean temperature record. The 1940 AMO peak is indicated with a red asterisk.*

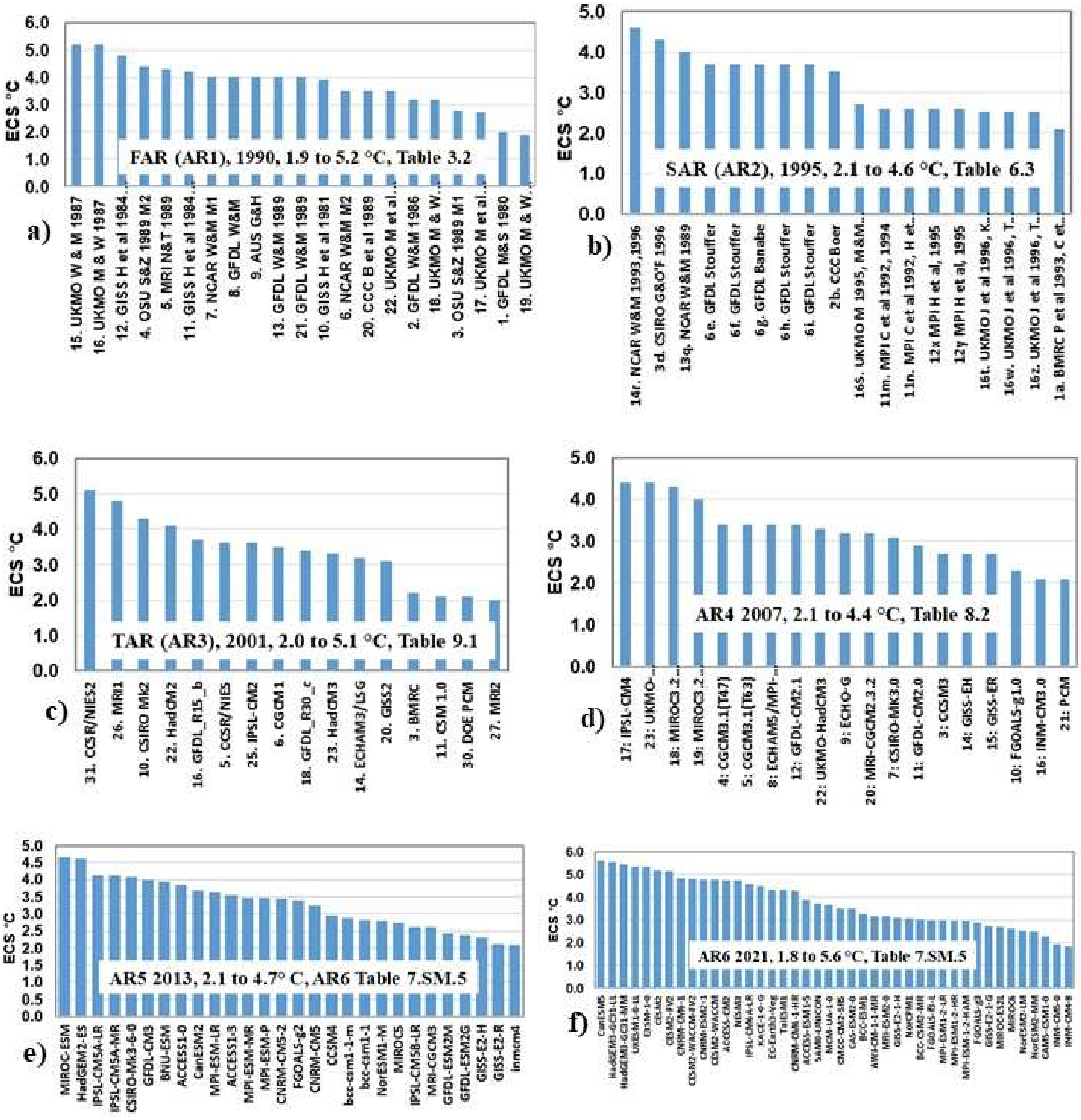

Figure 15: The equilibrium climate sensitivities (ECS) for various climate models from the six IPCC reports. The sources are indicated in the figures.

3.5 Anthropogenic Radiative Forcing and Extreme Weather Attribution

Starting with the Third IPCC Climate Assessment Report (2001), the time series of radiative forcings was split into 'natural' and 'anthropogenic' forcings as shown in Fig. 16a, Tett et al (2000). Three different climate model configurations were used. The first was a natural baseline, run using just the solar and volcanic forcings agents. The second was the anthropogenic contribution, run with a combination of well mixed greenhouse gases, changes in stratospheric and tropospheric ozone and the direct and indirect effects of sulfate aerosols. The third was a combined run with both sets of forcings. The results for these model configurations are shown in Figs 16b, 16c and 16d. The statistical argument used to link an increase in anthropogenic forcings to an increase in the intensity and frequency of extreme weather events shown in Fig. 16e. It is based on changes in the mean and variance of the normal distribution of temperature. Little has changed since 2001. A good example is the annual supplement to the Bulletin of the American Meteorological Society 'Explaining Extreme Events of [Year] from a Climate Perspective', Herring et al (2022). The series has been published annually since 2012. The BAMS publication guidelines state:

> *Each paper will start with a 30 word capsule summary that includes, if possible, how anthropogenic climate change contributed to the magnitude and/or likelihood of the event.*

The CMIP5 and CMIP6 model ensembles and other climate models have been used without question to explain the observed extreme weather events for the year of interest. Natural climate changes related, for example to ocean oscillations and blocking high pressure systems have to be 'enhanced' by radiative forcings. The same approach using natural and anthropogenic forcings was used in the Sixth IPCC Climate Assessment Report (2021) as shown in Fig. 17.

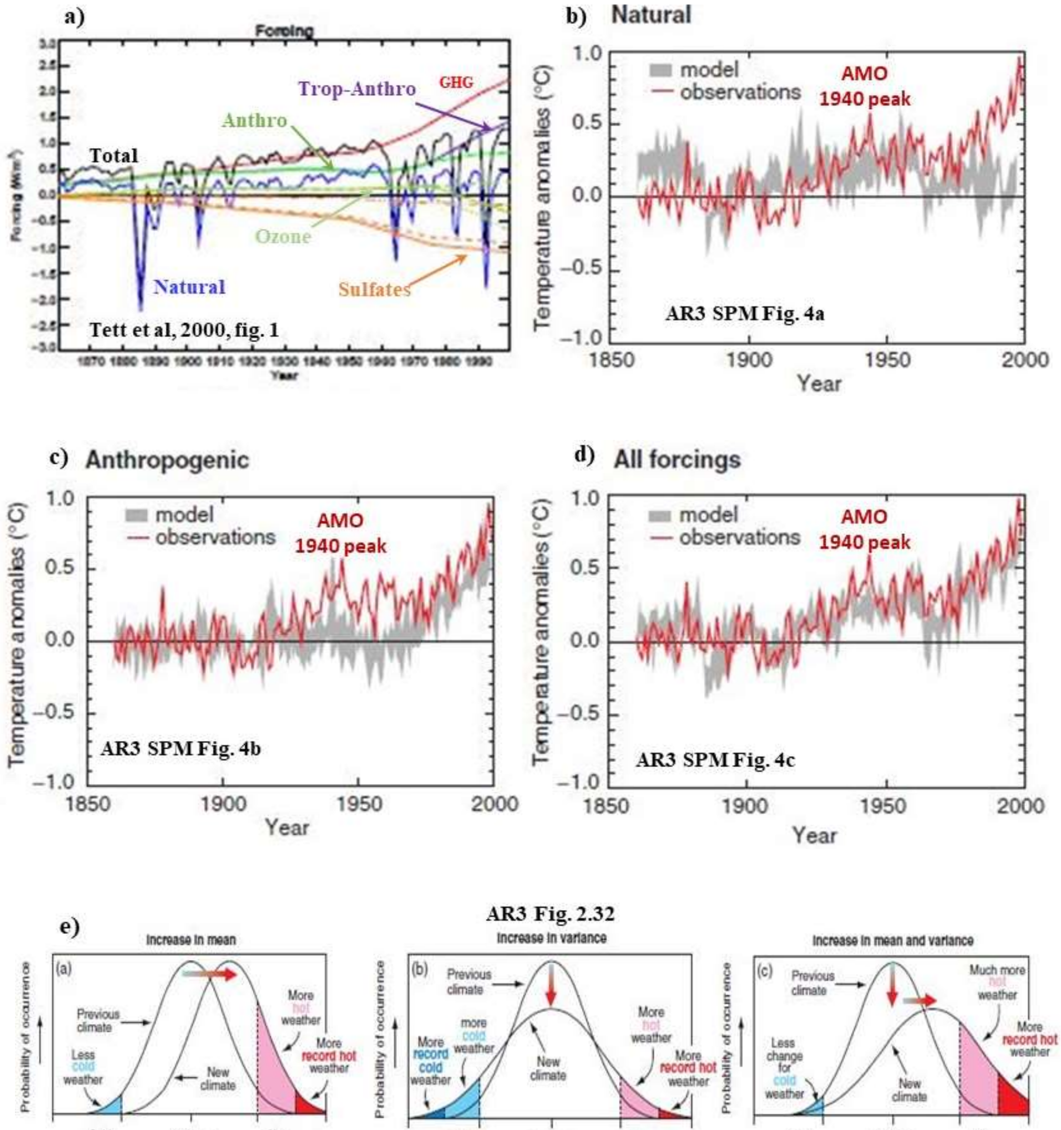

Figure 16: The radiative forcings used by the climate models to simulate the global mean temperature record shown in a) are separated into natural and anthropogenic sources. The climate models are rerun using the natural forcings to establish a 'natural' baseline b) and the anthropogenic forcings c) to show the 'human caused' warming. A vague statistical argument e) is used to claim that the anthropogenic warming caused an increase in the frequency and intensity of 'extreme weather events'.

3.6 Radiative Forcings, Feedbacks and Climate Sensitivity in AR6

The introduction to Chapter 7 of the Working Group 1 Report in the latest UN Intergovernmental Panel on Climate Change (IPCC), Climate Assessment, AR6, WG1 (2021) '*The Earth's energy budget, climate feedbacks, and climate sensitivity*' starts:

> *This chapter assesses the present state of knowledge of Earth's energy budget, that is, the main flows of energy into and out of the Earth system, and how these energy flows govern the climate response to a radiative forcing. Changes in atmospheric composition and land use, like those caused by anthropogenic greenhouse gas emissions and emissions of aerosols and their precursors, affect climate through perturbations to Earth's top-of-atmosphere energy budget. The effective radiative forcings (ERFs) quantify these perturbations, including any consequent adjustment to the climate system (but excluding surface temperature response). How the climate system responds to a given forcing is determined by climate feedbacks associated with physical, biogeophysical and biogeochemical processes. These feedback processes are assessed, as are useful measures of global climate response, namely equilibrium climate sensitivity (ECS) and the transient climate response (TCR).*

The time series of the radiative forcings used in the AR6 CMIP6 models and the related temperature changes are shown in Figs. 17a and 17b. The comparison to the global temperature record is shown in Fig. 17c. The attribution to human causes obtained by dividing the radiative forcings into 'natural' and 'human causes' is shown in Fig. 17d. The real causes of the observed temperature changes are shown in Fig. 17e. They are a combination of ocean temperature changes, urban heat island effects, changes to the rural/urban mix in the weather station averages and various 'adjustments' used to 'homogenize' the temperature data. It has been estimated that half of the warming in the 'global record' has been created by such adjustments. See for example, Andrews (2001a; 2017b; and 2017c), D'Aleo and Watts (2010), Berger and Sherrington (2022) and O'Neill et al (2022). The dominant terms in the ocean temperature contribution are the AMO (2022) and a linear temperature recovery from the Little Ice Age (LIA), Akasofu (2010). Further details are given in Section 4.5 (see Figs. 38 and 40). The climate models are simply 'tuned' to match the global temperature record. The 'tuned' models are then used to simulate the increase in global average temperature produced by a doubling of the CO_2 concentration. This gives the climate sensitivities shown in Fig. 17f (repeated from Fig. 15f).

There has been an extensive discussion in the literature over the magnitude of the climate sensitivity and the related feedbacks. (Lewis and Curry, 2018; Monckton, 2008; Soden and Held, 2006; Terando et al, 2020; Zelinka et al, 2020). These issues may be resolved by examining the time dependent energy transfer processes that contribute to the surface temperature. Climate energy transfer will now be considered in more detail in Section 4.

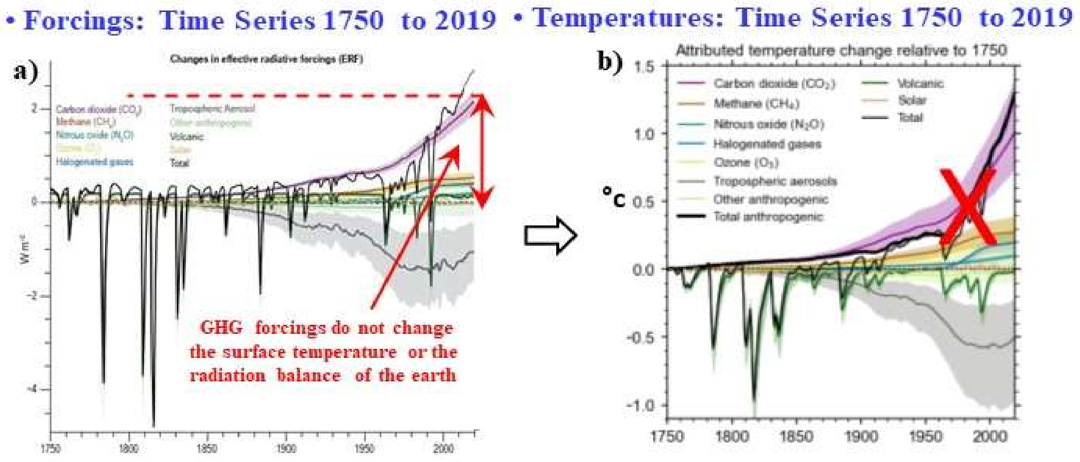

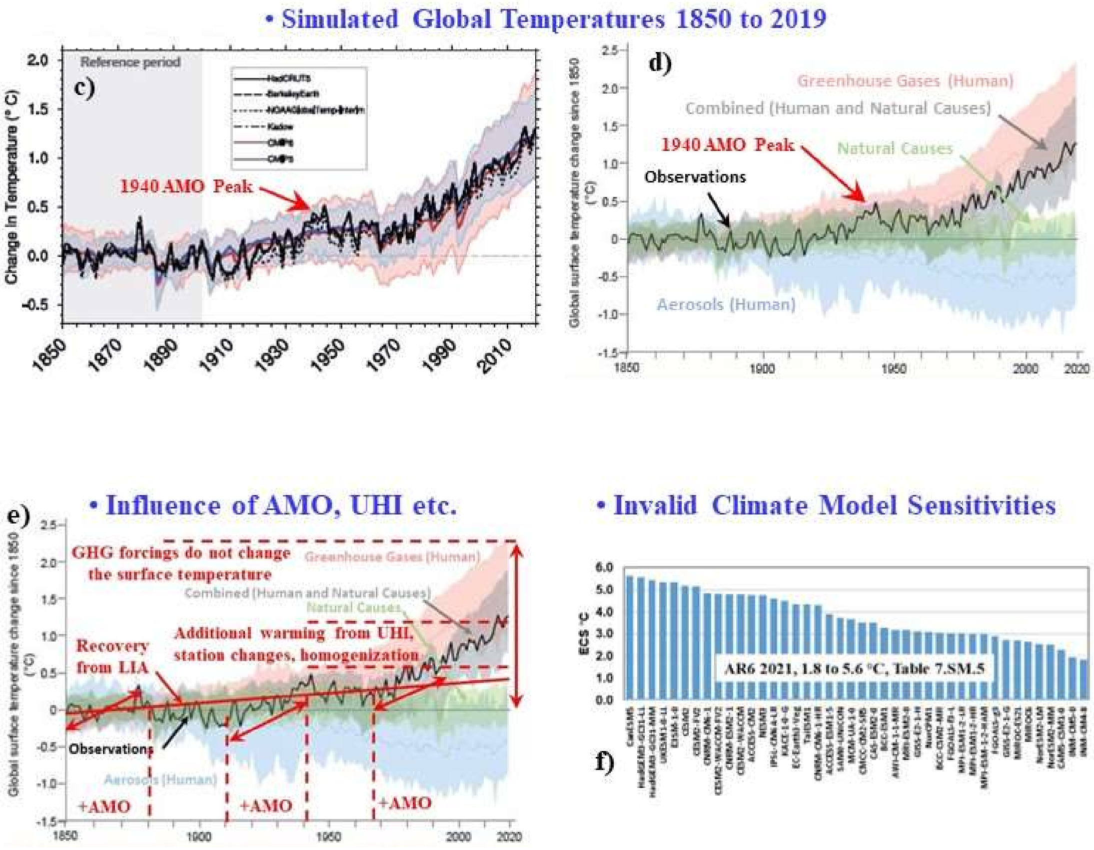

Figure 17: *The attribution process from the CMIP6 model ensemble used in AR6. a) time dependence of the radiative forcings and b) time dependence of the temperature changes derived from a), c) 'tuned' temperature record using a set of radiative forcings to simulate the global mean temperature record, d) separate sets of forcings are used to calculate 'human' and 'natural' temperature records, e) the contributions of the AMO, UHI etc. to the global mean climate record, f) the invalid equilibrium climate sensitivity (ECS) estimated from the CMIP6 models (IPCC AR6, WG1, figures 2.10, 7.8, 3.4b and FAQ 3.1 Fig. 1, ECS data from Table 7.SM.5)*

4. Climate Energy Transfer

Since 1800, the atmospheric concentration of CO_2 has increased by approximately 140 ppm, from 280 to 420 ppm, Keeling (2023). This has produced a decrease near 2 W m^{-2} in the LWIR flux emitted to space at TOA within the spectral range of the CO_2 emission bands. There has also been a similar increase in the downward LWIR flux from the lower troposphere to the surface, Harde (2017). For a CO_2 doubling from 280 to 560 ppm, the decrease in the outgoing longwave radiation (OLR) is estimated to be 3.7 W m^{-2}, IPCC (2013). At present, the average annual increase in CO_2 concentration is near 2.4 ppm. This produces an increase in the downward LWIR flux to the surface of approximately 0.034 W m^{-2} per year. The changes in CO_2 concentration are shown in Fig. 18a and the changes in total flux are shown in Fig. 18b. More detailed calculations of the change in flux at TOA produced by increases in the atmospheric concentration of H_2O, CO_2, O_3, N_2O and CH_4 have been provided by Wijngaarden and Happer (2022).

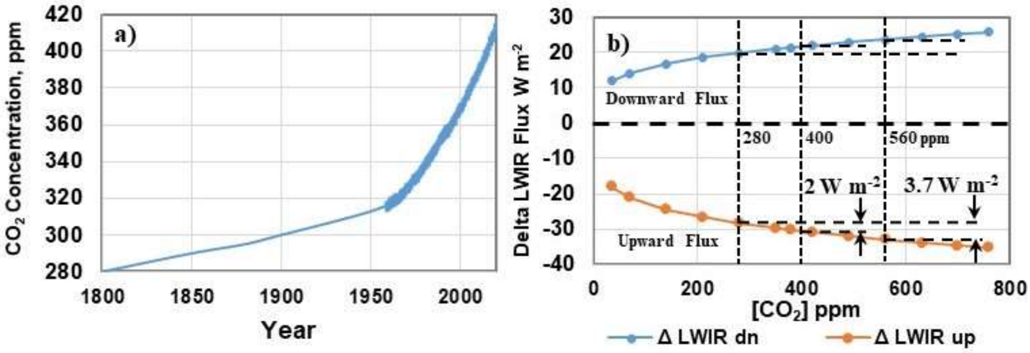

Figure 18: a) The measured increase in atmospheric CO_2 concentration from 1800 (Keeling curve) and b) calculated changes in atmospheric LWIR flux produced by an increase in atmospheric CO_2 concentration from 0 to 760 ppm. Data from table 1, Harde (2017).

In a non-equilibrium system, a change in flux produces a change in the rate of heating or cooling of a thermal reservoir. A change in temperature has to be determined by taking the change in heat content or enthalpy of the thermal reservoir of interest over a given time period and dividing this by the local heat capacity, Clark (2013a; 2013b). In addition to the LWIR flux, the solar heating, the evapotranspiration (moist convection) and the subsurface thermal transport are all coupled to the surface thermal reservoir and must be included in the analysis of the surface temperature. There may also be significant daily and seasonal time delays or phase shifts between the peak solar flux and the temperature response, Clark (2023). The energy transfer processes at the land-air and ocean-air interfaces are different and have to be considered separately.

Convection is also a mass transport process that is coupled to the gravitational field and the rotation of the earth. These interactions result in the formation of the Hadley, Ferrell and polar cell convective structure, the trade winds and the ocean gyre circulation. This is the source of the earth's weather patterns. In the troposphere, vertical motion changes the temperature of an air parcel by air compression/expansion (see Section 4.6). This process is fully coupled to the air parcel cooling produced by the net LWIR emission.

The IPCC assumes that the decrease in LWIR flux at TOA produced by an increase in atmospheric greenhouse gas concentration changes the energy balance of the earth and that the surface temperature increases until the energy balance at TOA is restored. In addition, it is assumed that the initial increase in temperature produces an increase in water vapor concentration that the amplifies the temperature response. Other effects, such as an increase in aerosol concentration may increase the solar flux reflected back to space and produce surface cooling. Changes in flux at TOA are called radiative forcings, Ramaswamy et al (2019). An elaborate scheme of forcings and feedbacks is used in the coupled atmosphere-ocean climate models to simulate climate change. This approach is illustrated above in Figs. 13 and 14. However, when the time dependent energy transfer processes that determine the surface temperature are considered, a very different picture emerges. This has been discussed in detail by Clark and Rörsch (2023). There are five parts to this analysis.

1) The LWIR flux in the atmosphere consists of many thousands of overlapping molecular lines. The line intensity depends on the molecular concentration and the temperature. The linewidth is influenced by molecular collisions. The lines are wider and more intense at lower altitudes. Almost all of the downward greenhouse gas LWIR flux from the atmosphere to the surface is emitted from within the lowest 2 km layer of the troposphere. When the atmospheric greenhouse gas concentration is increased, any additional heat released into the troposphere is decoupled from the surface by a combination of molecular line broadening and turbulent convection.

2) There is no thermal equilibrium or steady state, so a change in flux has to be interpreted as a change in the rate of cooling (or heating) of a set of coupled thermal reservoirs. In the troposphere, at low to mid latitudes, a doubling of the CO_2 concentration from 300 to 600 ppm produces a

maximum decrease in the LWIR cooling rate, or a slight warming of +0.08 °C per day. When this is combined with the normal daily and seasonal variations in surface temperature, any temperature increases from a CO_2 doubling are too small to detect.

3) Over the oceans, the penetration depth of the LWIR radiation is less than 100 micron (0.004 inches). The wind driven evaporation removes water molecules from the surface. The net LWIR cooling flux and the latent heat flux are combined in a thin surface layer. The cooler water produced in this layer sinks and is replaced by warmer water from the bulk ocean below. Within the ±30° latitude bands, the annual average long term latent heat flux is at least 100 W m^{-2}. The average annual increase in atmospheric CO_2 concentration is currently near 2.4 ppm per year. This produces a decrease in the net LWIR cooling flux of approximately 0.034 W m^{-2} yr^{-1}. This is too small to have any measurable effect on ocean temperatures.

4) Over land, almost all of the absorbed solar flux is dissipated within the same diurnal cycle in which it is received. Heat is removed from the surface by convection during the day when the surface is warmer than the air layer above. There is a convection transition temperature each evening when the convection stops and the surface continues to cool more slowly by net LWIR emission. This transition temperature is reset each day by the local weather system passing through. A decrease in net LWIR cooling flux of approximately 0.034 W m^{-2} yr^{-1} is too small to produce a detectable change in surface temperature variation associated with this transition temperature.

5) The IPCC claims that a series of radiative forcings can be used to explain the observed global mean temperature record. Consideration of the time dependent energy transfer processes that determine the surface temperature and the averaging process used to determine the global temperature record provide an alternative explanation. The well-known quasi-periodic oscillations in ocean surface temperature are coupled to the land based weather station record by weather systems that form over the oceans and move over land. This coupling is produced by changes to the convection transition temperature in the diurnal temperature cycle. In addition, urban heat island effects have increased as urban areas have grown in size. Changes to the mix of urban and rural weather stations used to determine the global average temperature have also added bias to the record. The process of homogenization used to adjust the raw temperature data may also add warming.

These areas will now be considered in more detail.

4.1 Radiative Forcing by Greenhouse Gases does not Change the Radiation Balance of the Earth

When the atmospheric concentration of a greenhouse gas is increased, there is a decrease in the LWIR flux emitted to space at TOA, within the spectral region of the absorption/emission band specific to each greenhouse gas considered, Wijngaarden and Happer (2022). A change in flux at TOA is considered to be a radiative forcing that changes the radiation balance of the earth (see Section 3.6). Other radiative forcings, such as changes in aerosol concentration may increase the reflected solar flux at TOA and produce cooling. It is then assumed that the surface temperature adjusts to restore the flux balance at TOA, Knutti and Hegerl (2008). The IPCC also assumes that there is a linear relationship between the radiative forcing ΔF and the surface temperature response ΔT (IPCC, 2021; Ramaswamy, 2019). The change flux at TOA, ΔN is given by:

$$\Delta N = \Delta F + \alpha \Delta T \qquad (1)$$

Here α is a net feedback parameter. The initial forcing, ΔF is reduced by the surface temperature response.

The concept of radiative forcing by greenhouse gases was first introduced by Ramanathan, (1975) for a 1-D RC steady state model. It is a mathematical construct based on conservation of energy applied to an equilibrium average climate state. The secondary energy transfer processes that occur after the initial photon absorption by the greenhouse gas molecules were not considered. The excited molecular vibration-rotation states formed by IR photon absorption are rapidly quenched by molecular collisions and the photon energy is transferred to the local air parcel as heat. The small amount of additional heat released at each level in the troposphere is then dissipated by a combination of wideband LWIR emission and local turbulence. The downward transfer of energy by LWIR emission is limited by the increase in linewidth with decreasing altitude. The initial wavelength specific decrease in LWIR flux at TOA is converted to wideband LWIR emission back to space at TOA. Any change to the energy balance of the earth is insignificant.

The atmospheric LWIR flux consists of IR emission and absorption from many overlapping lines (Clark and Rörsch, 2023; Wijngaarden and Happer, 2022). Each line is a specific transition between two molecular rotation-vibration states. The lines are broadened by molecular collisions. The collision frequency in the troposphere is $>10^9$. The increase in linewidth associated with the decrease in excited state lifetime by molecular collisions is a consequence of the Heisenberg Uncertainty Principle applied to energy and time, Messiah (1999). Near the surface within the main absorption emission bands, the lines overlap and merge into a quasi-continuum. At higher altitudes, these lines become narrower as the temperature and pressure decrease. Some of the upward LWIR flux can pass through the gaps between these narrower lines above and continue to space without additional absorption/emission. The downward flux is absorbed by the wider lines below. This is illustrated schematically in Fig. 19a for a single line and in Fig. 19b for a group of lines in the 590 to 600 cm^{-1} region. Almost all of the downward LWIR flux that reaches the surface originates from within the first 2 km layer of the troposphere. Approximately half of this downward flux originates from the first 100 m layer. This is shown in Fig. 19c.

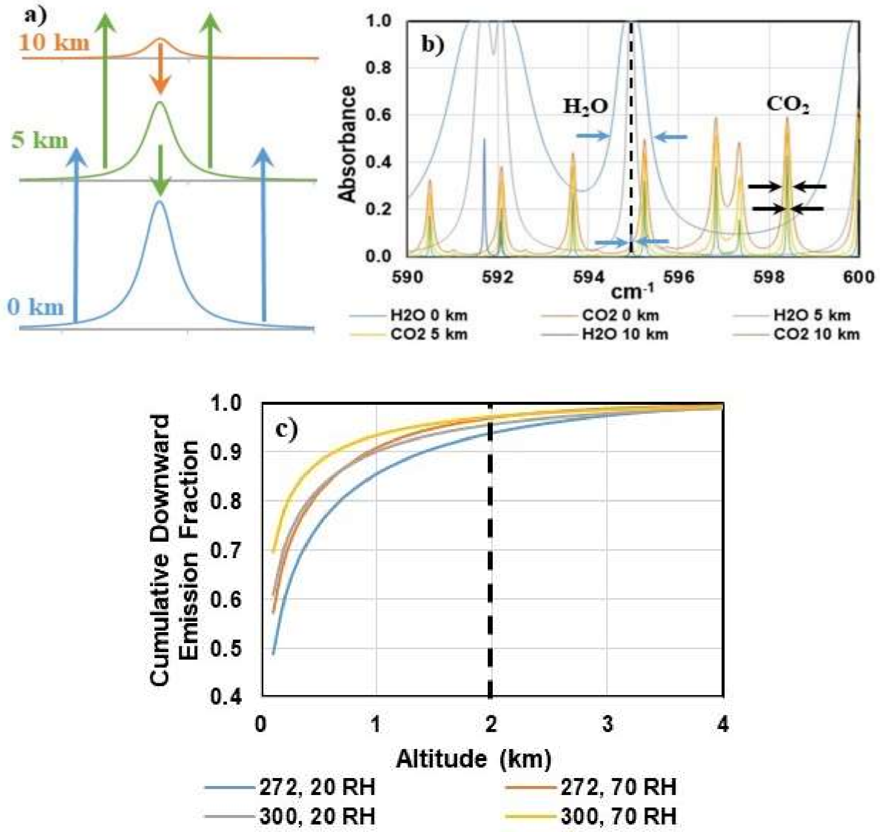

Figure 19: a) Transition from absorption-emission to free photon flux as the linewidth decreases with altitude. Single H_2O line near 231 cm^{-1}. b) Linewidths for H_2O and CO_2 lines in the 590 to 600 cm^{-1} spectral region for altitudes of 0, 5 and 10 km. c) Cumulative fraction of the downward flux at the surface vs. altitude for surface temperatures of 272 and 300 K, each with 20 and 70% relative humidity (RH). Almost all of the downward flux reaching the surface originates from within the first 2 km layer. Approximately half originates from within the first 100 m layer above the surface.

Fig. 20a illustrates the energy transfer processes for an air parcel in the troposphere (within the plane parallel atmosphere approximation). The air parcel is emitting LWIR radiation upwards and downwards at the local air temperature. It is also absorbing part of the upward LWIR flux from below and the downward LWIR flux from above. There may also be some direct heating produced by the absorption of near IR (NIR) solar radiation by the water vapor overtone bands. The air parcel is also in a turbulent convective flow field. Vertical motion changes the temperature of the air parcel at the local lapse rate. As the air parcel cools during convective ascent, internal molecular energy is converted to gravitational potential energy. Fig. 20b illustrates the dissipation of the radiative forcing in the troposphere produced by an increase in the atmospheric CO_2 concentration. The small amount of additional heat that is produced by increased absorption at each level is initially coupled to the local air parcel. It is dissipated and radiated back to space at TOA as wideband LWIR emission, mainly by the water bands.

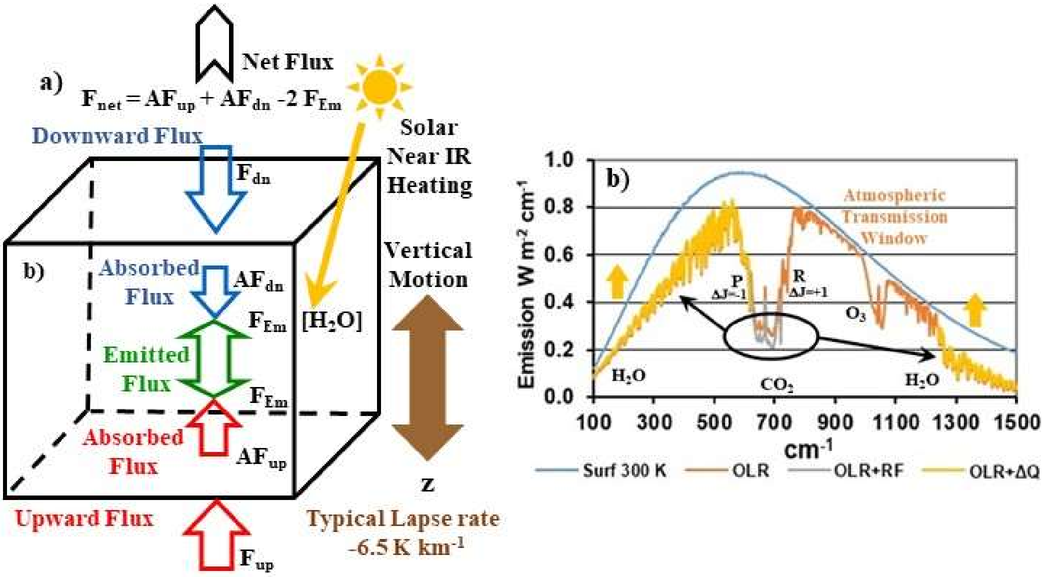

Figure 20: *a) The energy transfer processes for a local tropospheric air parcel (in a plane-parallel atmosphere) and b) the dissipation of the absorbed heat from a 'CO_2 doubling' by the normal tropospheric energy transfer processes (schematic). The wavelength specific increase in absorption in the CO_2 P and R bands is dissipated as small changes in broadband LWIR emission and gravitational potential energy.*

4.2 The LWIR Cooling Rate and the LWIR Surface Exchange Energy

When the atmospheric concentration of a greenhouse gas is increased, the decrease in LWIR flux at TOA is produced by small changes in emission at many different levels in the atmosphere. The emission from each level is modified by the absorption and emission of the levels above. In order to understand the atmospheric heating effects of a CO_2 doubling, the change in net LWIR flux has to be calculated at each level in the atmosphere and converted to a change in the rate of cooling by dividing by the heat capacity of the local air parcel. The total (10 to 3250 cm^{-1}) and spectral band average LWIR cooling rates for a tropical atmosphere are shown in Fig. 21a, Feldman et al (2008). The LWIR cooling rate for most of the troposphere at low latitudes is in the range 2 to 2.5 K per day.

The change in the rate of LWIR cooling in the atmosphere at mid latitudes produced by a doubling of the CO_2 concentration is shown in Fig. 21b, Iacono et al. (2008). In the stratosphere, there is a maximum change in the cooling rate of -3 K per day at an altitude of approximately 50 km with a pressure near 1 mbar and a temperature near 270 K. Because of the low pressure, the heat capacity of the air is also low, about 1.2 J m^{-3} K^{-1}. Therefore, the change in local net LWIR flux needed to produce a cooling rate of -3 K per day is approximately 40 μW m^{-3}. In addition, this cooling is decoupled from lower altitudes by molecular line broadening (see Fig. 19). Fig. 21c shows change in cooling rate for the troposphere on an enlarged scale. Here, the maximum change is +0.08 K per day at an altitude of 2 km. The required change in net LWIR flux is approximately 900 μW m^{-3}. At a lapse rate of -6.5 K km^{-1}, a daily change in temperature of +0.08 K requires a decrease in altitude of 12 meters. This is equivalent to riding an elevator down four floors. Similar results were obtained by Ackerman (1979), (see Fig 12).

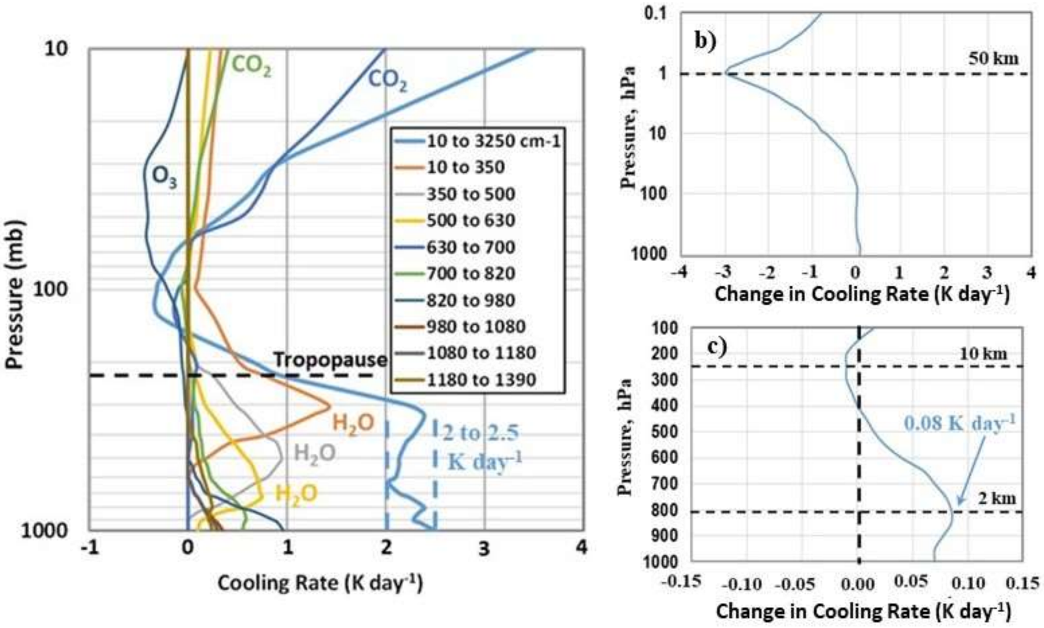

Figure 21: a) Total (10 to 3250 cm^{-1}) and band-averaged IR cooling rate profiles for the Tropical Model Atmosphere on a log-pressure scale, b) the change in atmospheric cooling rates produced by a CO_2 doubling from 287 to 574 ppm at mid latitude and c) the change in tropospheric cooling rates from b) on an enlarged scale.

Fig. 22 shows the vertical velocity profile up to 2 km altitude in the turbulent surface boundary layer. This is from Doppler heterodyne LIDAR measurements recorded over 10 hours at the École Polytechnique, south of Paris, July 10th 2005, Gibert et al (2007). The change in vertical velocity is ±2 m s^{-1}. For a vertical velocity of 1 m s^{-1} and a lapse rate of -6.5 K km^{-1}, an air parcel will cool by 6.5 K in 1000 seconds or about 17 minutes as it ascends to an altitude of 1 km. The short term cooling rate is -0.4 K per minute. This is much larger than any changes in the cooling rate produced by a CO_2 doubling as shown in Fig. 21c. Here the maximum decrease in the cooling rate is +0.08 K per day. In signal processing terms, the noise produced by the normal temperature variations in the surface boundary layer is sufficiently large that any temperature signal related to a CO_2 doubling is well below the detection limit. The increase in CO_2 concentration from 1880 to the present is near 140 ppm. In this case, the decrease in the LWIR cooling rate is near +0.04 K per day, which is also well below the detection limit.

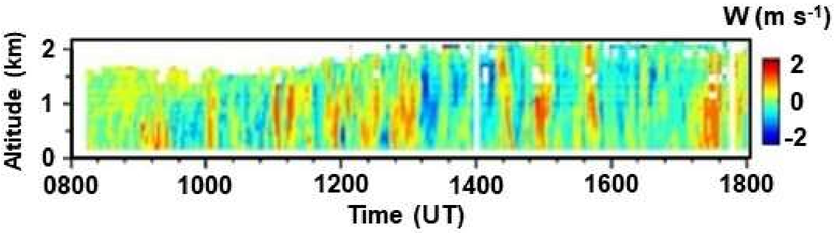

Figure 22: *Vertical velocity profile in the turbulent boundary layer recorded over 10 hours at the École Polytechnique, south of Paris, July 10th, 2005, using Doppler heterodyne LIDAR. Data adapted from Gibert (2007), fig.6.*

The basic assumption of a perturbation by a radiative forcing as introduced by Ramanathan (1975) is invalid.

> *The implications of Eq. 3 for the global climate can be examined by invoking the global energy balance condition which states that on a global average the incoming net solar radiation should be in balance with F [the net LWIR flux emitted to space]. Since the net incoming solar radiation would not change with the addition of chlorofluorocarbons, the energy balance condition implies that F has to be the same for the perturbed and the unperturbed atmosphere.* Ramamathan, 1975

He simply accepted the invalid equilibrium climate assumption and did not conduct any detailed energy transfer analysis. The heat released by the initial greenhouse gas radiative forcing or decrease in LWIR flux at TOA is radiated back to space at TOA as wideband LWIR emission (see Fig. 20b). There is no significant change to the energy balance of the earth. Any tropospheric heating effects are too small to be detected in the turbulent boundary layer near the surface. There is no accumulation of heat over time.

The downward LWIR flux from the lower troposphere to the surface establishes a partial LWIR exchange energy with the upward LWIR flux emitted by the surface. When the surface and surface air layer are at similar temperatures, within the main tropospheric absorption emission bands, IR photons are exchanged without any significant transfer of thermal energy. The net LWIR cooling flux (upward minus downward LWIR flux) at the surface is limited to the emission into the LWIR atmospheric transmission window. This net LWIR flux is insufficient to dissipate the absorbed solar insolation. The surface warms up so that the excess solar heat is removed by moist convection. This drives the tropospheric heat engine. The net cooling flux changes with temperature, humidity and cloud cover. In particular, clouds are close to blackbody emitters. The downward LWIR flux from the cloud base 'fills in' the atmospheric LWIR transmission window. This is illustrated in Fig. 23. When the surface is warmer than the air layer above, the excess upward LWIR flux emitted by the surface outside of the LWIR transmission window is absorbed in the lower troposphere and can increase the convection, Clark and Rörsch (2023). The ocean-air and the land-air interfaces have different energy transfer properties and have to be analyzed separately.

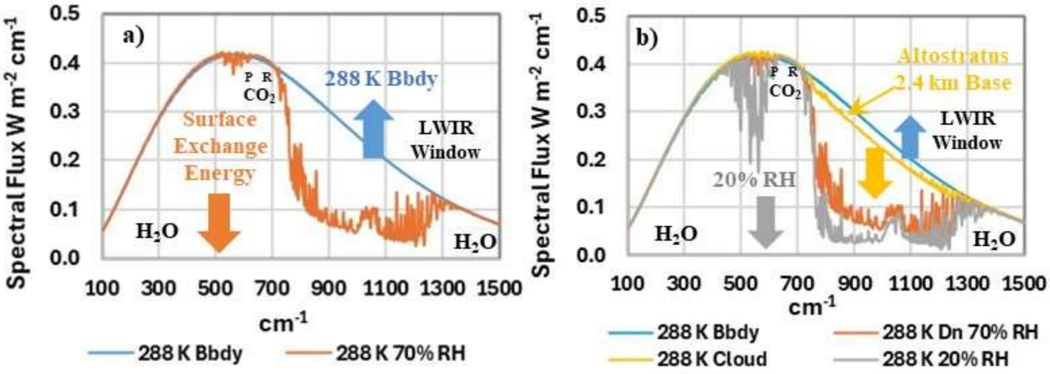

Figure 23: The surface exchange energy for surface and air temperatures of 288 K. a) Blackbody surface emission and downward LWIR flux for a relative humidity of 70% and CO_2 concentration of 400 ppm. The H_2O and CO_2 bands are indicated. b) Same as a) with the downward emission for 20% RH and for altostratus cloud cover with a 2.5 km cloud base added. MODTRAN calculations, 100 to 1500 cm^{-1} spectral range, 2 cm^{-1} spectral resolution, MODTRAN, (2024).

4.3 The Effect of an Increase in Atmospheric CO_2 Concentration on Ocean Surface Temperatures

Over the oceans, the surface is almost transparent to the solar flux. Approximately half is absorbed within the first meter layer and 90% is absorbed within the upper 10 m layer. The diurnal temperature rise is small and the bulk ocean temperature increases until the water vapor pressure is sufficient for the excess solar heat to be removed by wind driven evaporation. During the summer, at latitudes outside of the tropics, the solar heating exceeds the surface cooling. The lower sub-surface layers are not coupled to the surface by convective mixing and a stable thermal gradient is established. During the winter, the surface cooling exceeds the solar heating and the surface temperatures cool and establish a uniform temperature layer down to 100 m or lower depths. The monthly temperature profiles for 2018 from 2.5 to 200 m depth for a 5° x 1° strip (longitude x latitude) centered at 30° N, 20° W in the N. Atlantic Ocean are shown in Fig. 24, Clark and Rörsch (2023). The data are from the Argo Marine Atlas (2021). In summer, the ocean surface layers to a depth of 30 m reach a temperature of 24 °C. In winter the temperatures decrease to 19 °C to a depth of 100 m. The surface temperature phase shift or time delay between the peak solar flux and the peak ocean temperatures response is approximately 10 weeks. At 60 m depth it is 18 weeks. The phase shifts or time delays are clear evidence of a non-equilibrium thermal response, Clark (2023). At higher latitudes, the ocean temperature profiles follow a similar pattern to that shown in Fig. 24, with lower temperatures. The amount of heat stored and released over a year may easily reach 1000 MJ m^{-2} for a 1 m^2 water column extending down to 100 m depth. There is no requirement for an exact flux balance between the solar heating and surface cooling of the oceans.

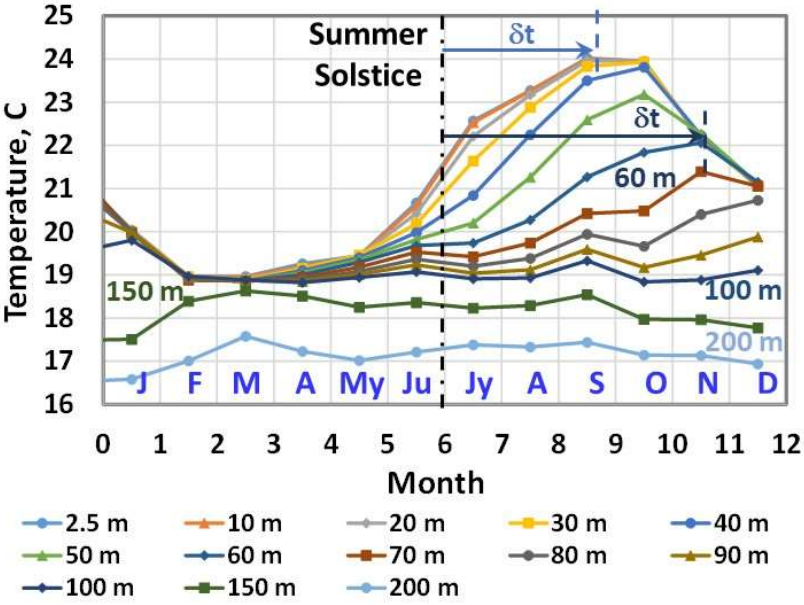

Figure 24: Monthly ocean temperatures at 30° N, 20° W and 2.5 to 200 m depth from 2018 Argo float data.

Long term (1958-2006) zonal latitude band averages of the air and surface temperatures, the latent heat and sensible heat flux, the wind speed and the absolute humidity are shown in Figs. 25a through 25f, adapted from Yu et al (2008). The penetration depth of the LWIR flux into the ocean surface is less than 100 micron (0.004 inches), Hale and Querry (1973). This is illustrated in Figure 26. The net LWIR cooling flux removes heat from this surface layer. The wind driven evaporation or latent heat flux is the removal of water molecules from the surface. The sensible heat flux is the transfer of thermal energy from the water surface to the air layer above. The cooler water produced by these three processes is mixed within a thin surface layer and then sinks. It is replaced by warmer water from below. This allows the evaporation to continue at night. The surface cooling processes are illustrated schematically in Fig. 27. There is a surface or skin layer that is cooler than the bulk ocean underneath. This establishes a thermal gradient close to the surface that enables the heat removed by the surface cooling to be replaced by thermal conduction from the warmer water layer below. The cooler skin layer has to be included in the determination of ocean surface temperatures using remote sensing techniques, Donlon et al (2002), Gentemann et al (2004).

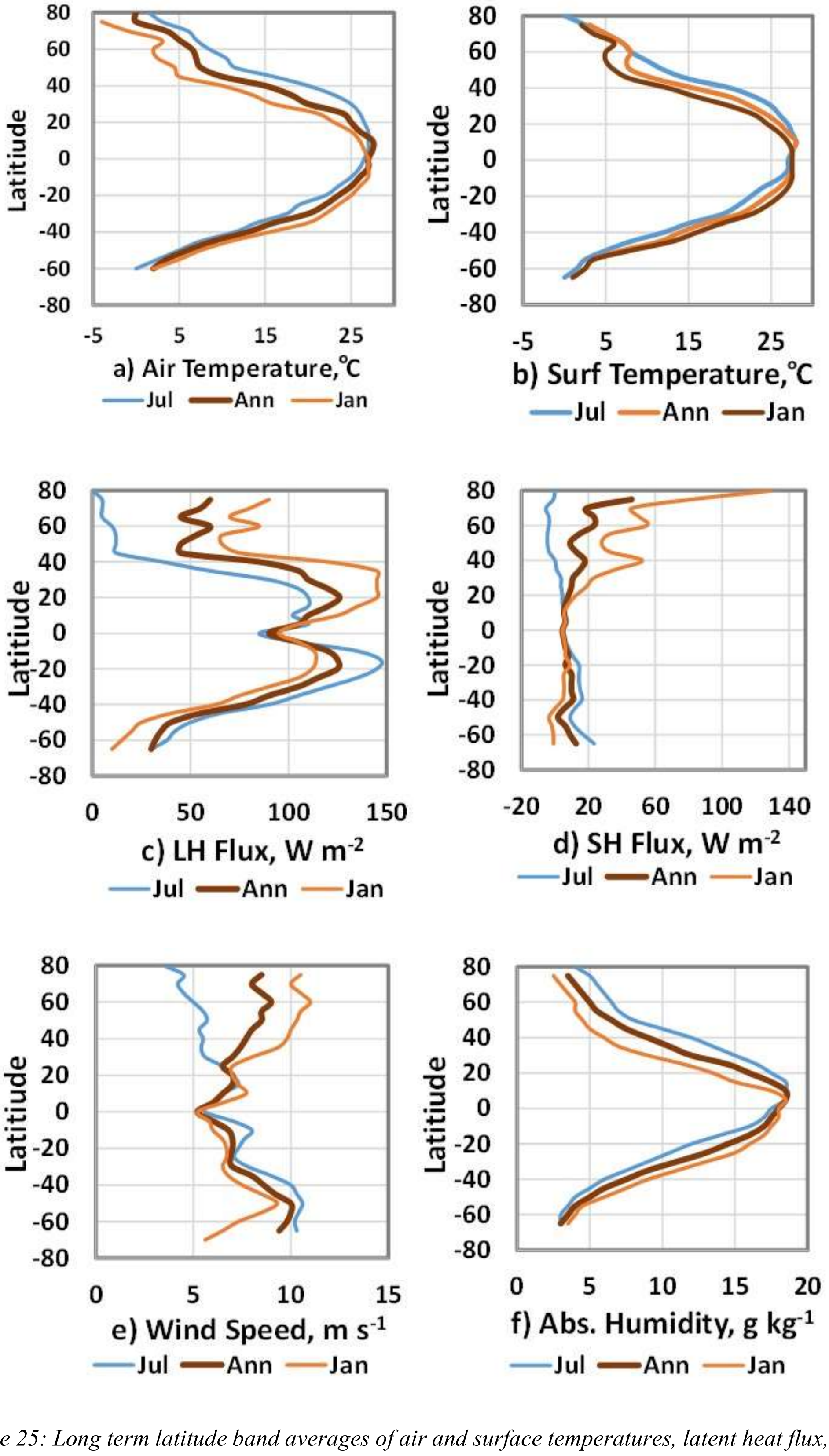

Figure 25: Long term latitude band averages of air and surface temperatures, latent heat flux, sensible heat flux, wind speed and absolute humidity. Annual averages and the values for July and January are shown. Adapted from Yu et al (2008).

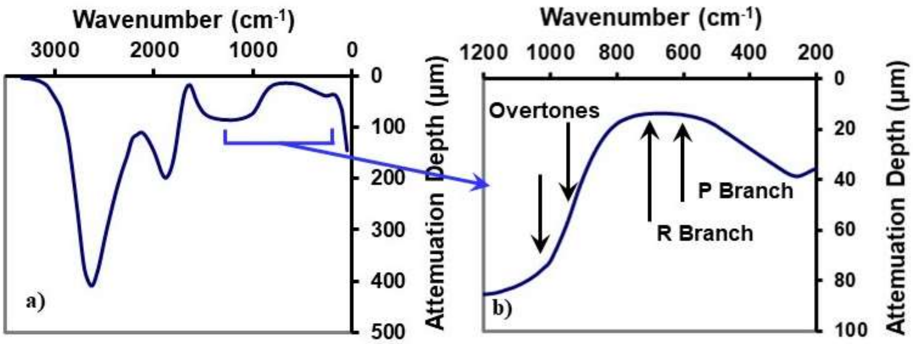

Figure 26: The penetration depth (99% absorption) of the LWIR flux into water a) below 3300 cm^{-1} and b) 1200 to 200 cm^{-1}. The locations of the main CO$_2$ absorption bands and the overtones are indicated.

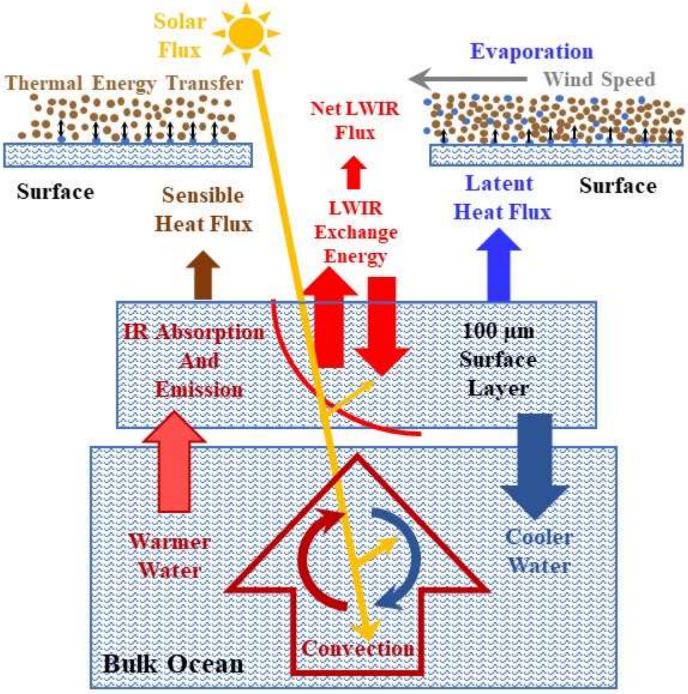

Figure 27: Ocean cooling (schematic): heat is removed from the surface by wind driven evaporation (latent heat flux) and the sensible heat flux. The net LWIR cooling flux removes heat from the first 100 micron layer. The cooler water produced by these three processes is combined in the surface layer, sinks and cools the bulk ocean below.

Ocean energy transfer involves the interaction between two very different thermal reservoirs. There is a large solar heated reservoir that may extend to over 100 m in depth. However, the initial cooling is limited to a thin surface reservoir that is less than 1 mm thick. Heat is also transported by ocean currents within the ocean gyre circulation (see Fig. 51). There are short term fluctuations in the LWIR flux and latent heat flux that do not produce a significant change in surface temperature. In signal processing terms, this is noise. There are also longer term changes in the surface cooling that produce variations in ocean surface temperature over different time scales. Increases in winter wind speed at higher latitudes enhance both the sensible and latent heat fluxes. Changes in wind speed over periods of a few years lead to quasi-periodic variations in tropical ocean temperatures including the El Niño Southern Oscillation (ENSO) and the Indian Ocean Dipole (IOD). There are also changes in wind speed over decadal time scales that are related to the AMO and the Pacific Decadal Oscillation (PDO). Ocean oscillations are considered in more detail in Sections 4.5 and 5.2.

Using the available hourly data for 2006 to 2024 from the TRITON buoy located at 170° W, 0° N (on the equator), the long term averages of the latent heat flux and the net LWIR flux are 105 ±39 W m^{-2} and 53 ±15 W m^{-2} (1σ standard deviation), TRITON (2024). There are large blocks of missing data. Approximately 40,400 hourly data points were recorded over 154,000 hours. This is a capture rate near 26%. These latent heat and LWIR fluxes give a combined surface cooling rate of 158 ±42 W m^{-2}. The main source of fluctuations or noise in the LWIR flux is the change in the downward LWIR flux produced by variations in cloud cover (see Fig. 23). For the latent heat flux, it is changes in the wind speed. Fig. 28a shows the 10 minute average RH (%) recorded for the first 6 months of 2016. Fig. 28b shows the hourly average wind speed and Fig. 28c shows the hourly average net LWIR flux and latent heat flux for the same time period.

The sensitivity of the latent heat flux to the wind speed may be estimated using the long term zonal averages of the latent heat flux and the wind speed from Figs. 25c and 25e. This is shown in Fig. 29. Within the ±30° latitude bands this sensitivity is at least 15 W m^{-2} for a change in wind speed of 1 m s^{-1}. Here, a 2 W m^{-2} decrease in net LWIR cooling flux is dissipated by an increase in wind speed near 13 m s^{-1}. For comparison, the long term 1σ variation in wind speed along the equator, recorded by the TRITON buoy network is near 2 m s^{-1}, Clark and Rörsch (2023).

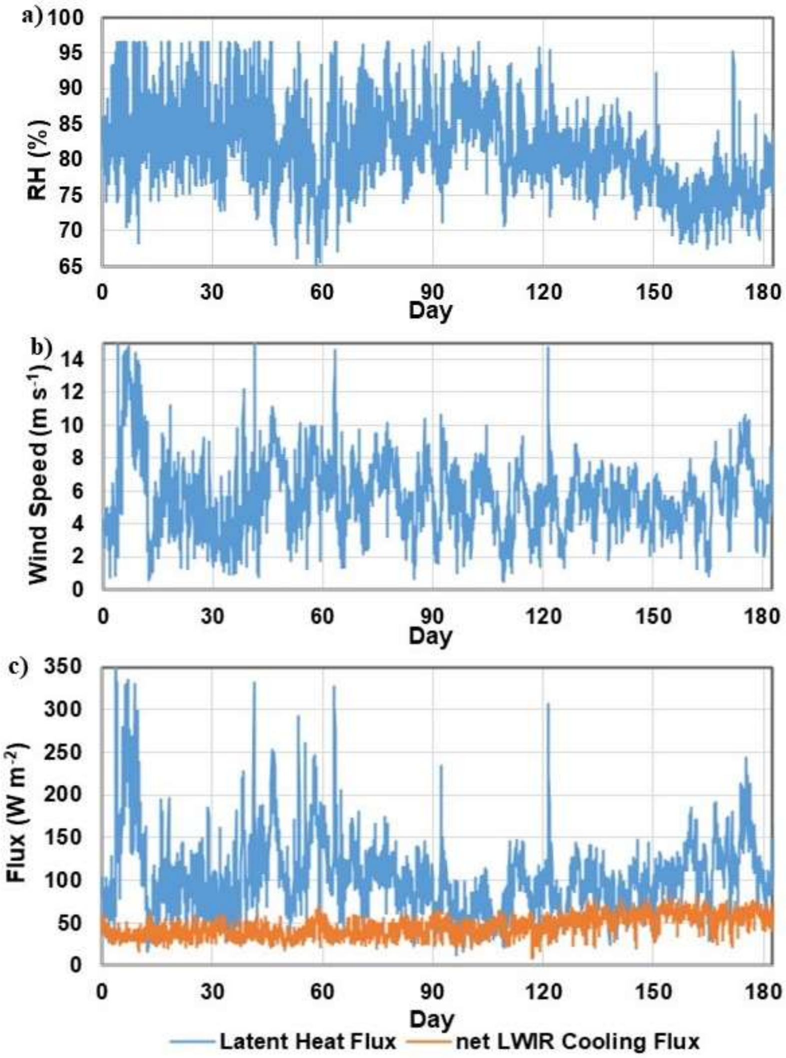

Figure 28: Short term average data recorded for the first six months of 2016 by the TRITON buoy at 170° W, 0° N (equator): a) 10-minute average relative humidity, b) 1-hour average wind speed and c) 1-hour average latent heat and net LWIR fluxes.

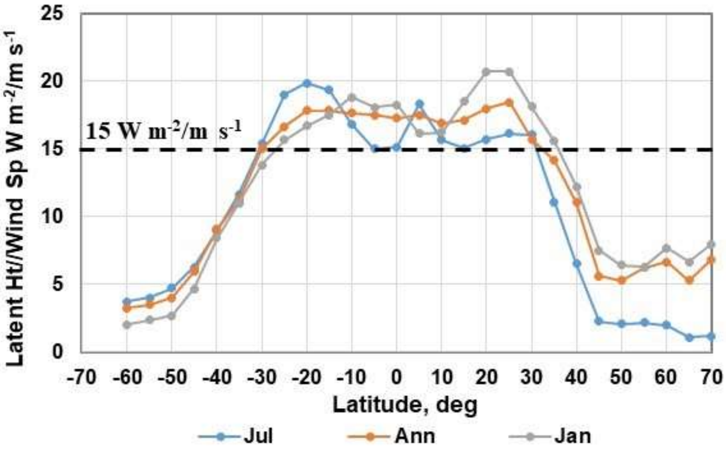

Figure 29: The sensitivity of the ocean latent heat flux to the wind speed. Based on data from Yu et al (2008).

The immediate cause of the ENSO is a change in the energy balance at the ocean surface between the solar heating and wind driven evaporation produced by a change in wind speed. The 2016 ENSO peak was produced by a decrease in wind speed of approximately 2 m s^{-1} over a period of 6 months. The corresponding decrease in latent heat flux was near 30 W m^{-2} and the temperature increase of 2.5 °C extended to a depth of at least 75 m. The related increase in ocean heat content was approximately 800 MJ m^{-2} for a 1 x 1 x 75 m water column. Over a six month period, the cumulative increase in downward LWIR flux to the surface produced by the increase in CO_2 concentration was near 0.26 MJ m^{-2}. The change in ocean heat content was approximately 3000 times larger than the cumulative increase in the downward LWIR flux from CO_2 (see Section 5.2 for further details).

Over large areas of the oceans, the sensible heat flux is less than 10 W m^{-2}. However, there is a significant increase in winter sensible heat flux at higher N. latitudes as shown in Fig. 25d. This is produced by an increase in winter wind speed as shown in Fig. 25e. The latent heat flux also increases. Part of the increase in winter cooling flux is produced by seasonal storms that increase the cold air flow from N. America across the warm water flow associated with the Gulf Stream. Within the area bounded by 30° to 42° N and 70° to 50° W, the long term (1947-2007) daily average sensible and latent heat fluxes are shown in Fig. 30, adapted from Shaman et al (2010). The summer to winter increases in the sensible and latent heat fluxes are 70 and 140 W m^{-2}.

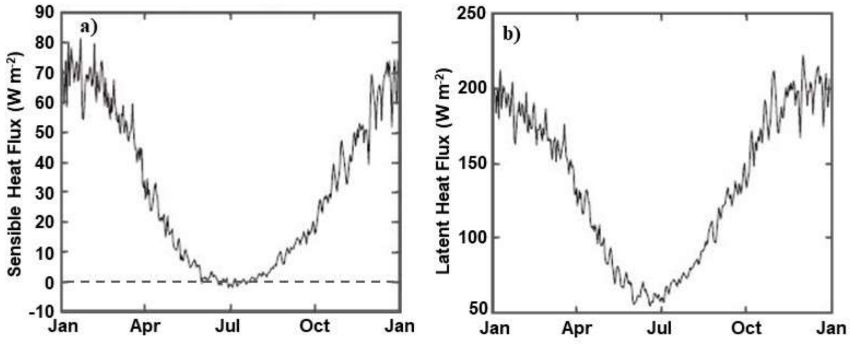

Figure 30: Long term (1947-2007) daily average sensible heat flux (a) and latent heat flux (b) for the area bounded by 30° to 42° N and 70° to 50° W that includes part of the Gulf stream off the coast of N. America.

The variation in the annual mean evaporation rate for the global ice free oceans from 1958 to 2005 is shown in Fig. 31, adapted from Yu, (2007). There was an increase in evaporation rate of 11 cm per year from 103 cm per year in 1977 to a peak of 114 cm per year in 2003. This is an increase in average latent heat flux of approximately 8.5 W m^{-2}. For reference, a latent heat flux of 2 W m^{-2} corresponds to an evaporation rate of 2.6 cm year^{-1}. The increase in evaporation is attributed to an increase in winter wind speed in both hemispheres.

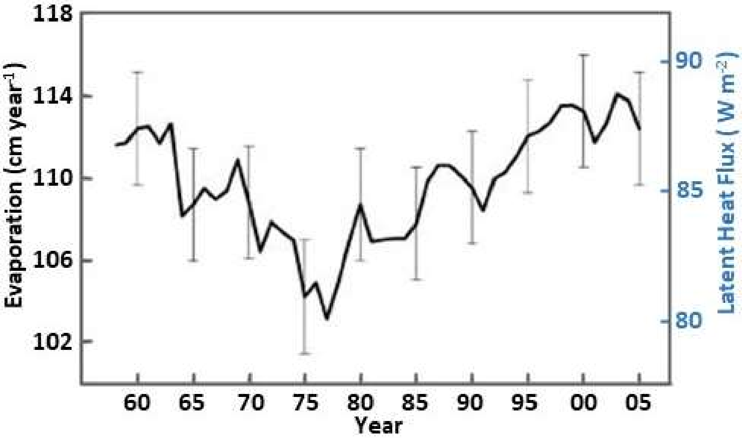

Figure 31: Average change in the global evaporation rate from 1958 to 2005. The corresponding changes in the average latent heat flux are also indicated.

The IPCC assumes that the surface responds to greenhouse gas radiative forcing with an increase in surface temperature that is amplified by a water vapor feedback, Knutti and Hegerl (2008). However, the quantitative details of the ocean surface energy transfer related to this process have not been considered. As shown above in Fig. 18b, the observed increase in the atmospheric CO_2 concentration of 140 ppm since 1800 has produced an increase in the downward LWIR flux to the surface of approximately 2 W m^{-2}. This is coupled to the surface thermal reservoir where it reduces the net LWIR cooling flux. However, the increase of 2 W m^{-2} has occurred gradually over time. At present, the average annual increase in downward LWIR flux is approximately 0.034 W m^{-2} or 34 milliwatts m^{-2} per year.

The net LWIR cooling flux, Q_{irnet}, can be simplified for discussion purposes by using Stefan's Law modified with a variable atmospheric spectral window:

$$Q_{irnet} = \sigma(\varepsilon T_s^4 - T_a^4) + Q_{winRH} - Q_{wincld} \qquad (2)$$

Here, σ is Stefan's constant, ε is the surface emissivity, T_s is the surface temperature, T_a is the surface air temperature (both in Kelvin), ΔQ_{winRH} is the humidity dependent LWIR cooling flux and Q_{wincld} is the downward LWIR flux from clouds (see Fig. 23b).

The latent heat flux, Q_{lh}, is given by:

$$Q_{lh} = k_{lat}(P_{Tws} - R_h P_{Twa})U \qquad (3)$$

Here, k_{lat} is an empirical constant, P_{Tws} is the saturated water vapor concentration at the surface temperature T_s, P_{Twa} is the saturated water vapor concentration at the surface air temperature T_a, R_h is the relative humidity and U is the wind speed, Clark and Rörsch (2023).

The increase in surface temperature needed to produce an increase in cooling flux of 2 W m^{-2} may be evaluated by combining equations (2) and (3). Setting $\varepsilon = 0.95$, $Q_{winRH} = 45$ W m^{-2}, $Q_{wincld} = 0$, $k_{lat} = 3$, RH = 80%, U = 6 m s^{-1}, with $T_a = T_s - 1$, gives:

$$Q_{irnet} + Q_{lh} = \sigma(0.95 * T_s^4 - (T_s - 1)^4) + 45 + k_{lat}(P_{Tws} - 0.8 * P_{Twa}) * 6 \qquad (4)$$

The water vapor pressure is calculated using a polynomial fit to the temperature. The increase in T_s is calculated using the 'goal seek' algorithm in Excel. The air temperature is not changed and only T_s is increased in the calculation. At 30 °C, (4) gives a value of 108 W m^{-2} for the latent heat flux. This is similar to the values of the latent heat flux at ±10° latitude in Fig. 25c.

Fig. 32a shows the increase in temperature needed to increase the cooling flux by 2 W m^{-2} for ocean surface temperatures from 0 to 34 °C. The blue line shows the temperature rise needed to increase just the LWIR surface emission by 2 W m^{-2} without any coupling to the latent heat flux. The orange line shows the temperature rise needed for the combined LWIR and latent heat flux. At a surface temperature of 0 °C, the increase is 0.45 °C for the LWIR flux and 0.19 °C for the combined flux. These values decrease to 0.33 °C and 0.06 °C at a surface temperature of 30 °C. Fig 32b shows the separate contributions of the LWIR and the latent heat fluxes to the 2 W m^{-2} increase in cooling flux vs. ocean surface temperature. As the temperature increases from 0 to 30 °C the latent heat fraction increases from 58% to 83%.

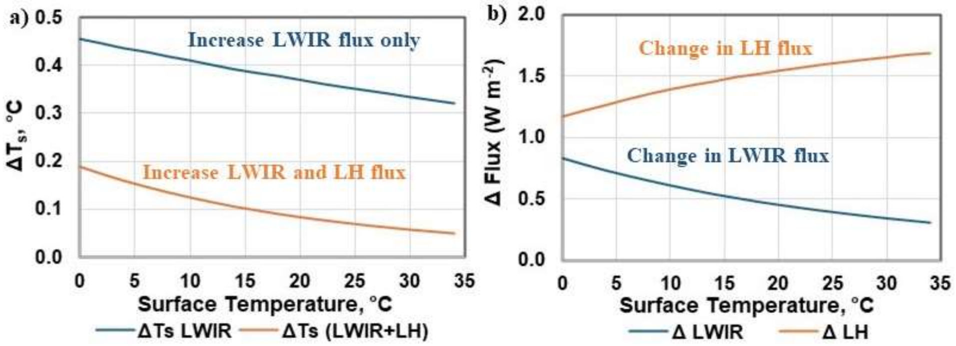

Figure 32: a) The increase in surface temperature needed to increase the LWIR flux (blue line) and the LWIR + latent heat flux (orange line) by 2 W m^{-2} as the surface temperature is increased from 0 to 34 °C. b) The separate contributions of the latent heat flux and LWIR flux to the 2 W m^{-2} total cooling flux increase vs. increase in ocean surface temperature.

This simple analysis indicates that the inclusion of the latent heat flux in the surface energy transfer produces a negative feedback. This was discussed by Harde (2017; 2014) as evaporation feedback. Part of the increase in downward LWIR flux to the surface is converted to latent heat. The additional evaporation increases the surface humidity gradient. The water molecules removed from the surface are entrained in the air flow and removed as moist convection. There is no amplification of the surface temperature by an increase in water vapor concentration in the air layer above the surface. These effects are also small compared to both the short term and longer term variations in the surface cooling flux. The IPCC assumptions that a greenhouse gas radiative forcing increases the surface temperature and that this is then amplified by a water vapor feedback require further evaluation.

4.4 The Effect of an Increase in Atmospheric CO_2 Concentration on Land Surface Temperatures

Over land, all of the flux terms are absorbed by a thin surface layer. The surface temperature initially increases after sunrise as the solar flux is absorbed. This establishes a thermal gradient with both the cooler air above and the subsurface ground layers below. The surface-air gradient drives the evapotranspiration (moist convection) and the subsurface gradient conducts heat below the surface during the first part of the day after sunrise. Later in the day, as the surface cools, the subsurface gradient reverses and the stored heat is returned to the surface. As the land and air temperatures equalize in the evening, the convection stops and the surface cools more slowly by net LWIR emission. This convection transition temperature is reset each day by the local weather system passing through. Almost all of the absorbed solar heat is dissipated within the same diurnal cycle. The heat transfer is localized. The diurnal temperature change is limited to a shallow depth, typically 0.5 to 2 m, and the seasonal temperature variations may extend to 5 m below the surface, Clark and Rörsch (2023). There are also characteristic phase shifts or time delays between the peak solar flux and the temperature response. This is not a recent discovery. The subsurface seasonal phase shift was described by Fourier (1824). Further details are given by Clark (2023). The soil temperatures at depths from 0.5 to 80 cm and the 2 m air temperature recorded at a monitoring site at O'Neill, Neb., August 13, 1953 are shown in Fig. 33, Letteau and Davidson (1957). The surface temperature phase shift, δt, and the convection transition temperature are indicated. Below the surface, the temperature rise decreases and the phase shift increases with the depth. At the surface, the temperature rise is 22 °C. The surface air temperature increase at 1.5 m above the surface is 15 °C. There is almost no measurable diurnal phase shift below 50 cm depth.

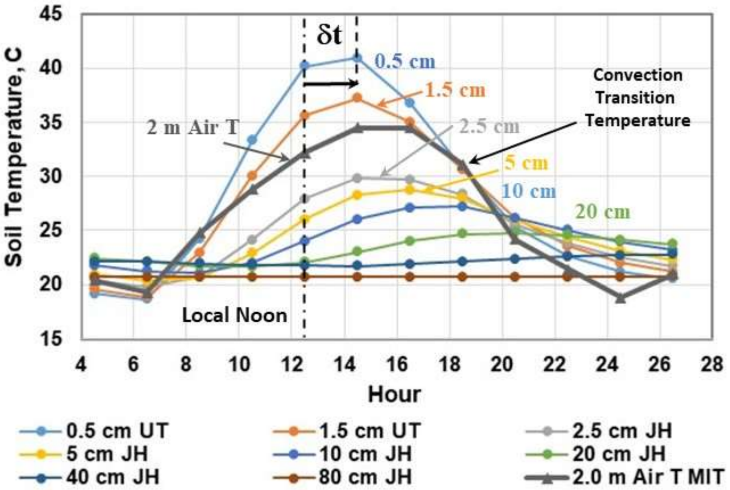

Figure 33: 2 m air temperature and subsurface temperatures recorded at O'Neill, Nebraska, August 13-14, 1953.

As shown above in Fig. 19c, almost all of the downward LWIR flux to the surface is emitted within the first 2 km layer of the troposphere and approximately half of this comes from within the first 100 m layer. Near the surface, both the relative and absolute humidity can change during the diurnal cycle. Figs. 34a and 34b show the relative and absolute humidity changes recorded at the O'Neill, Nebraska test site during the second observational period, August 13 to 14, 1953 related to the temperature changes shown in Fig. 33. The RH decreased from approximately 65% at 06:30 to 35% at 16:30 and then increased to approximately 70% by 02:30 the following morning. The absolute humidity increased from about 14 mbar at 02:30 to 20 mbar at 12:30 and decreased back to near 15 mbar by 00:30 the following morning. This is caused by evaporation from the warm surface during the day.

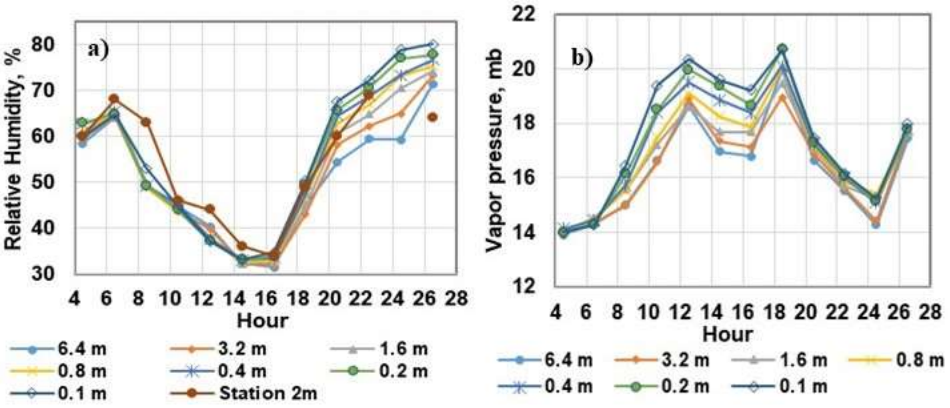

Figure 34: a) Relative humidity, % and b) absolute humidity, mbar recorded at O'Neill, Nebraska, August 13 - 14, 1953.

The fixed RH assumption also ignores the interactive coupling of the solar flux to the latent heat flux. Fig. 35 shows the total daytime and night time latent heat fluxes (MJ m^{-2} day^{-1}) recorded during the year 2008 at the Grasslands Ameriflux monitoring site located in Limestone Regional Park near Irvine, S. California. Almost all of the latent heat flux is produced during the day as the sun warms the vegetation and the surface. The peak latent heat flux occurs in March as the vegetation dries out after the winter rains. A total daytime flux of 6 MJ m^{-2} day^{-1} corresponds to an evaporation rate of approximately 140 W m^{-2}. In this region there is also a well-known transition from onshore to offshore flow. The onshore flow from the ocean brings lower temperatures and higher humidity. The offshore flow from the desert plateau produces higher temperatures and lower humidity. Fig. 36a shows the RH (%) and Fig. 36b shows the air temperature recorded over the year at half hour intervals. Some of the temperature spikes and low humidity related to the offshore flow are indicared by the dotted lines. Further details are provided by Clark and Rörsch (2023).

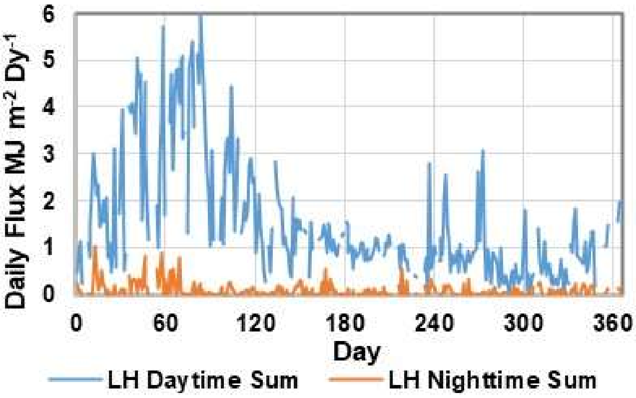

Figure 35: Total daytime and nighttime latent heat fluxes recorded at the Grasslands Ameriflux monitoring site near Irvine, CA during 2008.

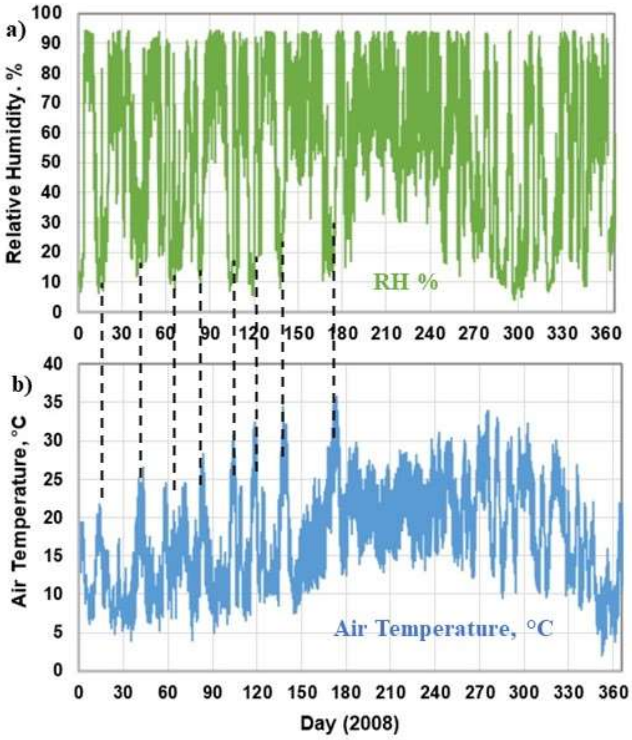

Figure 36: a) Half hour RH (%) and b) air temperature (°C) data recorded at the Grasslands site during 2008. Some of the temperature spikes and low himidity periods related to offshore flow are indicated with the dotted lines.

As discussed above in relation to Fig. 18, the average annual increase in the downward LWIR CO_2 flux from the lower troposphere to the surface is presently near 0.034 W m^{-2} yr^{-1}. This can have no measurable effect on the humidity in the surface boundary layer. The assumption of a fixed RH distribution used by M&W is not valid near the surface. Part of the absorbed solar flux can also be converted into latent heat flux. The diurnal and seasonal variations in the latent heat flux near the surface have been ignored. This contradicts the fixed RH distribution assumption used in MW67 that created the water vapor feedback.

The various flux terms interact with the surface and change the temperature at the land-air interface. However, the weather station temperature is the meteorological surface air temperature (MSAT) measured in a ventilated enclosure located at eye level, 1.5 to 2 m above the ground, Oke (2006). In general, the minimum MSAT and the minimum surface temperature are similar, but the maximum surface temperature is larger than the maximum MSAT, Clark and Rörsch (2023). The minimum and maximum temperatures are determined by different energy transfer processes. The minimum temperature is reset each day by the bulk surface air temperature of the local weather system passing through. The maximum surface temperature is set by the balance between the solar heating, the combined net LWIR flux and evapotranspiration (moist convection) and the subsurface thermal transport. The maximum MSAT is determined by the mixing of the warm air rising from the surface with the cooler air at the level of the MSAT thermometer. The important physical variables in the weather station temperature data are therefore the minimum MSAT and the delta T or difference between the maximum and minimum MSAT. The average MSAT, $(T_{max} + T_{min})/2$, has little useful meaning.

Starting in the early 1980s, the traditional white painted wooden Stevenson screen weather station enclosure fitted with Six's min/max thermometer was replaced by a smaller 'beehive' structure with an electronic thermometer, Quayle et al (1991). Since this has a faster response time, it is susceptible to short temperature transients that may bias the readings if the electronic signal is not averaged to simulate the thermal response time of six's thermometer, Hansen (2024). This may contribute to an observed warming in the weather station record.

To illustrate the normal variation in the MSAT record, the 1981 to 2010 thirty year daily climate averages for the O'Neill, Neb. weather station #256290 are shown in Fig. 37, WRCC (2022). The 1σ standard deviations and the ΔT (T_{max} - T_{min}) values are also shown. There is a phase shift of approximately 30 days between the peak solar flux at summer solstice, day 172 and the peak seasonal temperature response. In addition, the ΔT values remain within the approximate range 13.4 ±2 °C for the entire year while the temperature variation is ±10 °C. The 1σ temperature standard deviations increase from approximately 4 °C in summer to 8 °C in winter.

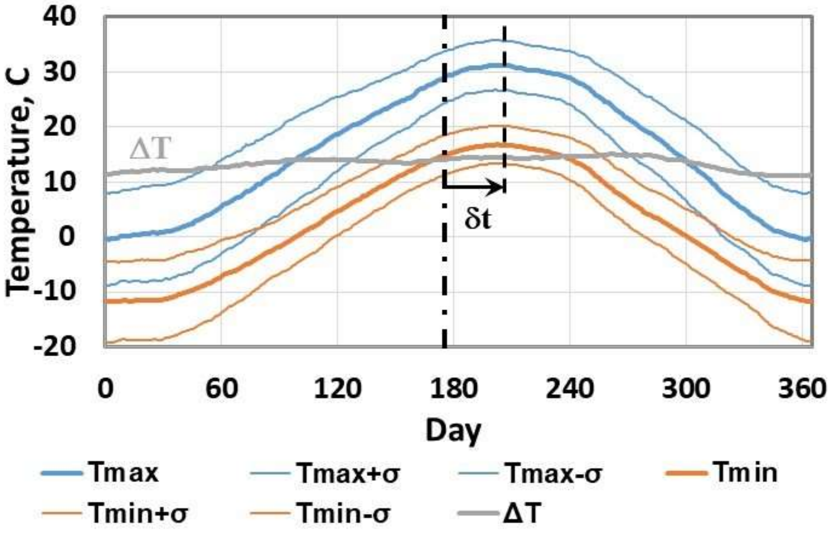

Figure 37: *1981-2010 daily climate averages for O'Neill, Neb., Station #256290. The 1σ standard deviations and the ΔT (T_{max} -T_{min}) are also shown. The seasonal phase shift, δt is indicated.*

A simple thermal engineering model of the surface and air temperatures recorded in 2008 at the Grasslands site was used to evaluate the effect of an increase in CO_2 concentration on land temperatures (Clark and Rörsch 2023; Clark, 2013a; 2013b). In this case, for a doubling of the CO_2

concentration from 280 to 560 ppm, the increase in MSAT was approximately 0.1 °C. This is too small to measure in the normal day to day variations in the convection transition temperature. In addition, the diurnal and seasonal phase shifts demonstrate that the surface thermal reservoir is not in thermal equilibrium, Clark (2023).

4.5 The Coupling of Ocean Surface Temperatures to the Weather Station Record.

Akasofu (2010) explained the global temperature record as a linear recovery from the LIA with multidecadal temperature oscillations superimposed as shown in Fig. 38. He used a wide range of proxy data in his analysis including ice core data, river freeze/breakup dates, sea level changes, sea ice changes, glacier changes, tree ring data and cosmic ray intensity data. He also proposed that the IPCC projections of climate warming attributed to greenhouse gas radiative forcings are an extrapolation of the latest warming phase of the multidecadal oscillation.

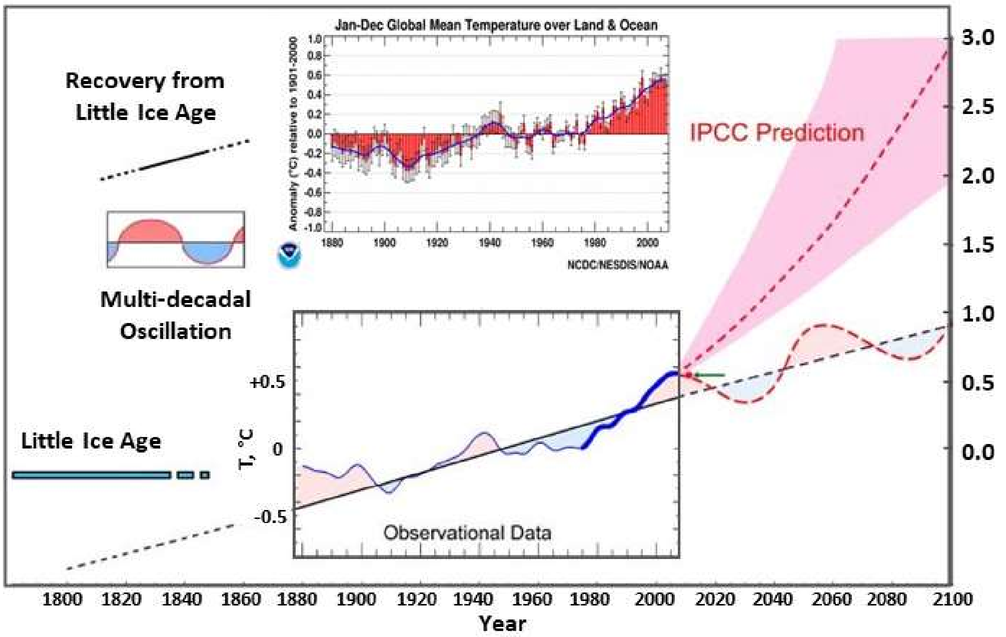

Figure 9. The figure shows that the linear trend between 1880 and 2000 is a continuation of the recovery from the LIA, together with the superimposed multi-decadal oscillation. It also shows the predicted temperature rise by the IPCC after 2000. It is assumed that the recovery from the LIA would continue to 2100, together with the superimposed multi-decadal oscillation. This view could explain the halting of the warming after 2000. The observed temperature in 2008 is shown by a red dot with a green arrow. It has been suggested by the IPCC that the thick blue lime portion was caused mostly by the greenhouse effect, so their future projection is a sort of extension of the blue line.

Figure 38: *The linear temperature recovery from the LIA with multi-decadal oscillations superimposed. Adapted from Akasofu (2010).*

When the climate temperature anomaly record, such as the HadCRUT4 data set is evaluated, the dominant term is found to be the AMO (HadCrut4, 2022; Morice et al, 2012). This is illustrated in Fig. 39a. The AMO is a long term quasi-periodic oscillation in the surface temperature of the N. Atlantic Ocean from 0° to 60° N, AMO (2022). Superimposed on the oscillation is a linear increase in temperature. This is the recovery from the LIA described by Akasofu (2010). The linear equation for the slope and the least squares fit to the oscillation are shown in Fig. 39a. Before 1970, the AMO and HadCRUT4 track quite closely. This includes both the long period oscillation and the short term fluctuations. There is an offset that starts near 1970 with HadCRUT4 approximately 0.3 °C higher than the AMO. The short term fluctuations are still similar. The correlation coefficient between the two data sets is 0.8. The influence of the AMO extends over large areas of N. America, Western Europe and parts of Africa. The weather systems that form over the oceans and move overland couple the ocean surface temperature to the weather station data through the diurnal convection transition temperature, Clark and Rorsch (2023). The contributions of the other ocean oscillations to the global temperature anomaly are smaller. The IOD and the PDO are dipoles that tend to cancel and the ENSO is limited to a relatively small area of the tropical Pacific Ocean. However, small surface temperature variations in the tropical oceans have a major impact on ocean evaporation and rainfall. Fig. 39b shows a tree ring construction of the AMO from 1567 (Gray et al, 2004a; 2004b). The modern instrument record is also indicated in green.

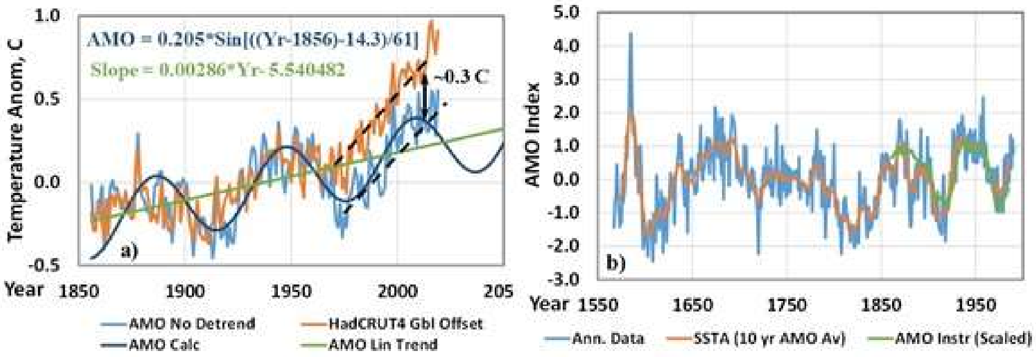

Figure 39: a) Plots of the HadCRUT4 and AMO temperature anomalies overlapped to show the similarities. Both the long term 60 year oscillation and the shorter term 'fingerprint' details can be seen in both plots. The role of 'adjustments' in the 0.3 °C offset since 1970 requires further investigation. b) Tree ring reconstruction of the AMO from 1567.

There is still an additional part of the recent HadCRUT4 warming that is not included in the AMO signal. This may be explained as a combination of three factors. First there are urban heat islands related to population growth that were not part of the earlier record. Second, the mix of urban and rural weather stations used to create the global record has changed. Third, there are so called 'homogenization' adjustments that have been made to the raw temperature data. These include the 'infilling' of missing data and adjustments to correct for 'bias' related to changes in weather station location and instrumentation. It has been estimated that half of the warming in the global record has been created by such adjustments. This has been considered in more detail for example by Andrews (2001a; 2017b; and 2017c), D'Aleo and Watts (2010), Berger and Sherrington (2022) and O'Neill et al (2022). The effect of the changes to the urban/rural weather station mix, adapted from D'Aleo and Watts (2010) is shown in Fig. 40.

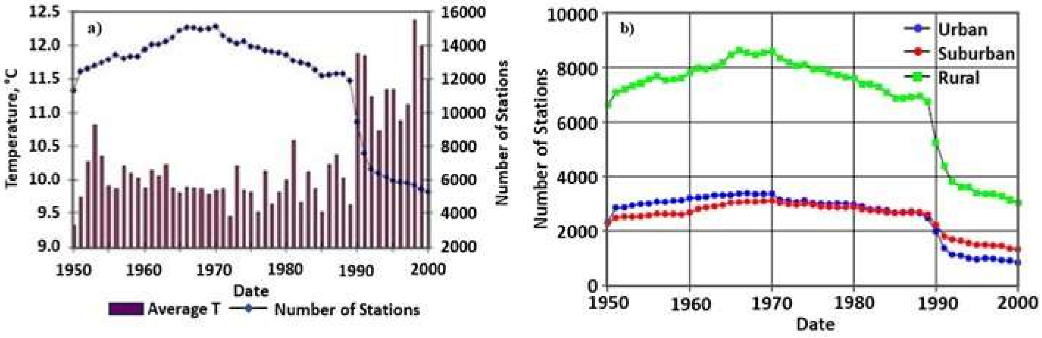

Figure 40: a) Changes in the number of stations used in the global average from 1950 to 2000 and the average temperatures. b) Changes in the number of stations by category from 1950 to 2000.

The role of the AMO in setting the surface air temperature has been misunderstood or ignored for a long time. The first person to claim a measurable warming from an increase in CO_2 concentration was Callendar (1938). The warming that he observed was from the 1910 to 1940 warming phase of the AMO and not from CO_2. During the 1970s there was a global cooling scare that was based on the cooling phase of the AMO from 1940 to 1970 (McFarlane, 2018; Peterson et al, 2008; Bryson and Dittberner, 1976). In H81, Hansen et al overlooked the 1940 AMO peak in their analysis of the effects of CO_2 on the weather station record (see Fig. 10e). Similarly, Jones et al overlooked the 1940 AMO peak when they started to ramp up the modern global warming claims (Jones et al, 1986; 1988). The IPCC also ignored the AMO peak in its First Assessment Report (FAR WG1 fig. 11 SPM p. 29, IPCC 1990) and it has continued to ignore it as shown in the recent Sixth Assessment Report (AR6 WG1 TS CS Box 1 fig. 1c p. 61, IPCC 2021). This is illustrated in Fig. 41. The AMO and the periods of record used are shown in Figure 41a. The temperature records used by Callendar, Douglas, Jones et al, Hansen et al and IPCC 1990 and 2021 are shown in Figs. 41b through 41g. The increase in atmospheric CO_2 concentration is also shown in Figs. 41d through 41g (Keeling, 2023).

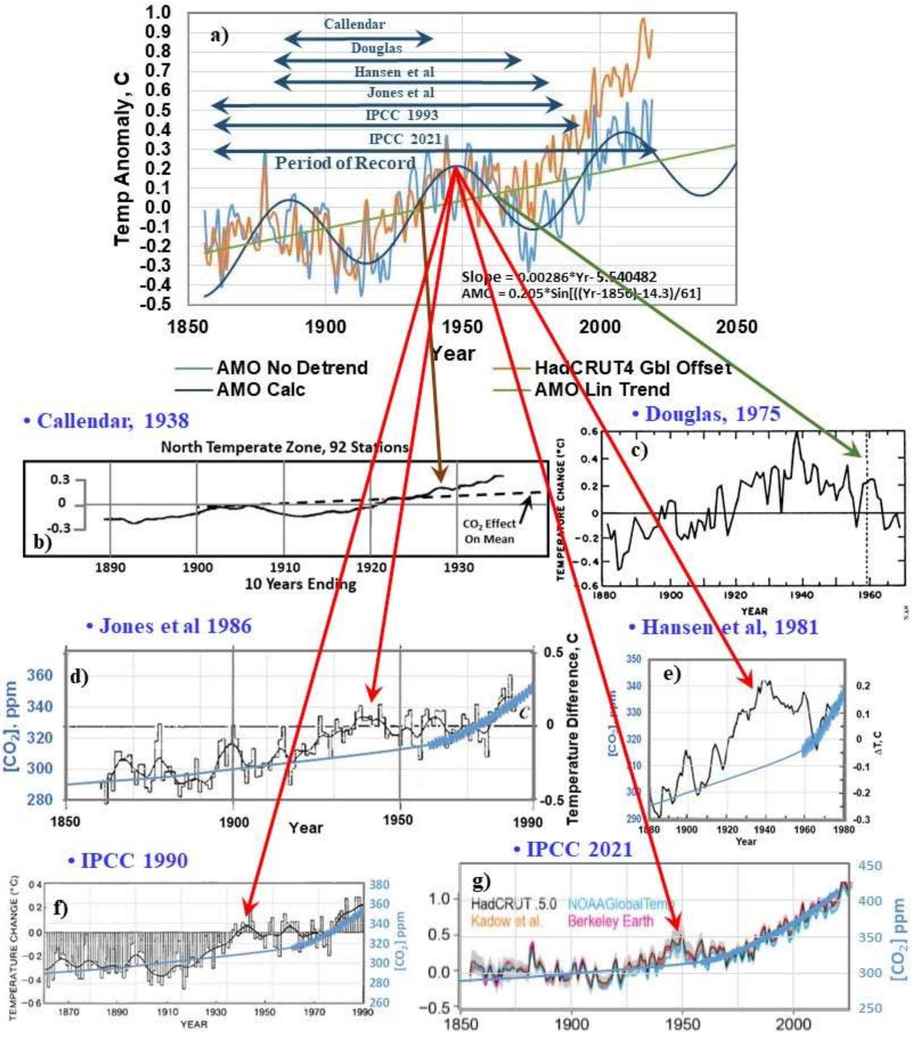

Figure 41: *a) AMO anomaly and HadCRUT4 global temperature anomaly, aligned from 1860 to 1970, b) temperature anomaly for N. temperate stations from Callendar (1938), c) global cooling from Douglas (1975), d) global temperature anomaly from Jones et al, (1986) e) global temperature anomaly from Hansen et al, (1981), f) and g) global temperature anomalies from IPCC (1990) and IPCC (2021). The changes in* CO_2 *concentration (Keeling curve) are also shown in d) through g). The periods of record for the weather station data are also indicated in a).*

The large scale climate models are simply tuned to match the global mean temperature anomaly. There are two different ways that the climate sensitivity is determined. First, the CO_2 concentration is simply doubled and the model is run to equilibrium or steady state. This is called the equilibrium climate sensitivity (ECS). Second, the CO_2 concentration is increased gradually, usually by 1% per year. The temperature change at the CO_2 doubling point is called the transient climate response (TCR).

In order to validate the climate models, a similar exercise is applied in reverse to the measured global mean temperature record. This may be illustrated by considering the work of Otto et al, (2013). They defined the climate sensitivities as:

$$ECS = F_{2x}\Delta T/(\Delta F - \Delta Q) \quad (5a)$$

$$TCR = F_{2x}\Delta T/\Delta F \quad (5b)$$

Here, F_{2x} is the radiative forcing produced a doubling of the atmospheric CO_2 concentration, set in this case to 3.44 W m^{-2} for a doubling from 'preindustrial levels', 280 to 560 ppm, ΔF is the change in radiative forcing (W m^{-2}), ΔT (°C) is the change in global mean temperature and ΔQ is the change in the earth system heat content, also given in W m^{-2}. The change in temperature is taken from the HadCRUT4 global temperature anomaly and the radiative forcings are taken from the CMIP5/RCP4.5 model ensemble. The change in heat content is dominated by ocean heat uptake. The decadal temperature and forcing estimates from data given by Otto et al are shown in Figs. 42a and 42b. The 1910 AMO cycle minimum and the 1940 maximum are indicated. As discussed above in Section 4.3, the increase in the downward LWIR flux related to the radiative forcing shown in Fig. 42b is coupled to the ocean surface layer and does not have any measurable effect on the bulk ocean temperature below. Using the data from Figs. 34a and 34b combined with estimates of ΔQ from various sources, Otto et al assume that their net radiative forcing estimates are responsible for the observed heating effects and that the temperature response to the change in LWIR flux is linear. Plots of ΔT vs (ΔF-ΔQ) and ΔT vs ΔF are therefore presumed to be linear with a slope that changes with the value of ECS or TCR. The results generated by Otto et al are shown in Figs. 42c and 42d. Using the data for 2000 to 2010, they create an ECS of 2.0 °C with a 5-95% confidence interval of 1.2 to 3.9 °C and a TCS of 1.3 °C with a confidence level of 0.9 to 2.0 °C.

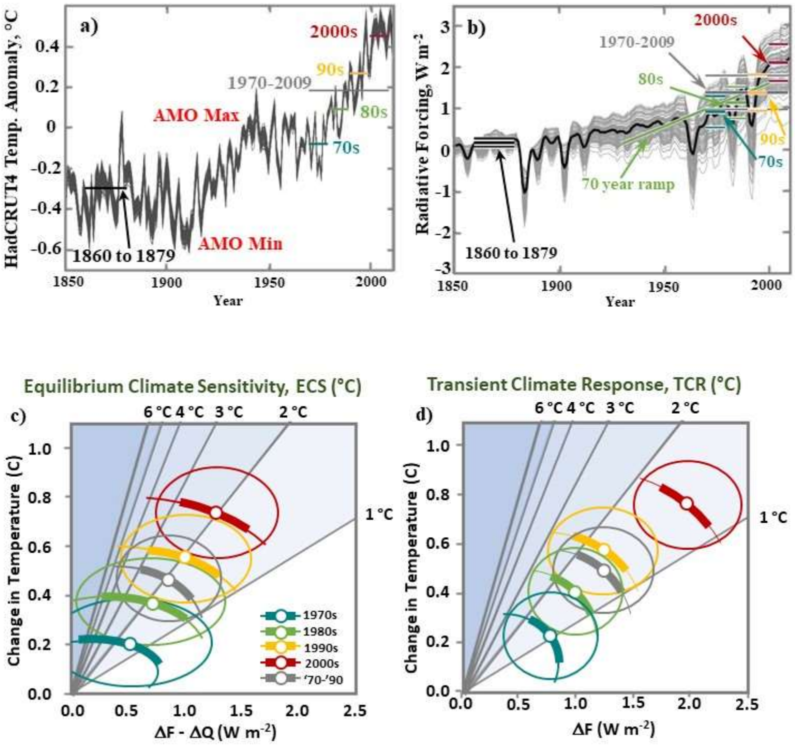

Figure 42: a) Decadal mean temperature estimates derived from the HadCRUT4 global mean temperature series. b) Decadal mean forcing with standard errors from the CMIP5 /RCP4.5 ensemble. c) Estimates of ECS and d) estimates of TCR. Data from Otto et al (2013).

4.6 Air Compression: The Neglected Heat Source

One of the more egregious applications of the equilibrium climate models has been the ‘attribution’ of ‘extreme’ natural weather events to increased CO_2 levels in the atmosphere. This is discussed above in Section 3.5. At present, the annual average increase in the atmospheric concentration of CO_2 is near 2.4 ppm per year. The corresponding annual increase in downward LWIR flux from the lower troposphere to the surface is 0.034 W m^{-2}. This can have no effect on such ‘extreme’ weather events. One of the main climate modeling errors has been the neglect of the heating produced by air compression. As dry air descends to lower altitudes, the lapse rate is +9.8 K km^{-1}. There are two different energy transfer processes that have to be considered. The first is heating by downslope winds and the second is the heating produced by the downward flow of air circulating within a high pressure system. These processes can produce temperature changes of 10 °C or more over a few days or less.

Downslope winds are well known in many regions of the world and there are many different names for the same effect. In S. California they are Santa Ana Winds. In N. California they are diablo winds. In the Rocky Mountains they are chinook (‘snow eating’) winds. In the Alps they are Föhn winds. A good example of the effect of downslope winds on temperature was recorded at Havre, Montana, December 16 to 18, 1933, Math (1934). At this time the CO_2 concentration was near 310 ppm. The thermograph trace is shown in Fig. 43a, adapted from Math (1934), fig.2. The temperature first rose by 27 °F (15 °C) in five minutes and increased by a total of 53 °F (29 °C) in less than 2 days. The temperature then cooled by 41 °F (23 °C) in two hours. There is no connection between these downslope wind events and any increase in atmospheric CO_2 concentration. Once the necessary weather pattern is established, the hot, dry winds will dry out the vegetation very quickly and any ignition source will start the fire. In S. California, a high pressure system over the Great Basin produces an offshore flow that descends from the desert plateau. The winds may be increased by an adjacent low pressure region. Fig. 43b is a Terra Satellite image taken on Dec. 5, 2017, showing the fires in S. California, NASA (2017). The smoke is blown out to sea by the offshore winds. The Marshall fire in Boulder Colorado, December 30, 2021, that destroyed about 1000 houses was caused by strong downslope winds and an ignition source related to human activity. The fuel was dry grass and any residual moisture would have been removed very quickly by the dry 100 mph winds, Mass (2022).

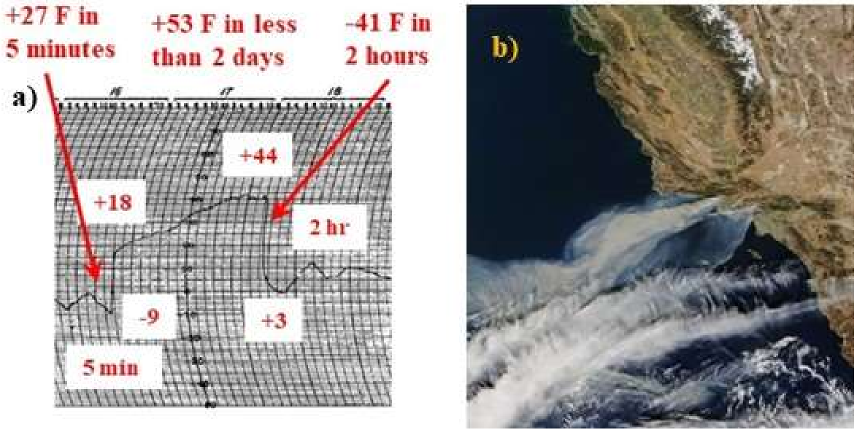

Figure 43: a) Thermograph trace of a downslope wind (Chinook) event, Havre Montana, December 1933, and b) Terra satellite image of the fires in S. California, taken Dec. 5, 2017.

A stationary or blocking high pressure system can produce significant warming over a period of several days, Clark and Rörsch (2023). None of this has any relationship to CO_2. A high pressure dome formed over the Pacific Northwest in late June 2021. This produced record high temperatures as shown in Fig. 44. As the high pressure system moved east, the temperature in Portland, Oregon dropped from 116 to 64 °F (47 to 18 °C) over the night of June 28 to 29, Watts (2021). Once a ‘blocking’ high pressure system pattern is established, it can persist for weeks or even months. Since these systems also block rainfall and remove soil moisture, additional heating is produced by the reduced latent heat flux at the surface. For example, there was nothing unusual about the 2003 European heat wave, Black et al (2004). Brush fires produced by 'blocking' high pressure systems are a normal part of the Australian climate, Foley (1947). Similarly, a high pressure system regularly forms over the area near Verkhoyansk, Siberia. This produces very high summer temperatures and very low winter temperatures (Autio, 2020; Watts, 2020).

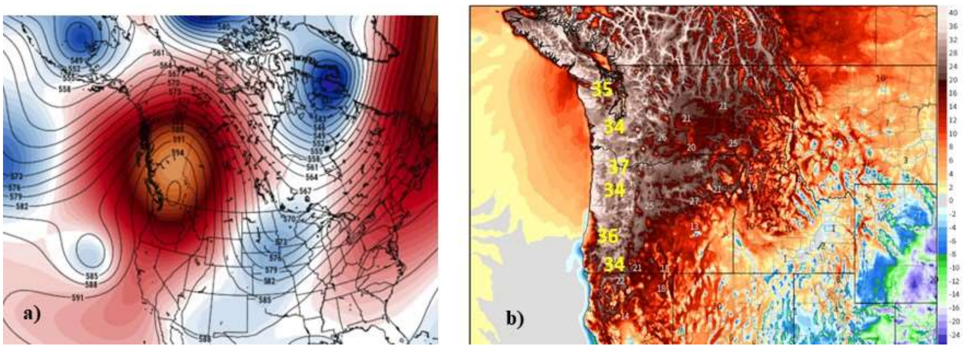

Figure 44: Blocking high pressure system over the Pacific NW, late June 2021. As the high pressure system moved east, the temperature in Portland Oregon dropped by 29 °C from 47 to 18 °C overnight, June 28 to 29.

4.7 The Dependence of the Atmospheric CO_2 Concentration on Ocean and Surface Temperatures

The analysis of the time dependent energy transfer processes that determine the surface temperature presented above in Sections 4.1 to 4.6 shows that the observed increase in CO_2 concentration of 140 ppm has not produced any measurable increase in surface temperature. Additional evidence that variations in the atmospheric concentration of CO_2 cannot cause climate change can be derived from the relationship between atmospheric CO_2 concentration and surface and ocean temperatures and from isotope studies. First, the time delays between the temperature changes and the CO_2 concentration response show that the temperature changes first and the CO_2 concentration then follows. Second, a large body of measurements contradict the ice core derived CO_2 concentrations. Third, a detailed analysis of the absorption and emission of CO_2 indicates that only a small fraction of the observed increase in CO_2 concentration can be attributed to anthropogenic causes. These areas will now be considered in turn.

Fig. 45 shows the relationship between the annual temperature changes in the HadCRUT4 and HadCRUT5 temperature series and the annual change in the CO_2 concentration measured at Mauna Loa from 1960 to 2004. The CO_2 response (green) lags the temperature response (red and blue) by 9 months to a year (Humlum, 2024; Humlum et al, 2012). Fig. 46 shows the temperature and CO_2 concentration data derived from the Vostok ice core. During the inception period (initial cooling) for each major glaciation, the decrease in CO_2 concentration lags the temperature by several thousand years, data from Mearns (2017). This is interpreted as a delay in the absorption of the CO_2 by the oceans as they cool.

The CO_2 concentration has been monitored at Mauna Loa using a non-dispersive IR technique since 1958, Keeling (2023). While this is now the preferred CO_2 monitoring method, a large number of CO_2 concentration measurements were made using conventional chemical analysis, some dating back to the early nineteenth century. A data set of these results has been compiled by Beck (2022). Fig. 47 shows the CO_2 concentration recorded for the marine boundary layer from 1870 to 1960 (adapted from Beck, fig. 25). The CO_2 concentration generally stays between 300 and 320 ppm from 1870 to 1930. There is a prominent CO_2 peak between 1935 and 1945 that reaches 380 ppm. The CO_2 concentration then decreases to values near 320 ppm for 1960 in agreement with the early CO_2 concentrations recorded at Mauna Loa. The blue crosses are the CO_2 concentrations derived from the Law Dome ice core. They are consistently lower than the Beck data and do not show the 1940 peak. The green stars are proxy CO_2 concentrations derived from leaf stomata data. Stomata are leaf pores used for gas exchange. The density of these pores is inversely proportional to the CO_2 concentration. These stomata results agree with the Beck data.

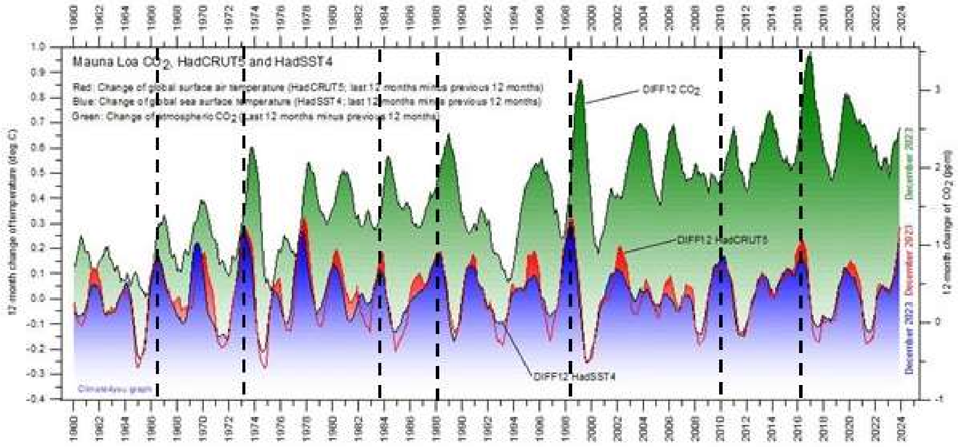

Figure 45: Annual changes in the HadCRUT4 and HadCRUT5 temperature series compared to the annual change in the CO_2 concentration measured at Mauna Loa. The increase in CO_2 concentration follows the temperature increase with a delay of 9 months to a year (Humlum, 2024).

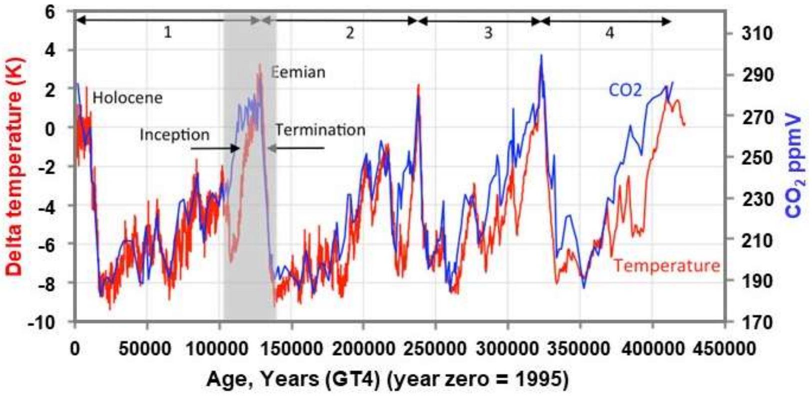

Figure 46: Temperature and CO_2 concentration data from the Vostok ice core. During the inception periods there is a major time delay between the temperature decrease and the CO_2 concentration response.

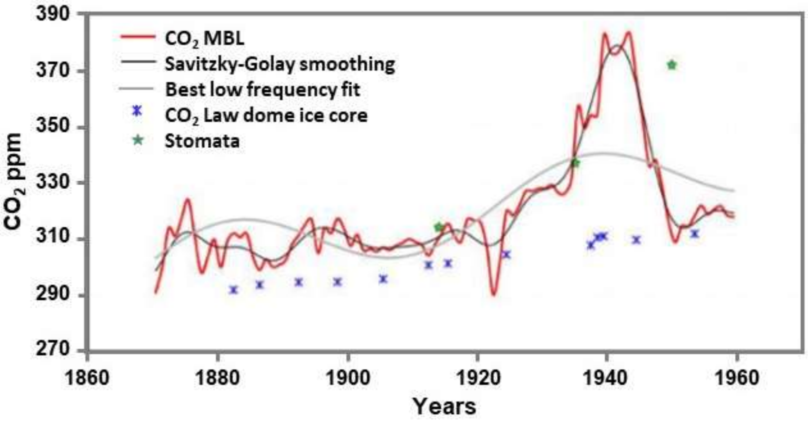

Figure 47: CO_2 concentration data measured in the marine boundary layer, 1870 to 1960 (red line), Law dome ice core data (blue crosses) and leaf stomata estimates (green stars), data from Beck (2022), figure 25.

Fig. 48 shows CO_2 concentrations derived from leaf stomata data obtained from lake sediment analysis for the time interval between 8,700 and 6800 years BP compared to Taylor Dome ice core data, from Wagner et al (2002). The leaf stomata results show a larger and more variable CO_2 concentration compared to the ice core data. The ice core data stays between 260 and 270 ppm. The leaf stomata data varies between 270 and 325 ppm. These results show that the CO_2 concentrations derived from ice core measurements are lower than those from other measurements. In addition, the time resolution is much coarser. In order for air bubbles to be trapped in the ice core, the snow deposited at the surface has to be compressed and converted to ice. The compressed snow is known as firn before it is fully converted to ice. During this compression process, physical and chemical changes occur that alter the CO_2 concentration. The drilling process may also alter the properties of the ice core. Measured ice core concentrations may be 30 to 50% lower than the real values. This is discussed by Jaworowski (2007).

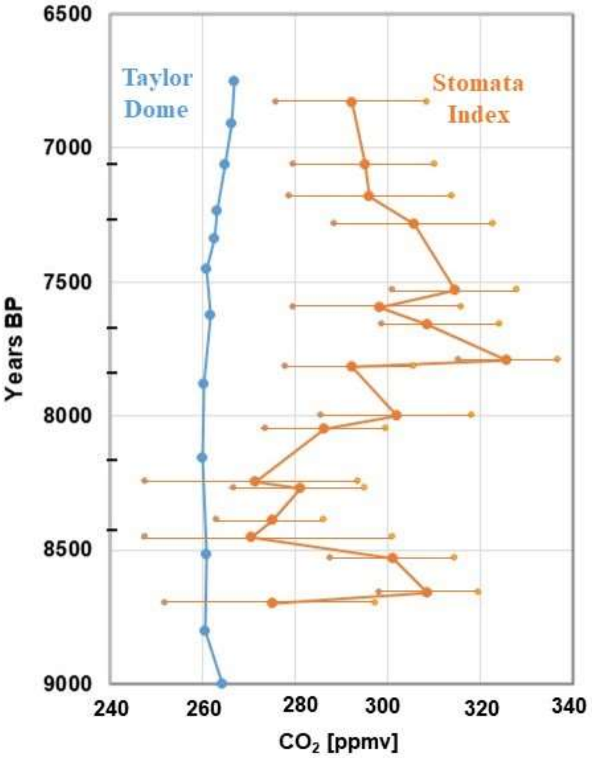

Figure 48: CO_2 concentration data from the Taylor Dome ice core compared to lake sediment leaf stomata index proxies for the period 8700 to 6800 BP.

The atmospheric concentration of CO_2 as recorded for example by the Mauna Loa Observatory, is determined by the dynamic balance between the emission and absorption of CO_2 at the earth's surface, Salby and Harde (2022a). The decline in $^{14}CO_2$ related to nuclear device testing that followed the 1963 nuclear test ban has provided a means for investigating the absorption of CO_2, Salby and Harde (2021a). The increase in atmospheric CO_2 concentration related to increases in tropical surface temperatures was then investigated, Salby and Harde (2021b). This study showed that the increase in tropical temperature over land was a major source of the observed increase in atmospheric CO_2 concentration. Further analysis was provided by Salby and Harde (2022b). This work demonstrated that the anthropogenic contribution to the observed increase in atmospheric CO_2 concentration was small. This is shown in Fig. 49 (Salby and Harde, 2022a, fig. 1).

A similar result was obtained by Koutsoyiannis (2024) using $\delta^{13}C$ analysis of the atmospheric CO_2 concentration from 1978, Keeling (2023) and the proxy record from 1520 to 1997, Böhm et al (2002). An anthropogenic CO_2 signal was not discernable in the ^{13}C isotope record.

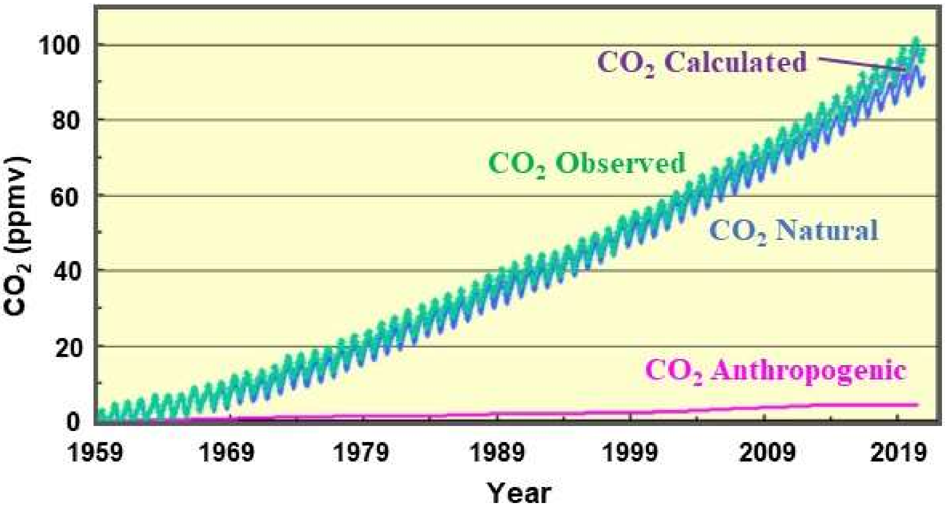

Figure 49: Measured (green) and calculated (purple) increase in CO_2 concentration from 1959. The contributions from thermally induced CO_2 emission (blue) and anthropogenic emission (magenta) are also shown. The calculated (purple) increase is almost hidden under the measured (green) line.

5. Climate Change Over Time

The earth's climate has been sufficiently stable over a period of several billion years (1 bn = 10^9) to allow for the evolution of life into its present forms. However, the climate has always changed over a wide range of time scales. Stellar evolution has produced a 20% increase in the solar flux over the last 2.5 billion years. The current composition of the atmosphere was established by photosynthesis and reached today's levels of approximately 78% nitrogen and 21% oxygen about 500,000 years ago. The atmospheric concentration of CO_2 has also varied from approximately 7000 ppm to 200 ppm. Plate tectonics has altered the distribution of the continents and caused major changes in ocean circulation. The present continental boundaries were formed by the breakup of the supercontinent Pangaea that started approximately 175 million years ago. Major ocean changes since then include the formation of the Southern Ocean and the separation of the Pacific and Atlantic Oceans by the Isthmus of Panama, Zachos et al (2001). In the more recent geological past, planetary perturbations of the earth's orbit known as Milankovitch cycles (2022) have produced a series of Ice Ages, each lasting approximately 100,000 years. Small changes in the solar energy reaching the earth related to the sunspot cycle that vary over periods of 100 to 1000 years have produced the Minoan, Roman and Medieval warming periods and the Maunder Minimum or Little Ice Age, Clark and Rörsch, (2023).

Approximately 71% of the earth's surface is ocean. The ocean-air interface involves the interaction of two fluids, air and water. The detailed description of these fluid interactions is complex and there is no simple mathematical solution, Lorenz (1963; 1973). There is no requirement for an exact flux balance between the solar heating and the surface cooling of the oceans. There are characteristic, quasi-periodic short and long term oscillations in ocean surface temperature with periods near 3 to 7 years and in the 15 to 25 year and 60 to 70 year ranges that have significant impacts on the earth's climate. Short term oscillations include the ENSO and the IOD. Longer term oscillations include the PDO and the AMO. These provide a natural noise floor for climate temperatures. Changes in land use related to agriculture and the growth of urban areas have also changed local climates. These effects include irrigation and urban heat islands.

A convenient description of the earth's climate is the Köppen or similar zonal classification scheme which starts with five basic climate types that are further subdivided into zones based on precipitation and temperature. Such a classification using 31 zones updated from Kottek et al, (2006) is shown in Fig. 50, NOAA (2023).

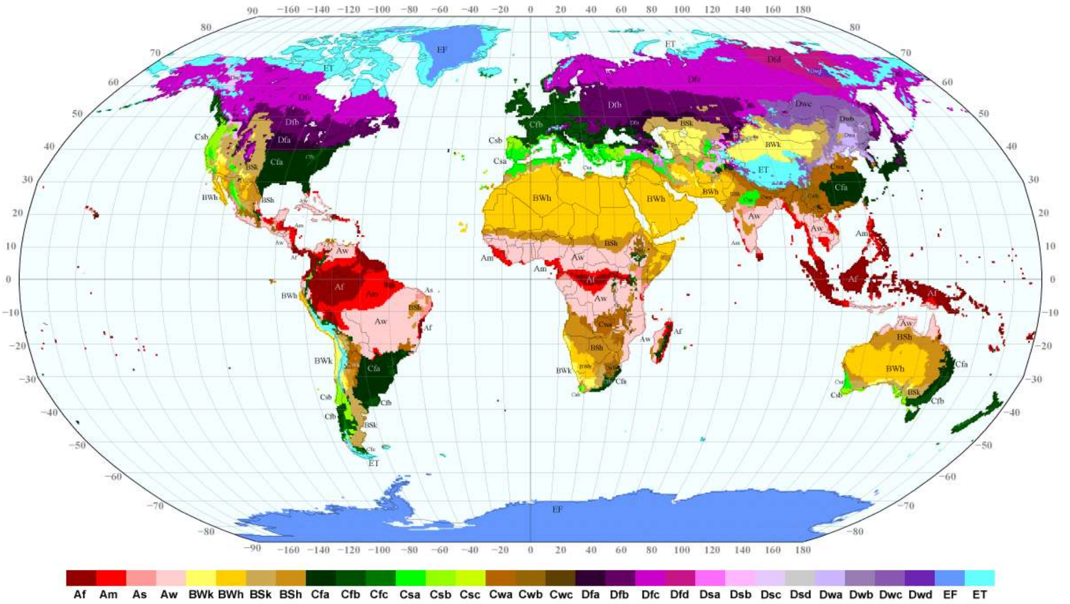

Figure 50: A world map of the Koppen-Geiger climate classification

Our understanding of climate change over different time scales is relatively recent. The first evidence for major climate change was the discovery of an Ice Age by Agassiz (1840) through observations of the glaciers in the Alps. The evidence for the Milankovitch cycles was established using deep drilled ocean sediment cores by Hays et al (1976). A more detailed history is provided by Imbrie and Imbrie (1979). The influence of ocean oscillations and ocean gyre circulation on climate was not established until the 1980s, Folland et al (1986). Any discussion of climate change requires careful consideration of all of the factors that influence temperature and precipitation over different time scales within a framework of climate zones. Climate is often defined quite narrowly as the long term trend in weather patterns. An averaging period of 30 years, updated at 10 year intervals, is commonly used. However, short term climate changes such as those related to ocean oscillations cannot be explained using 30-year averages.

5.1 The Transition from Weather to Climate

The quasi-periodic ocean oscillations provide a natural noise floor for climate studies. As weather systems that form over the oceans move over land, information about the ocean surface temperatures including seasonal phase shifts and ocean oscillations is coupled to the land based weather station data through changes to the convection transition temperature. The time scales associated with these oscillations therefore have to be included in climate analysis. The ocean gyre circulation and the main ocean oscillations are shown in Fig. 51 (Clark and Rörsch, 2023).

The ENSO and IOD vary over time scales in the 3 to 7 year range. While the temperature changes are relatively small, the related changes in evaporation and rainfall patterns are large because of the high tropical ocean temperatures. In addition, the maximum ocean surface temperature stays near 30 °C. It is the size and location of the Pacific equatorial warm pool that varies during the ENSO oscillations. The changes in area of the equatorial Pacific Ocean warm pool are illustrated in Figs. 52a and 52c for the ENSO peak in November 2015 and the minimum in December 2017, NRL (2021). The monthly ENSO index from 1979 to 2019 and the UAH global lower tropospheric (tlt) temperature anomalies are shown in Fig. 52b, UAH (2022). The lower troposphere temperatures follow the ENSO with a delay of several months.

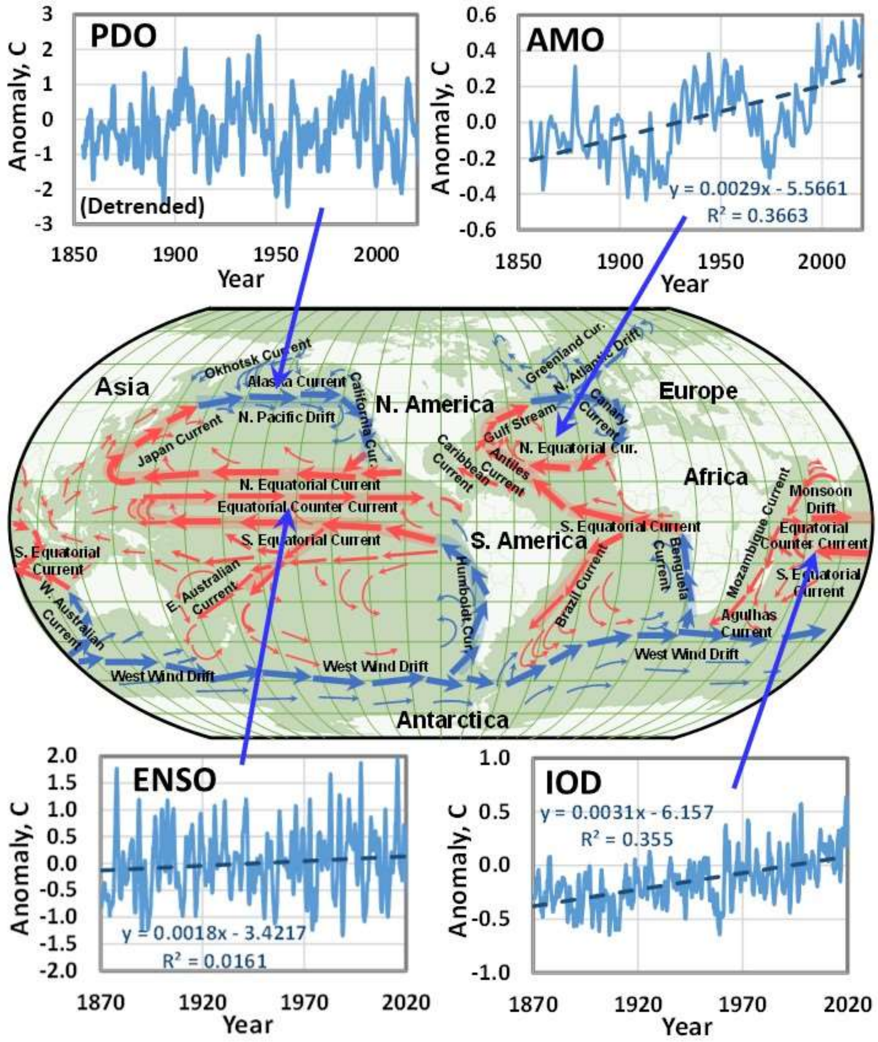

Figure 51: *The ocean gyre circulation and the four main ocean oscillations (schematic).*

The immediate cause of the ENSO is a change in the energy balance at the ocean surface between the solar heating and wind driven evaporation produced by a change in wind speed. However, the changes in ocean temperature are not limited to the surface and may reach 50 to 100 m in depth. There is a well-established inverse relationship between the Southern Oscillation Index (SOI) and the ENSO. The SOI is a measure of the wind speed derived from the surface pressure difference between Tahiti and Darwin, Australia, SOI (2022). As shown above in Fig. 29, the sensitivity of the latent heat flux to the wind speed within the ±30° latitude bands is near 15 W m^{-2}/m s^{-1}. As the wind speed decreases, the latent heat flux decreases and the ocean water warms. In addition, the ENSO region is part of the Pacific equatorial current. As the wind speed decreases, the ocean current velocity also decreases. This increases the transit time across the Pacific Ocean so more solar heat is absorbed by a cell of ocean water as it moves with the equatorial current. The ESNO index and the SOI, scaled and inverted to match the ENSO are shown in Fig. 53. The 2016 ENSO peak was produced by a decrease in wind speed near 2 m s^{-1}. The decrease in latent heat flux was approximately 30 W m^{-2} and the temperature change was 2.5 °C to a depth of at least 75 m. The change in ocean heat content to 75 m depth was approximately 800 MJ m^{-2}. Over the 6 month period of the ENSO peak, the cumulative increase in downward LWIR flux from CO_2 was 0.26 MJ m^{-2}. This is approximately 3000 times less than the change in heat content to 75 m depth produced by the ENSO peak, Clark and Rörsch, (2023). The detailed interactions that produce the ENSO oscillations are complex and include changes to the Walker circulation, Madden-Julian Oscillations and Rossby Waves, Schwendike et al (2021). Changes to the Walker circulation in the Pacific Ocean may also impact the Hadley/Walker circulation in the Atlantic and Indian Oceans.

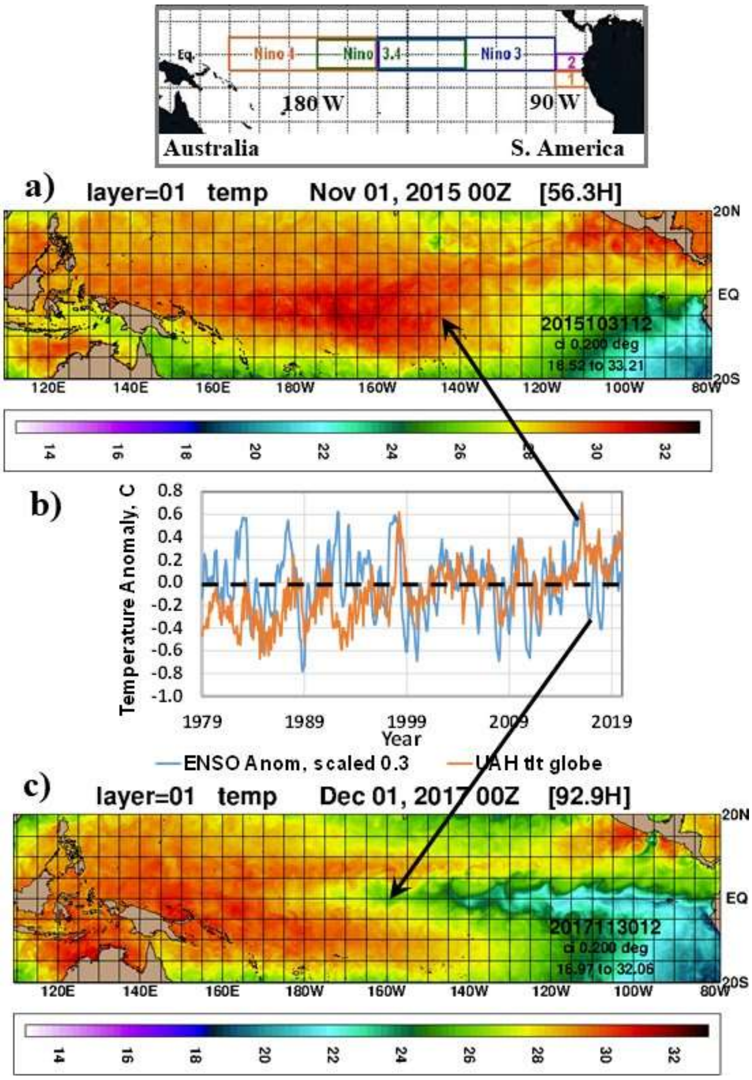

Figure 52: Surface temperatures in the equatorial Pacific Ocean for November 1, 2015 and December 1, 2017 corresponding to a) high and c) low values of the ENSO index. The map inset indicates the Nino 3.4 region used to determine the ENSO index. The monthly ENSO index (scaled) and the UAH global lower tropospheric temperature anomaly (tlt) from satellite microwave measurements are shown in b).

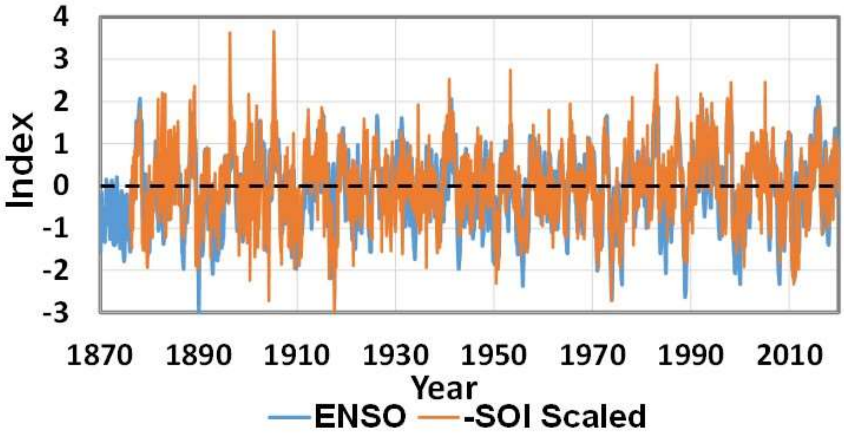

Figure 53: *Monthly ENSO data series from 1870 plotted with the scaled SOI index from 1876. The SOI is multiplied by 0.086 and the sign is reversed to match the ENSO response.*

The AMO and the PDO vary over longer time scales in the 60 to 70 year range (AMO, 2022; PDO, 2022). The AMO is discussed above in Section 4.5. The 1940 AMO peak is a prominent feature in the global mean temperature record that has been ignored in climate modeling studies (see Figures 14, 17e, 39 and 41). The PDO signal can be found in the weather station records for California and the AMO signal can be found in the UK weather station records. This is discussed in more detail by Clark and Rörsch (2023). The effect of wind speed on the ocean gyre circulation at high latitudes is the opposite of that near the equator. As the wind speed increases, the transit time decreases. There is less time for the ocean water to cool. An increase in wind speed therefore produces a warming or more accurately, a decrease in the rate of cooling along the polar leg of the N. Atlantic and N. Pacific Gyres. Most of this cooling occurs in winter as wind speeds increase and Arctic temperatures decrease (see Fig. 25). The influence of changes in solar activity on winter cooling has been discussed by Vinos (2022) as the winter gatekeeper hypothesis.

5.2 Climate Numbers and Number Series

Starting with H81, the 1-D RC model with a slab ocean was tuned to generate a time series of temperatures that approximately matched the number series obtained by averaging the weather station data. This is illustrated above in Fig. 10f. This process was later extended to the larger climate GCMs and used in all of the IPCC Climate Assessment Reports as illustrated in Figs. 13 and 14, Ramaswamy et al (2019). The weather station averages are now called global mean temperatures or temperature anomalies. These are just number series. This averaging process has been discussed in detail by Essex et al (2007). Temperature is a measure of the thermal motion of the molecules in a thermal reservoir. In thermodynamic terms it is an intensive property of the system. The corresponding extensive property is the heat content or enthalpy of the system. The average temperature of two independent systems, such as the temperatures recorded at weather stations in New York and Los Angeles, has no physical meaning. The first step in the averaging process, the sum of the temperatures is not a temperature, it is simply a number. When the sum of the temperatures is divided by the number of data points, the average is still just a number. When the mean is subtracted to create a global mean temperature anomaly, this is still just a number.

> *an average of temperature data sampled from a non-equilibrium field is not a temperature. Moreover, it hardly needs stating that the Earth does not have just one temperature. It is not in global thermodynamic equilibrium — neither within itself nor with its surroundings. It is not even approximately so for the climatological questions asked of the temperature field. Even when viewed from space at such a distance that the Earth appears as a point source, the radiation from it deviates from a black body distribution and so has no one temperature. There is also no unique "temperature at the top of the atmosphere". The temperature field of the Earth as a whole is not thermodynamically representable by a single temperature.*
>
> Essex et al, page 2, 2007

The global mean temperature anomaly is an area weighted average of the temperature anomalies derived from individual weather station measurements that have already been adjusted (homogenized). The data points used to generate the global mean are not usually displayed and there is no discussion of the variance of the anomalies. The individual data points used to generate the global anomaly are shown in Fig. 54, adapted from Lindzen, (2024).

Similarly, a simple conservation of energy argument is used to determine a planetary average LWIR cooling flux near 239 W m^{-2} emitted at TOA. This is then converted to an effective emission temperature near 255 K using the Stefan Boltzmann Law, Möller (1964). Neither the intensity variation of the LWIR flux nor the spectral distribution are considered. Fig. 55a shows an IR image of the earth recorded March 18, 2011, using the CERES instrument on the NASA aqua satellite, CERES (2011). The intensity of the LWIR emission varies from approximately 150 to 350 W m^{-2}. The low intensity white areas near the center of the image are the LWIR emission from cloud tops. Climate stability only requires an approximate long term planetary energy balance between the absorbed solar flux and the outgoing longwave radiation (OLR). There is no exact local energy balance. Almost all of any imbalance is accounted for by changes in ocean thermal storage. Fig. 55b shows the spectral distribution of the LWIR flux at TOA for three locations recorded using the Michelson interferometer (FTIR spectrometer) on the Nimbus 4 satellite. These demonstrate that the LWIR flux emitted at TOA does not have the spectral distribution of a blackbody radiator near 255 K, data from Hanel et al (1971). These spectra were available 10 years before the publication H81.

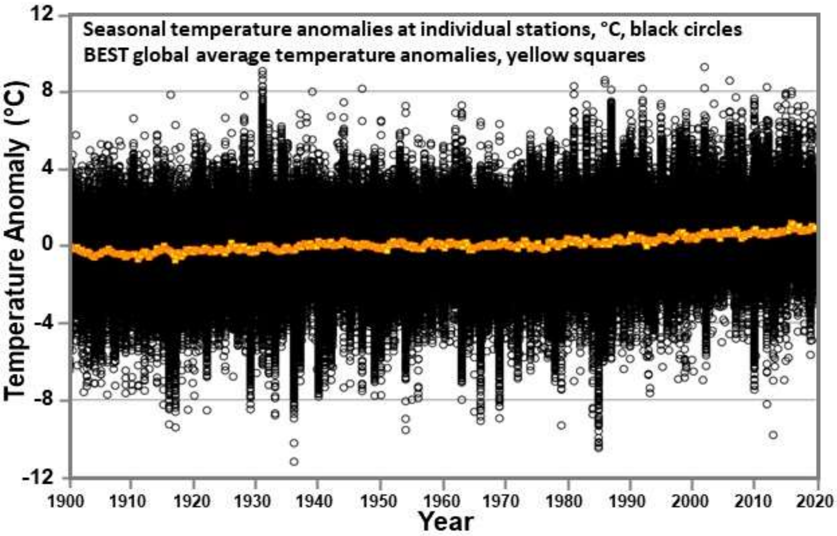

Figure 54: The seasonal temperature anomalies of the individual weather stations used to generate the BEST global average temperature anomalies. (BEST breakpoint adjusted data, minimum 100 years per station, ~ 3000 stations).

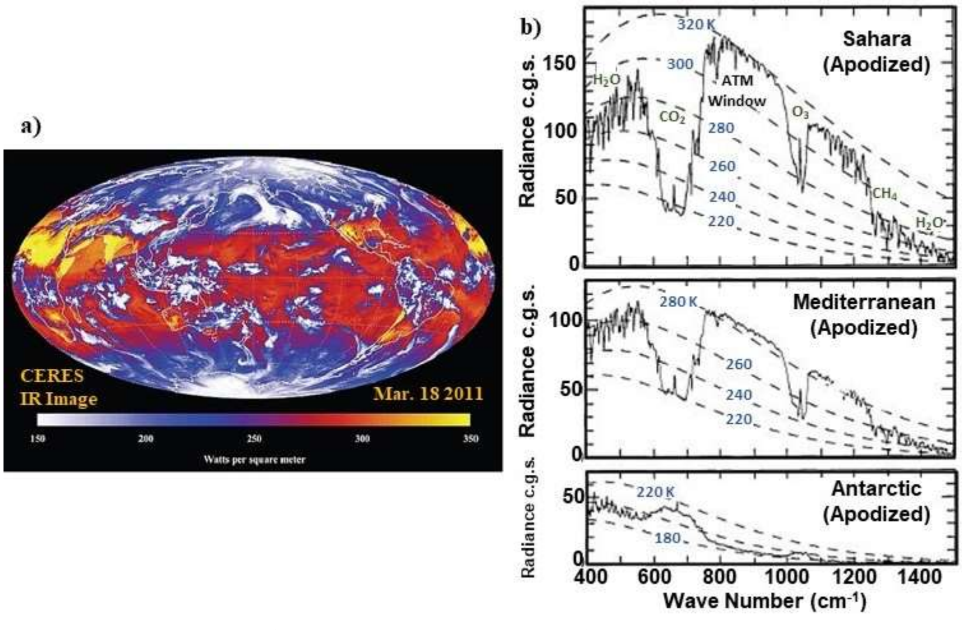

Figure 55: *a) CERES image of the LWIR emission to space from the earth, recorded March 18, 2011. b) The LWIR flux emitted at the top of the atmosphere (TOA) for selected geographic regions measured by the Michelson interferometer (FTIR spectrometer) on the Nimbus 4 satellite. A set of refence blackbody emission curves is included with the LWIR emission plots. The spectral distributions are clearly not that of a blackbody radiator at a temperature near 255 K.*

It is assumed that the fictitious effective emission temperature of 255 K would be the average temperature of a hypothetical earth without a ‘greenhouse effect’. This is compared to an equally fictitious average global temperature of 288 K. The temperature difference of 33 K is then called the greenhouse effect temperature. It is assumed that the 33 K temperature increase is produced by greenhouse gas absorption and emission in the atmosphere. This is based on the equilibrium climate assumption that a global average surface temperature is determined by the solar and LWIR flux balance.

Instead of defining the greenhouse effect, G, as a temperature difference, Ramanathan and coworkers used the difference in LWIR flux between the blackbody radiation emitted by the surface, E, and the outgoing longwave radiation (OLR) emitted at TOA, F, at the same location (Raval and Ramanathan, 1989, RR89; Ramanathan and Collins,1991).

$$G = E - F \tag{6}$$

To minimize the changes in E related to the diurnal cycle, they only considered ocean temperatures. Using ERBE satellite and ocean surface temperature data they found a global average for G of 179 W m^{-2}. This was based on a surface emission, E of 421 W m^{-2} and an OLR of 242 W m^{-2}. They further divided G into a greenhouse gas ‘trapping’ of 146 W m^{-2} and a cloud ‘trapping’ of 33 W m^{-2}. The increase in G with temperature was approximately linear from 273 to 295 K with a rate of 3.3 W m^{-2} K^{-1}. They assumed that G was the result of an ‘effective absorption’ along the vertical path between the surface and TOA. This oversimplifies the atmospheric energy transfer processes that determine the upward LWIR flux. In order to understand the simplifications introduced by Ramanathan and coworkers it is necessary to consider atmospheric energy transfer in more detail.

Three atmospheric profiles will now be considered based on MODTRAN calculations:

1. Surface and surface air temperatures of 300 K, tropical atmosphere model, clear sky.
2. Surface and surface air temperatures of 280 K, mid latitude summer atmosphere model, clear sky.
3. Surface and surface air temperatures of 300 K, tropical atmosphere model, altostratus cloud layer, 2.6 km base, 3 km top.

The spectral range is from 0 to 2200 cm^{-1} with a resolution of 2 cm^{-1}. The molecular line structure is not resolved, MODTRAN (2024). The CO_2 concentration is 420 ppm and the default water vapor profiles (water vapor scale =1) are used, adjusted for temperature offset using fixed relative humidity. The temperature, pressure, and water vapor concentration profiles at 300 and 280 K are shown in Figs. 56a, 56b and 56c.

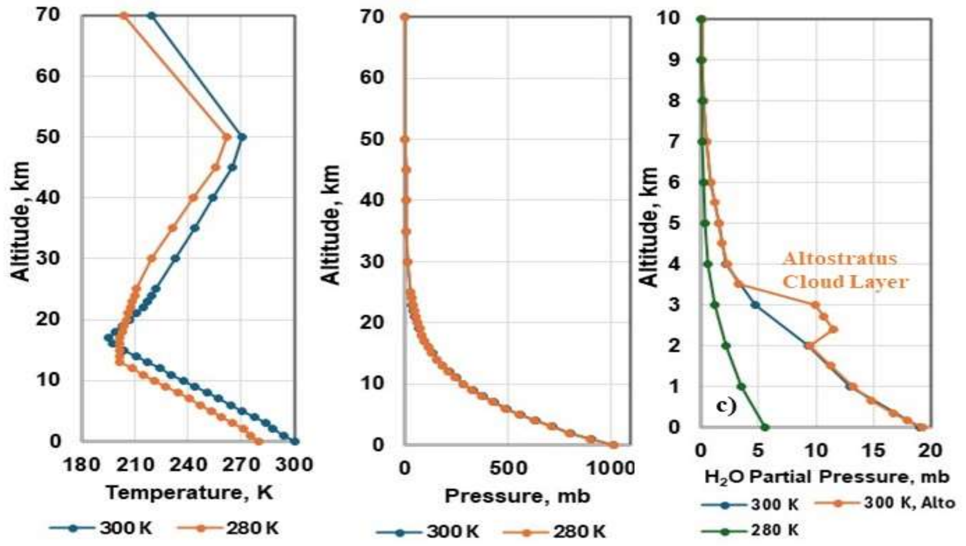

Figure 56: *a) temperature, b) pressure and c) water vapor pressure vs. altitude for the three atmospheric profiles used in the MODTRAN analysis.*

The data are from the MODTRAN output files. These examples are intended to illustrate the changes in the spectral distribution of the upward and downward LWIR flux with altitude. They are ‘snapshots’ of the atmospheric LWIR flux profile for the conditions specified. Both the temperature and the humidity profiles can change significantly during the diurnal cycle, especially near the surface (see Figs. 33 and 34). Radiative transfer calculations at higher spectral and spatial resolutions or with different water vapor profiles will give different quantitative results.

The spectral distribution of the total upward LWIR flux and the separate upward surface and atmospheric fluxes at selected altitudes through the atmosphere are shown in Fig. 57.

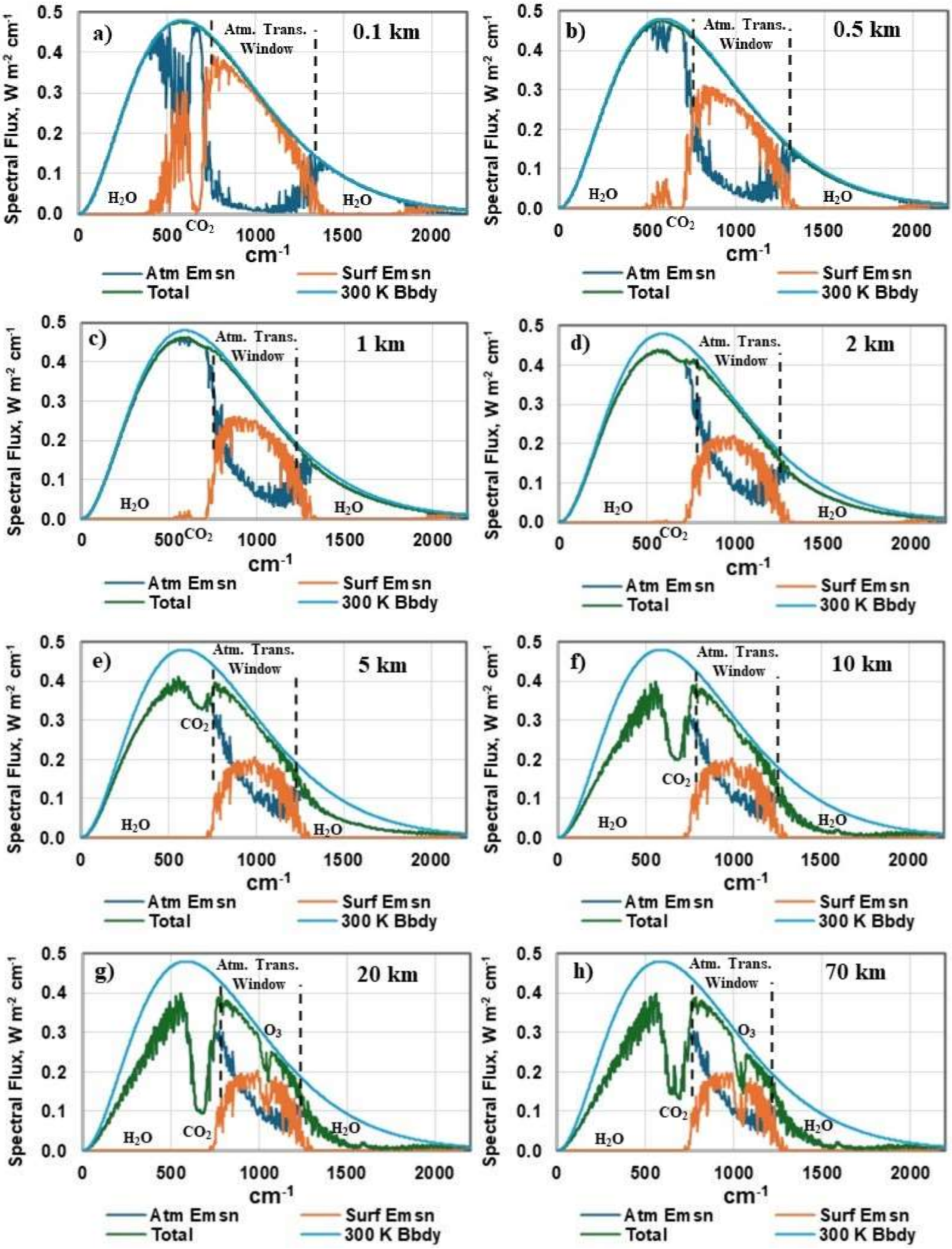

Figure 57: *The spectral distribution of the total upward LWIR flux and the separate upward surface and atmospheric fluxes at selected altitudes through the atmosphere. The main* H_2O *and* CO_2 *absorption-emission bands, the atmospheric transmission window and the stratospheric ozone absorption-emission are indicated. MODTRAN calculations, atmospheric profile 1, tropical model atmosphere, 300 K surface temperature, 0 to 2200 cm*$^{-1}$ *at 2 cm*$^{-1}$ *resolution (MODTRAN, 2024).*

The spectral distributions of the total upward and downward fluxes at selected altitudes are shown in Fig. 58. These are for atmospheric profile 1. Fig. 57a shows the upward LWIR flux terms at 100 meters (0.1 km) above the surface. Below 400 cm^{-1} and between 1400 and 1800 cm^{-1}, all of the upward LWIR flux emitted by the surface has already been absorbed by water vapor (orange line). In addition, the CO_2 band has absorbed at least 95% of the surface flux between 650 and 690 cm^{-1}. However, almost all the absorbed surface flux has been replaced by upward LWIR flux emitted from within the first 100 m air layer. The intensity of the total upward flux at 100 m is close to that of the surface emission. There is also a similar downward LWIR flux that is emitted from this layer to the surface. This process of absorption and emission continues through the troposphere. The total upward flux decreases with altitude. At 2 km, as shown in Fig. 57d, almost all of the surface flux below 700 cm^{-1} and between 1300 and 2200 cm^{-1} has been absorbed and replaced by atmospheric emission. Part of the upward atmospheric LWIR flux from below is also absorbed and replaced by local atmospheric LWIR emission at a lower temperature. Above 2 km, the change in the surface flux through the LWIR transmission window is small. As the temperature and water vapor pressure decrease with altitude, the absorption decreases and there is a gradual transition from absorption-emission to a free photon flux. There is little change in the water band emission above 10 km. The upward LWIR flux emitted by CO_2 continues to decrease up to an altitude of approximately 20 km. In the stratosphere, there is also an ozone absorption-emission feature near 1050 cm^{-1}.

Fig. 58a shows the upward surface emission, E, and the downward LWIR flux to the surface. These interact to establish the LWIR exchange energy (see Section 4.2 and Fig. 23). Within the spectral regions below 400 cm^{-1} and between 1400 and 1800 cm^{-1}, the downward LWIR flux is emitted from within the first 100 m layer above the surface. As the temperature and water vapor concentration decrease with increasing altitude, the downward LWIR flux decreases and the spectral profile changes. Because of increased molecular line broadening in the lower troposphere, almost all of the downward LWIR flux that reaches the surface originates from within the first 2 km layer above the surface (see Fig. 19).

When the surface temperature decreases, both the upward LWIR flux emitted by the surface and the atmospheric absorption-emission decrease. However, the net LWIR surface flux emitted into the LWIR transmission window increases. This is illustrated in Fig.59 that compares atmospheric profiles 1 and 2. Figs. 59a and 59b show the upward flux emitted by the surface and the downward LWIR flux to the surface emitted from the lower troposphere for surface temperatures of 300 and 280 K. The LWIR transmission window flux increases from 81 to 105 W m^{-2}. Figs. 59c and 59d show the upward fluxes emitted at the 100 m (0.1 km) level.

At 300 K, the surface emission is 453.4 W m^{-2} in the 0 to 2200 cm^{-1} spectral region. The first 100 m layer absorbs 255.8 W m^{-2} of this flux. It is replaced by 253.4 W m^{-2} of upward atmospheric emission from the air layer. The total upward emission at 100 m is 451 W m^{-2}. The spectral distribution of the upward flux terms at 100 m is shown in Fig. 59c. At 280 K, the surface emission is 344.9 W m^{-2}. Of this, 156.3 W m^{-2} is absorbed and replaced by 154.2 W m^{-2} of upward emission from the air layer. The total upward emission at 100 m is 342.8 W m^{-2}. The spectral distribution of the upward flux at 100 m is shown in Fig. 59d.

The absorption-emission process continues as the altitude increases and the spectral distributions change. For the 300 K surface temperature at 20 km, the total upward emission is 298.8 W m^{-2}. The downward emission from above 20 km has decreased to 9.3 W m^{-2}. For the 280 K surface temperature at 20 km, the total upward emission is 250 W m^{-2} and the downward emission is 7.6 W m^{-2}. The spectral distributions are shown in Figs. 59e and 59f.

For the 300 K profile at 70 km, 386.1 W m^{-2} of the surface emission has been absorbed and replaced by a cumulative upward atmospheric emission of 232 W m^{-2}. The total upward flux is 299.3 W m^{-2}. For the 280 K profile at 70 km, 277.7 W m^{-2} of the surface emission has been absorbed and replaced by a cumulative upward atmospheric emission of 157 W m^{-2}. The total upward flux is 250.4 W m^{-2}. The fraction of the surface flux removed by the absorption emission process is the normalized greenhouse effect, g, as defined by RR89. In the examples considered here it is 0.34 for the 300 K atmospheric profile 1 and 0.27 for the 280 K atmospheric profile 2.

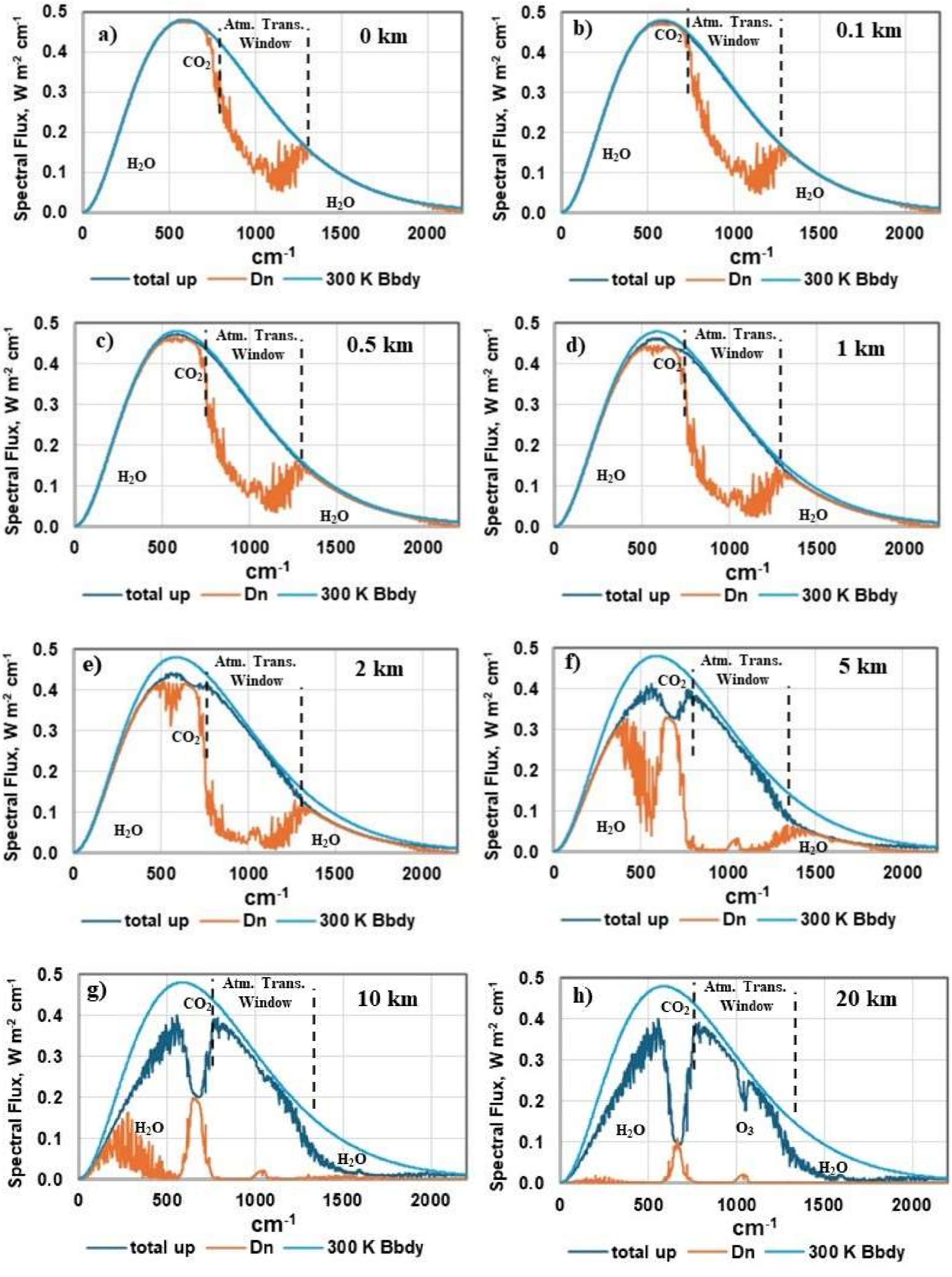

Figure 58: *The spectral distribution of the total upward and downward fluxes at selected altitudes. The main H_2O and CO_2 absorption-emission bands, the atmospheric LWIR transmission window and the stratospheric ozone absorption peak are indicated. MODTRAN calculations, atmospheric profile 1, tropical atmosphere, 300 K surface temperature, 0 to 2200 cm^{-1} at 2 cm^{-1} resolution (MODTRAN, 2024).*

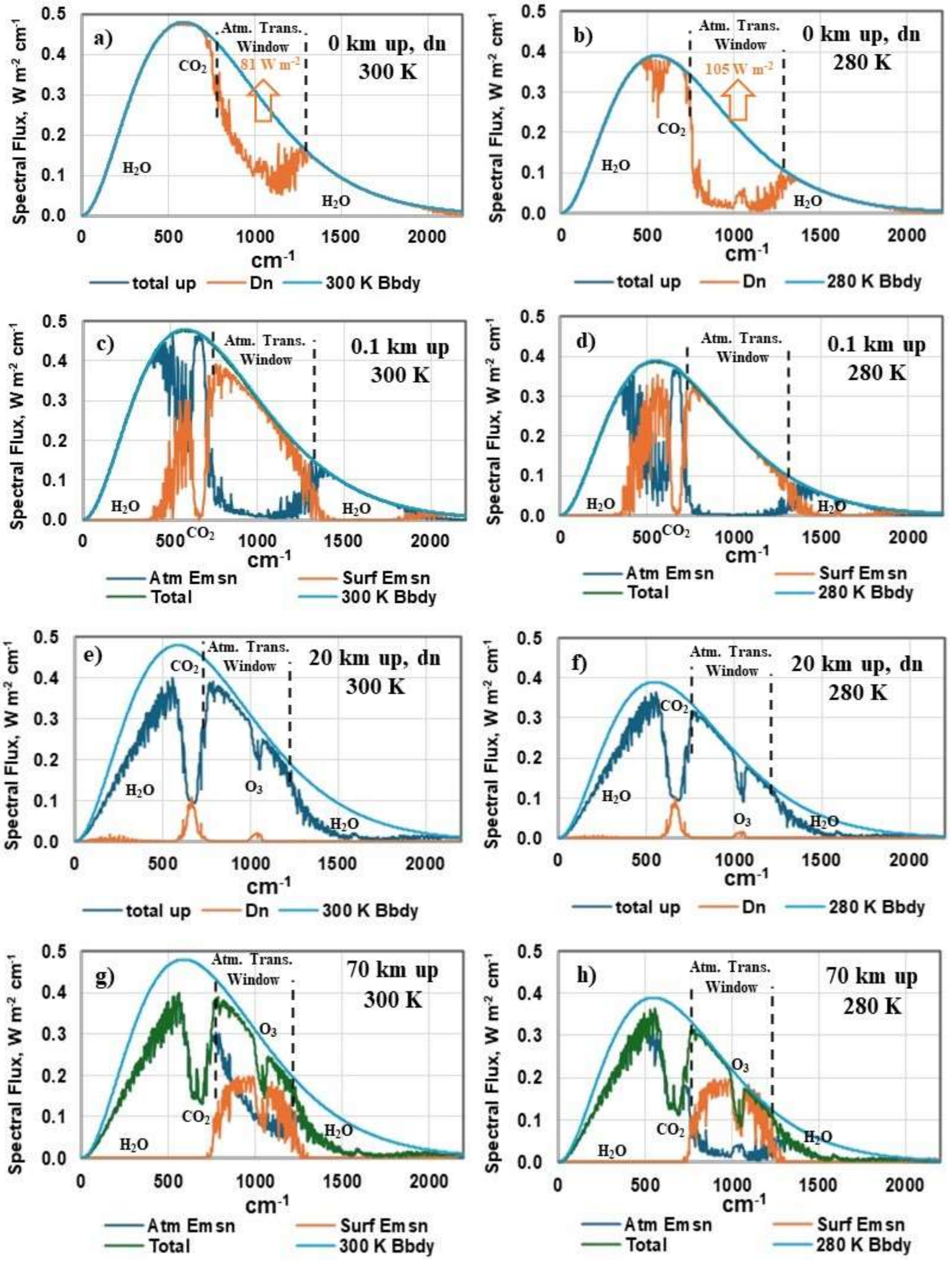

Figure 59: *Comparison of the atmospheric profiles 1 and 2 at 300 and 280 K for the upward and downward flux at the surface (a and b), the upward fluxes at 0.1 k (c and d), the upward and downward fluxes at 20 km (e and f) and the upward fluxes at 70 km (g and h). MODTRAN calculations, 300 K, 0 to 2200 cm^{-1}, 2 cm^{-1} resolution (MODTRAN, 2024).*

The total LWIR fluxes from 0 to 2200 cm^{-1} for the upward atmospheric, surface and total LWIR emission at selected altitudes for surface temperatures of 300 and 280 K are shown in Fig. 60a. The total upward and downward LWIR fluxes at selected altitudes are shown in Fig. 60b. The differences between the surface emission at 300 and 280 K and the total upward fluxes at selected altitudes are shown in Fig. 60c. This shows the change in G with increasing altitude. At 70 km, G_{300} = 151 W m^{-2} and G_{280} = 94.5 W m^{-2}, are the greenhouse effect fluxes as defined by RR89.

This is a mathematical construct that only considers the upward LWIR flux. Such an approach creates a net heat gain ('trapping') in the troposphere. However, when the downward flux is included, there is usually a net LWIR cooling at each level (see Fig. 21). This does not include NIR solar heating, latent heat release or local vertical motion of the air parcel.

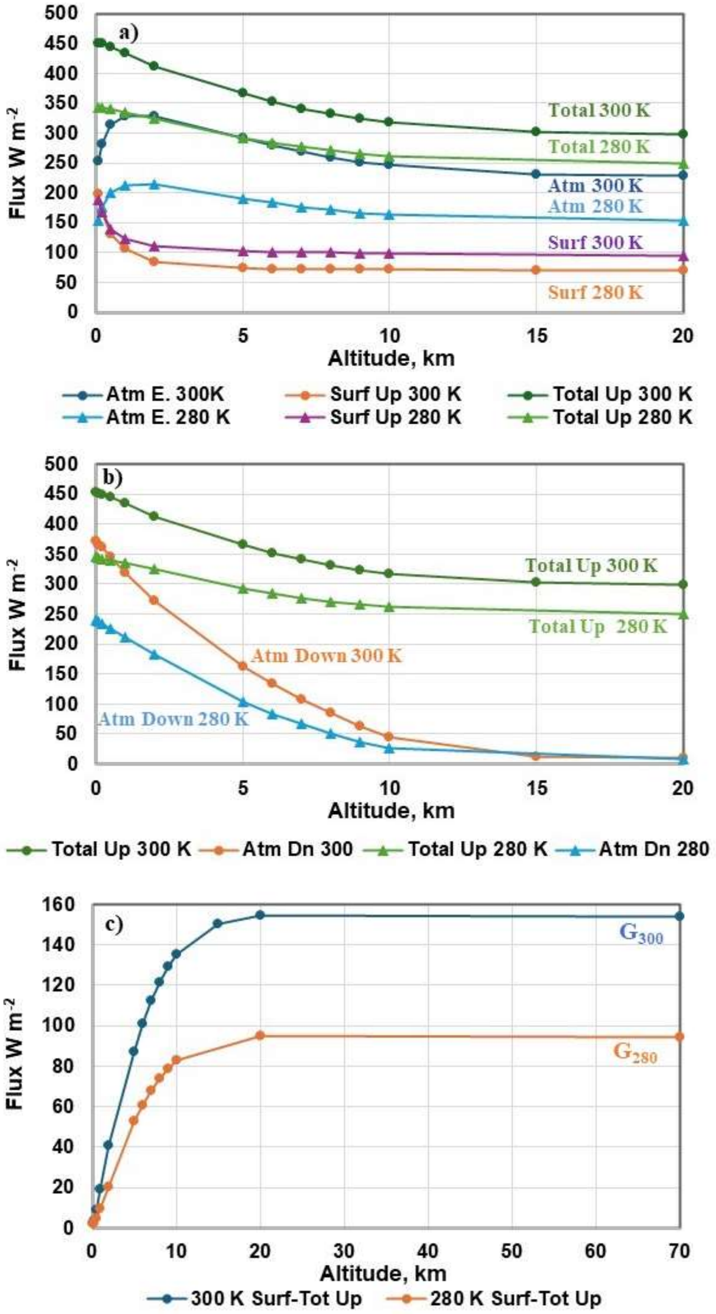

Figure 60: Comparison of atmospheric profiles 1 and 2. a) Upward LWIR atmospheric, surface and total fluxes at selected altitudes for surface temperatures of 300 and 280 K. b) Total upward and downward fluxes for selected altitudes and surface temperatures of 300 and 280 K. c) Difference between the surface flux and total upward flux for selected altitudes and surface temperatures of 300 and 280 K. The values at 70 km (TOA), G_{300} and G_{280} are the greenhouse fluxes defined by Raval and Ramanathan (1989).

Fig. 61a shows the spectral distributions of the surface emission, E, and the OLR, F, at 300 and 280 K. The surface emission increases by approximately 30% from 344.9 to 453.4 W m^{-2} as the temperature increases from 280 to 300 K. The contributions to the OLR at 300 and 280 K from the four spectral regions corresponding approximately to the H_2O and CO_2 bands and the transmission window are summarized in Fig. 61c. The main change in the OLR is the increase in emission through the atmospheric transmission window. The OLR related to water band emission below 500 cm^{-1} and above 1500 cm^{-1} is insensitive to the surface temperature, Koll and Cronin, (2018). As the temperature increases from 280 to 300 K, the water band emission to space shifts to a higher altitude, Clark (2013a). This is because the emission is determined by the local water vapor concentration. Above the saturation level, this in turn is determined by the local air temperature. There is a broad emission band with a peak near 260 K (13 °C). In this MODTRAN example, the 260 K level increases in altitude from 4 to 6.5 km as the surface temperature increases from 280 to 300 K.

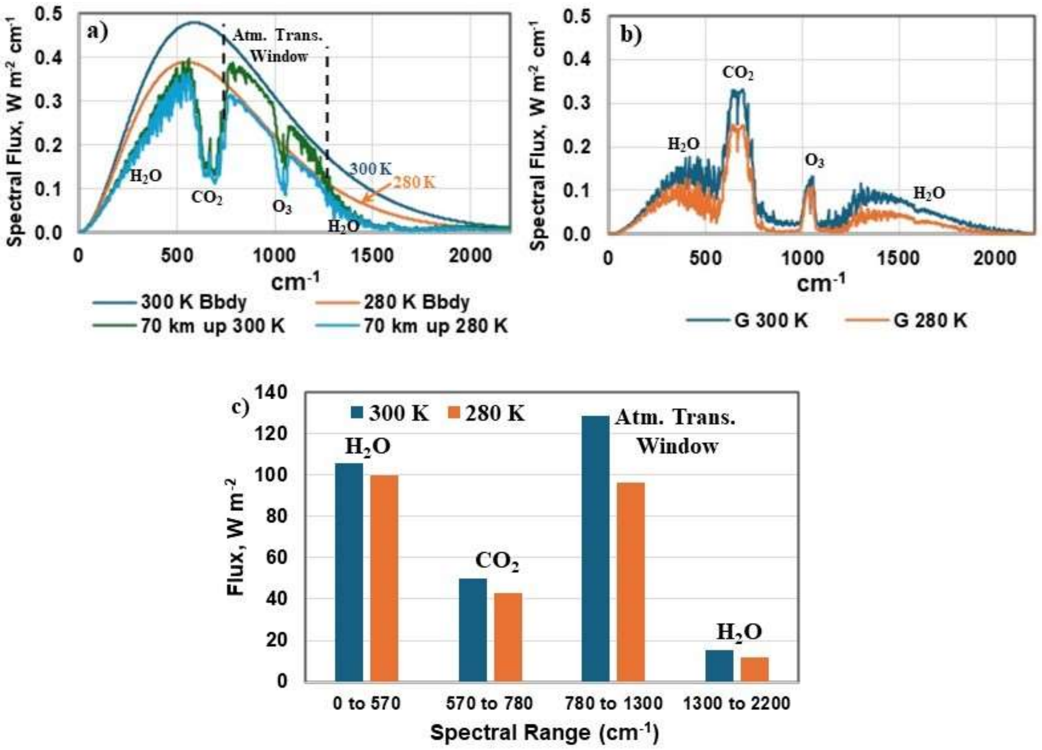

Figure 61: a) Spectral profiles of the surface and OLR emission at 300 and 280 K, b) spectral profiles of the greenhouse fluxes (surface-OLR) as defined in RR89 and c) approximate contributions of the H_2O and CO_2 bands and the transmission window to the OLR flux for the spectral regions indicated.

The spectral profiles of the greenhouse fluxes, G_{300} and G_{280}, are shown in Fig. 61b. Here, the OLR spectra shown in Fig. 61a have been subtracted from surface emission. There is an increase in absorbed flux as the temperature increases. However, it is the downward LWIR flux to the surface that determines the surface exchange energy (see Section 4.2). Most of this downward flux is emitted by the air layer close to the surface (see Fig. 19). The greenhouse effect, G, as defined in RR89 is not a useful measure of the atmospheric energy transfer processes that determine the surface temperature.

So far, this analysis has only considered clear sky conditions. A cloud layer contains water droplets or ice crystals that are good blackbody absorbers and emitters in the LWIR spectral region. Such a layer absorbs all of the upward LWIR flux from below and emits blackbody radiation downward at the cloud base temperature. It also absorbs all of the downward LWIR flux from above and emits blackbody radiation upwards at the cloud top temperature. RR89 only considered the change in the upward LWIR flux. On average, clouds reduced the OLR by approximately 30 W m^{-2}. This was called a 'cloud trapping'. The increase in downward LWIR flux to the surface through the atmospheric LWIR transmission window was ignored. Fig. 62 shows the effect adding a cloud layer on the flux terms shown in Fig. 60 for atmospheric profile 3, the MODRAN tropical atmosphere model with a 300 K surface temperature. In this illustration, the MODTRAN altostratus cloud option with a base at 2.6 km and a top at 3 km is used. Fig. 62a shows the effect of this cloud layer on the upward flux terms. The altostratus layer is indicated by the gray bar. The upward surface flux is absorbed and is zero above the cloud layer. This is indicated by the lower red circle. The upward flux emitted by the atmosphere is also absorbed, but is replaced by blackbody emission at the cloud top temperature of 284 K. This is indicated by the upper red circle. Above the cloud layer the atmospheric emission and total emission have the same values. Fig. 62b shows the effect of the altostratus layer on the total upward and downward flux terms. The total upward flux terms are the same as in Fig. 62a. The downward flux is absorbed by the cloud layer and replaced by downward LWIR emission from the cloud base at a temperature of 286.4 K. In this MODTRAN example, the downward LWIR flux to the surface increases from 372 to 434 W m^{-2}, and the net LWIR emission into the LWIR transmission window decreases from 81 to 19.5 W m^{-2}. The increase in downward flux from the cloud base may also mask at least part of any increase in downward flux produced by an increase in atmospheric CO_2 concentration. Clouds may therefore change any possible water vapor feedback effects. Over the oceans, sea mist and water spray from breaking waves also contribute to the LWIR flux.

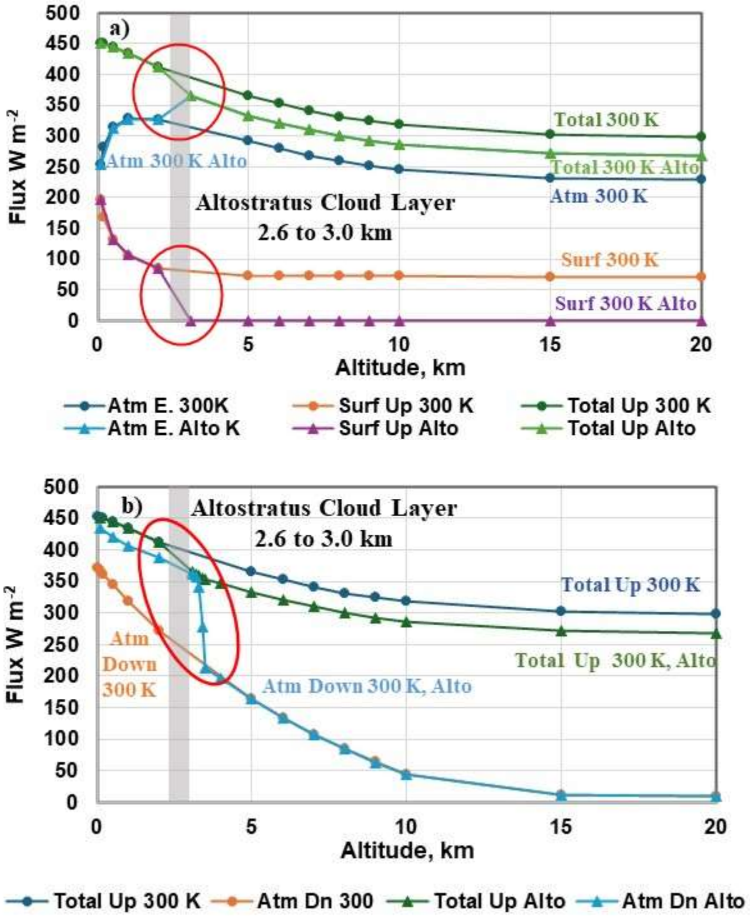

Figure 62: Atmospheric profile 3, the effect of a cloud layer on a) the upward flux terms and b) the total upward and downward flux terms. The cloud absorbs the upward and downward incident fluxes and replaces them with blackbody emission at the cloud base and cloud top temperatures.

The discussion of a greenhouse effect based on the temperature difference between an average surface temperature and an effective emission temperature at TOA (Hansen et al, 1981) or in terms of the related flux difference between the local surface emission and the OLR (Raval and Ramanathan, 1989) does not include all of the interactive energy transfer processes that determine the surface temperature. Radiative transfer through the atmosphere involves the absorption and emission of both the upward and downward LWIR fluxes by the local air parcel. In addition, the role of water in the energy transfer has been underestimated. The water related processes include ocean solar absorption, evaporation, the release of latent during cloud formation, solar attenuation by clouds, upward and downward LWIR emission by clouds and NIR solar absorption by the water vapor overtone bands. Further details are given above in Section 4 and by Clark and Rörsch (2023).

In addition to global averages of the earth's temperature field, highly detailed satellite radiometer data are often averaged to give three climate numbers, an average absorbed solar flux, an average reflected flux or albedo and the average outgoing LWIR flux. The integrated and averaged flux terms are adjusted to give the desired imbalance required by the radiative forcings used in the climate models. Fig. 63 shows the zonal averages of the net flux (absorbed solar flux minus LWIR flux) for March, June, September and December, adapted from Kandel and Voilier, (2010). Near equinox, in March and September, the net flux within the ±30° latitude bands is positive with a net energy flow into the earth of up to 100 W m^{-2}. There is net cooling at higher latitudes. In June, near summer solstice in the N. Hemisphere, the heating occurs in the N. Hemisphere and this reverses in December for the S. Hemisphere summer. The starting point for any realistic analysis of these flux terms is that the earth consists of two weakly coupled hemispheres with heating and cooling cycles that are out of phase with each other. There is no requirement for an exact flux balance. The dominant term in any imbalance is a change in ocean thermal storage.

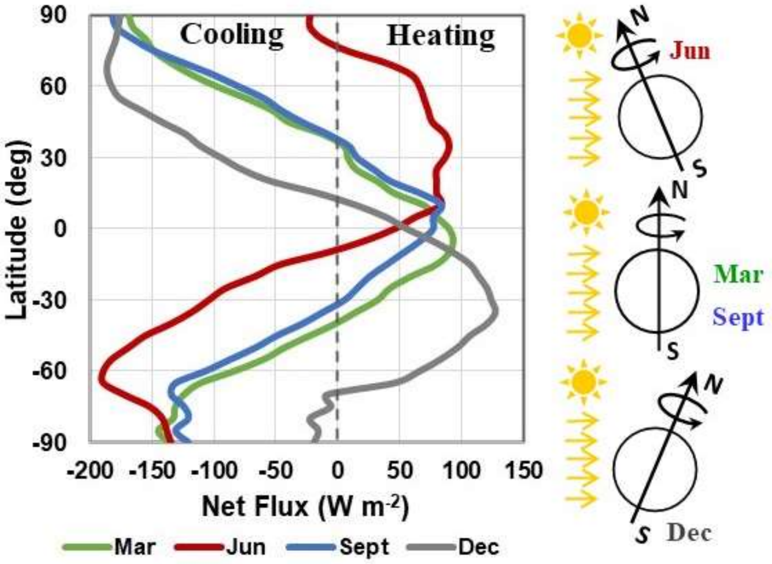

Figure 63: Zonal averages of the net flux (absorbed solar minus emitted LWIR flux), for March, June, September and December, five-year average CERES values.

Conclusions

Starting in the nineteenth century, the energy transfer processes that determine the surface temperature were oversimplified using the equilibrium climate assumption. The time dependent flux terms were replaced by average values. Physical reality was abandoned in favor of mathematical simplicity. When the atmospheric CO_2 concentration is increased, radiative transfer calculations show that there is a small decrease in the LWIR flux returned to space within the spectral emission bands of CO_2. It is assumed that this perturbs the equilibrium climate and that the surface temperature increases until the flux balance is restored. This approach was used by Arrhenius in 1896. It created surface warming as a mathematical simplification in his calculations. The idea that an increase in the atmospheric CO_2 concentration could warm the earth became accepted scientific dogma. The concept was originally proposed as the cause of an Ice Age. Gradually this was transformed to concern over warming effects from fossil fuel combustion.

In 1967, Manabe and Wetherald used the Arrhenius model as the foundation for their 1-D RC model. They added a 9 or 18 layer radiative transfer calculation with a fixed relative humidity

(RH) distribution. This added a water vapor feedback that amplified the initial CO_2 warming created by the equilibrium assumption. When the CO_2 concentration was increased from 300 to 600 ppm in the MW67 model, the total warming was 2.9 °C for clear sky conditions. They went on to incorporate their MW67 modeling assumptions into every unit cell of the 'highly simplified' GCM described in MW75. This provided an invalid benchmark for the warming created in later GCMs. Manabe's group never considered the errors associated with the equilibrium assumption and ignored the daily and seasonal variations in both temperature and RH found in the surface boundary layer. For a CO_2 doubling, the small temperature increases calculated at each step in their time integration procedure does not accumulate in the real atmosphere.

As funding was reduced at NASA after the end of the Apollo (moon landing) program, the group modeling planetary atmospheres shifted to climate studies. In H76 they simply copied the MW67 model and used it to create warming artifacts for 10 minor species including CH_4 and N_2O. The basic equilibrium climate model was completed with H81. This added a slab ocean to MW67 and introduced the CO_2 step doubling. The model was then tuned so that the calculated warming resembled the global mean temperature record derived from the measured temperature record. This established the pseudoscientific concepts of radiative forcing, feedbacks and climate sensitivity that have been used by the IPCC since it was established in 1988.

As computer technology improved, the climate models became more complex. Coupled atmosphere-ocean GCMs replaced the 1-D RC model, but the underlying equilibrium assumption was still there. Water vapor feedback still amplified the CO_2 warming artifact created by Arrhenius. Starting with the Third IPCC Climate Assessment Report (TAR), 2001, the time series of radiative forcings used to simulate the global mean temperature record was split into 'natural' and 'anthropogenic' forcings. The climate models were then rerun to create a separate 'natural baseline' and an 'anthropogenic contribution'. A vague statistical argument using changes to the normal distribution ('bell' or Gaussian curve) of temperature was then used to claim that the increase in temperature caused by 'anthropogenic' forcings would cause an increase in the frequency and intensity of 'extreme weather events'. This provided the pseudoscientific justification for the political control of fossil fuel combustion that has led to the 1.5 or 2 °C limit in the Paris Climate Accord and the disastrous net zero policy of today.

The scientific method is an interactive process of hypothesis based on available scientific evidence. This was never used in mainstream climate science. The equilibrium climate assumption became accepted scientific dogma in the nineteenth century. Climate modeling has now degenerated past dogma into a quasi-religious cult. Irrational belief in climate model results has replaced logic and reason. Instead of changing the hypothesis to explain the data, the opposite has occurred. Climate data has been made to fit the pseudoscience of radiative forcing, feedbacks and climate sensitivity. The weather station data has been 'adjusted' using 'homogenization'. Satellite radiometer data has been reduced to the three numbers used to create the illusion of an equilibrium climate. The spectral distribution of the LWIR flux returned to space has been removed from the discussion of the effective emission temperature and the greenhouse effect temperature. The Charney Report ignored the Milankovitch cycles that are the real cause of the Ice Age cycle. The role of ocean oscillations in climate change has been neglected. The paleoclimate record has been distorted to fit the climate model results. Tree ring data was unilaterally selected to reduce the temperature increase related to the medieval warming period and create the well-known hockey stick plot used in the Third IPCC Climate Assessment Report. The contribution of fossil fuel combustion to the observed 140 ppm increase in CO_2 concentration has been greatly exaggerated. Electronic controls theory has been used incorrectly to describe climate feedback effects. However other concepts in electronics such as the phase shift and the signal to noise ratio have been conveniently overlooked.

The basic requirement of a climate model is that it should accurately predict the climate observations it was configured to simulate. When climate models are examined in more detail and model outputs are compared to observations, it is found that that they have very poor predictive capabilities. The limitations of the climate models associated with the CMIP3 and CMIP5 ensembles have been discussed in detail in *Climate Change Reconsidered II: Physical Science*, Idso et al

(2013). Since short term climate change is strongly influenced by ocean oscillations, this provides a good model test. Section 1.4.1 El Niño/Southern Oscillation concludes:

> *Clearly there remain multiple problems in the ability of models to reliably simulate various aspects of climate associated with ENSO events, casting further doubt on the overall ability of models to simulate the future climate of the planet in general.*

When the pseudoscience of radiative forcing, feedbacks and climate sensitivity is removed from the climate models, what is left? Are the underlying GCMs capable of predicting natural climate changes such as those related to ocean oscillations? Model performance so far indicates that another approach is needed.

The 2.9 °C clear sky increase in surface temperature produced by a doubling of the CO_2 concentration reported in Table 5 of MW67 was produced by two mathematical artifacts created using an oversimplified 1-D RC model. These errors were never corrected and provided the foundation for the massive climate modeling fraud we have today. The part of the 2021 Nobel Prize in Physics awarded to Manabe was for climate modeling simplifications or errors that created spurious warming when the atmospheric CO_2 concentration was increased.

Instead of an extended discussion over the magnitude of the climate sensitivity, there is a simple question that climate science should address:

At present the average annual increase in atmospheric CO_2 concentration is near 2.4 ppm per year. This produces an increase in the downward LWIR flux from the lower troposphere to the surface of approximately 0.034 W m^{-2} per year. How does this change the surface temperature of the earth?

The correct answer is that any temperature changes are too small to measure. Nor can there be any effect on extreme weather events.

Guest-Editor: Jan-Erik Solheim; Reviewers: anonymous.

Acknowledgements

This work was performed as independent research by the author. It was not supported by any grant awards and none of the work was conducted as a part of employment duties for any employer. The views expressed are those of the author.

The author also thanks the SCC editor, Herman Harde, for many helpful comments that have improved the manuscript.

References

Ackerman, T. P., 1979: *On the effect of CO_2 on the atmospheric heating rates*, Tellus v. 31, pp 115-123. https://a.tellusjournals.se/articles/10.3402/tellusa.v31i2.10416

Agassiz, L., 1840: *Etudes sur les Glaciers*, Neuchatel.

Akasofu, S.-I., 2010: *On the recovery from the Little Ice Age*, Natural Science, v. 2, no. 11, pp. 1211-1224. http://dx.doi.org/10.4236/ns.2010.211149

AMO, 2022: *Atlantic Multidecadal Oscillation*. https://www.esrl.noaa.gov/psd/data/correlation/amon.us.long.mean.data

Andrews, R., 2017a: *Adjusting Measurements to Match the Models – Part 3: Lower Troposphere Satellite Temperatures*, Energy Matters, Sept 14. http://euanmearns.com/adjusting-measurements-to-match-the-models-part-3-lower-troposphere-satellite-temperatures/#more-19464

Andrews, R., 2017b: *Making the Measurements Match the Models – Part 2: Sea Surface Temperatures*, Energy Matters, Aug 2. http://euanmearns.com/making-the-measurements-match-the-models-part-2-sea-surface-temperatures/

Andrews, R., 2017c: *Adjusting Measurements to Match the Models – Part 1: Surface Air*

Temperatures, Energy Matters, July 27. http://euanmearns.com/adjusting-measurements-to-match-the-models-part-1-surface-air-temperatures/

Argo Marine Atlas, 2021: https://argo.ucsd.edu/data/data-visualizations/marine-atlas/

Arrhenius, S., 1896: *On the influence of carbonic acid in the air upon the temperature of the ground*, The London, Edinburgh, and Dublin Philosophical Magazine and Journal of Science, v. 41, pp. 237-276. https://doi.org/10.1080/14786449608620846

Autio, P., 2020: *Siberia on fire – every summer*, Watts Up with That, July 14. https://wattsupwiththat.com/2020/07/14/siberia-on-fire-every-summer/

Beck, E-G., 2022: *Reconstruction of atmospheric CO_2 background levels since 1826 from direct measurements near ground*, Science of Climate Change, v. 2, no. 2, pp.148-211. https://scienceofclimatechange.org/ernst-georg-beck-reconstruction-of-atmospheric-co2-background-levels-since-1826-from-direct-measurements-near-ground-inclusive-supplements-3-5/

Berger, T. and G. Sherrington, 2022: *Uncertainty of Measurement of Routine Temperatures–Part Three*, Watt Up with That, Oct 14. https://wattsupwiththat.com/2022/10/14/uncertainty-of-measurement-of-routine-temperatures-part-iii/

Black, E., M. Blackburn, G. Harrison, B. Hoskins and J. Methven, 2004: *Factors contributing to the summer 2003 European heatwave*, Weather, v. 59, no. 8, pp. 217-223.https://doi.org/10.1256/wea.74.04

Böhm, F., A. Haase-Schramm, A. Eisenhauer, W.-C. Dullo, M. M. Joachimski, H. Lehnert and J. Reitner, 2002: Geochemistry, *Evidence for preindustrial variations in the marine surface water carbonate system from coralline sponges*, Geophysics, Geosystems v. 3, no. 3, 10.1029/2001GC000264, pp 1-13. https://doi.org/10.1029/2001GC000264

Bolin, B., 1960: *On the Exchange of Carbon Dioxide between the Atmosphere and the Sea*, Tellus, v. 12, pp. 274-281. https://doi.org/10.3402/tellusa.v12i3.9402

Bolin, B., and Eriksson, E., 1959: *Changes in the carbon dioxide content of the atmosphere and sea due to fossil fuel combustion*, in B. Bolin, (Ed.), *The atmosphere and the sea in motion,* pp. 130-142. New York: The Rockefeller Institute and Oxford University Press. http://climatepositions.com/wp-content/uploads/2014/03/n8._Bolin___Eriksson__1958corrected.pdf

Bryson, R. A. and G. J. Dittberner, 1976: *A non-equilibrium model of hemispheric mean surface temperature*, J. Atmos. Sci., v. 33, no. 11, pp. 2094-2106. https://journals.ametsoc.org/view/journals/atsc/33/11/1520-0469_1976_033_2094_anemoh_2_0_co_2.xml

Budyko, M. I., 1969: *The effect of solar radiation variations on the climate of the Earth*, Tellus, v. 21, no. 5, pp. 611-619. https://doi.org/10.3402/tellusa.v21i5.10109

Callendar, G. S., 1938: *The artificial production of carbon dioxide and its influence on temperature*, J. Roy. Met. Soc., v. 64, pp. 223-240. https://doi.org/10.1002/qj.49706427503 Available at: http://www.met.reading.ac.uk/~ed/callendar_1938.pdf

CERES Team, 2011: NASA Langley, Press Release, OLR Image, March 18. https://ceres.larc.nasa.gov/resources/images/#public-release-satellite-images

Cess, R. D. and S. D. Goldenberg, 1981: *The effect of ocean heat capacity upon global warming due to increasing atmospheric carbon dioxide*, J. Geophysical Res. v. 86. pp. 498-502. https://doi.org/10.1029/JC086iC01p00498

Charney, J. G.; A. Arakawa, D. J. Baker, B. Bolin, R. E. Dickinson, R. M. Goody, C. E. Leith, H. M. Stommel and C. I. Wunsch, 1979: *Carbon Dioxide and Climate: A Scientific Assessment*, Report of an ad hoc study group on carbon dioxide and climate, Woods Hole, MA July 23-27. https://geosci.uchicago.edu/~archer/warming_papers/charney.1979.report.pdf

Clark, R., 2023: *Time dependent energy transfer: The forgotten legacy of Joseph Fourier*, Science of Climate Change v. 3, no. 4, pp. 1-24. https://scienceofclimatechange.org/roy-clark-time-dependent-energy-transfer/

Clark, R., 2013a: *A dynamic, coupled thermal reservoir approach to atmospheric energy transfer Part I: Concepts,* Energy and Environment, v. 24, nos. 3-4, pp. 319-340. https://doi.org/10.1260/0958-305X.24.3-4.319

Clark, R., 2013b: *A dynamic, coupled thermal reservoir approach to atmospheric energy transfer Part II: Applications*, Energy and Environment, v. 24, nos. 3-4 pp. 341-359. https://doi.org/10.1260/0958-305X.24.3-4.341

Clark, R. and A. Rörsch, 2023: *Finding Simplicity in a Complex World - The Role of the Diurnal Temperature Cycle in Climate Energy Transfer and Climate Change*, Clark Rörsch Publications, Thousand Oaks, CA. Further details and supplementary material are available at: https://clarkrorschpublication.com/index.html

D'Aleo J. and A. Watts, 2010: *Surface temperature records: policy driven deception?* Aug. 27, http://scienceandpublicpolicy.org/images/stories/papers/originals/surface_temp.pdf (Link not working) Available at: https://venturaphotonics.com/files/6.0_D'Aaleo.Watts.Surface_temp.SPPC%202010.pdf

Donlon, C. J., P. J. Minnet, C. Gentemann, T. J. Nightingale, I. J. Barton, B. Ward and M. J. Murray, 2004: *Towards improved validation of satellite sea surface skin temperature measurements for climate research*, J. Climate v. 15, no. 4, pp. 353-369. https://doi.org/10.1175/1520-0442(2002)015<0353:TIVOSS>2.0.CO;2

Douglas, J. H., 1975: *Climate change: chilling possibilities*, Science News, March 1, v. 107, pp. 138-140. https://www.sciencenews.org/wp-content/uploads/2008/10/8983.pdf

Essex, C.; R. McKitrick and B. Andresen, 2007: *Does a global temperature exist?* J. Non-Equilibrium Thermodynamics, v. 32, no. 1, pp. 1-27. https://doi.org/10.1515/JNETDY.2007.001

Also available at: http://www.rossmckitrick.com/uploads/4/8/0/8/4808045/globtemp.jnet.pdf

Feldman D.R., K. N. Liou, R. L. Shia and Y. L. Yung, 2008: *On the information content of the thermal IR cooling rate profile from satellite instrument measurements*, J. Geophys. Res., v. 113, D1118, pp. 1-14. https://doi.org/10.1029/2007JD009041

Foley, J. C., 1947: *A study of meteorological conditions associated with bush and grass fires and fire protection strategy in Australia,* BOM Bulletin 38, 238 pp. https://nla.gov.au/nla.obj-257165724/view?partId=nla.obj-257176204#page/n4/mode/1up

Folland, C. K.; T. N. Palmer and D. E. Parker, 1986: *Sahel rainfall and worldwide sea temperatures*, Nature, v. 320, pp. 602-606. https://doi.org/10.1038/320602a0

Fourier, J.-B. J., 1824: *Remarques générales sur les températures du globe terrestre et des espaces planétaires*, Annales de Chimie et de Physique, v. 27, pp. 136–167. https://gallica.bnf.fr/ark:/12148/bpt6k65708960/f142.image# English translation: http://fourier1824.geologist-1011.mobi/

Gates, W. L., 1992: AMIP: *The Atmospheric Model Intercomparison Project,* Bull. Amer. Met Soc. v. 73, no. 12, pp. 1962-1970. https://doi.org/10.1175/1520-0477(1992)073<1962:ATAMIP>2.0.CO;2

Gentemann, C. L. F. J. Wentz, C. A. Mears and D. K. Smith, 2004: *In situ validation of Tropical Rainfall Measuring Mission microwave sea surface temperatures*, J. Geophysical Research v. 109, no. C04021, pp. 1-9. https://doi.org/10.1029/2003JC002092

Gibert, F.; J. Cuesta, J.-I. Yano, N. Arnault and P. H. Flamant, 2007: *On the Correlation between Convective Plume Updrafts and Downdrafts, Lidar Reflectivity and Depolarization Ratio*, Boundary Layer Meteorology, v. 5, pp. 553-573. https://doi.org/10.1007/s10546-007-9205-6

Gray, S. T., L. J. Graumlich, J. L. Betancourt and G. T. Pederson, 2004a: *A tree-ring based reconstruction of the Atlantic Multi-decadal Oscillation since 1567 A.D.*, Geophys. Res. Letts., v.

31, L12205, pp. 1-4. https://doi.org/10.1029/2004GL019932

Gray, S. T., L. J. Graumlich, J. L. Betancourt and G. T. Pederson, 2004b: *Atlantic Multi-decadal Oscillation (AMO) Index Reconstruction,* IGBP PAGES/World Data, Center for Paleoclimatology, Data Contribution Series #2004-062, NOAA/NGDC Paleoclimatology Program, Boulder CO, USA. https://www.ncei.noaa.gov/pub/data/paleo/treering/reconstructions/amo-gray2004.txt

HadCRUT4, 2022: *HadCRUT4 Data Series*, https://www.metoffice.gov.uk/hadobs/hadcrut4/data/current/time_series/HadCRUT.4.6.0.0.annual_ns_avg.txt

Hale, G. M. and M. R. Querry, 1973: *Optical constants of water in the 200 nm to 200 µm wavelength region*, Applied Optics, v. 12, no. 3, pp. 555-563. https://doi.org/10.1364/AO.12.000555

Hanel, R. A., B. Schlachman, D. Rogers and D. Vanous, 1971: *Nimbus 4 Michelson Interferometer*, Applied Optics v. 10, no. 6, pp. 1376-1382. https://doi.org/10.1364/AO.10.001376

Hansen, J. et al., (45 authors), 2005: *Efficacy of climate forcings*, J. Geophys. Research, v. 110, D18104, pp.1-45. https://pubs.giss.nasa.gov/docs/2005/2005_Hansen_ha01110v.pdf

Hansen, J., D. Johnson, A. Lacis, S. Lebedeff, P. Lee, D. Rind and G. Russell, 1981: *Climate impact of increasing carbon dioxide*, Science, v. 213, pp. 957-956. https://pubs.giss.nasa.gov/docs/1981/1981_Hansen_ha04600x.pdf

Hansen, J.; A. Lacis, D. Rind, G. Russell, P. Stone, I. Fung, R. Ruedy and J. Lerner, 1984: *Climate sensitivity: analysis of feedback mechanisms*, in *Climate Processes and Climate Sensitivity*, Geophysical Monograph 29, Maurice Ewing Volume 5, pp. 130-163, American Geophysical Union. https://doi.org/10.1029/GM029p0130

Hansen, J. R. Ruedy, A. Lacis, M. Sato, L. Nazarenko, N. Tausnev, I. Tegen and D. Koch, 2000: *Climate modeling in the global warming debate*, in Randall, D. A. (Ed.), *General Circulation Model Development*, International Geophysics Series, v. 70, Chapter 4, Academic Press, San Diego. https://vdoc.pub/documents/general-circulation-model-development-past-present-and-future-5ki27rscn990 Available at: https://venturaphotonics.com/files/7.0_Randall_Hansen.Chap.4.GISS1.pdf

Hansen, K., 2024: *Rising Maximum Temperatures*, Watts Up with That, Jan. 5. https://wattsupwiththat.com/2024/01/05/rising-maximum-temperatures/

Harde, H., 2017: *Radiation Transfer Calculations and Assessment of Global Warming by CO_2*, Int. J. Atmos. Sci., 9251034, pp. 1-30. https://doi.org/10.1155/2017/9251034

Harde, H., 2014: *Advanced two-layer climate model for the assessment of global warming by CO_2*, Open J. Atmos. and Climate Change, v. 1, no. 3, pp 1-50. http://hharde.de/index_htm_files/Harde-ACC-V1N3-001.pdf

Harper, K. C., 2004: *The Scandinavian tag team: Providers of atmospheric reality to numerical weather prediction efforts in the U. S. (1948-1955)*, Proc. Int. Commission on History of Meteorology, v. 1, no. 1, pp. 84-91. https://journal.meteohistory.org/index.php/hom/issue/view/2

Hausfather, Z., 2019: *CMIP6: The next generation of climate models explained*, Carbon Brief, Dec. 2. https://www.carbonbrief.org/cmip6-the-next-generation-of-climate-models-explained

Hays, J. D., J. Imbrie, and N. J. Shackleton, 1976: *Variations in the Earth's Orbit: Pacemaker of the Ice Ages*, Science, v. 194, pp 1121-1132. https://www.science.org/doi/10.1126/science.194.4270.1121

Herring, S. C., N. Christidis, A. Hoell and P. A. Stott, 2022: *Explaining Extreme Events of 2020 from a Climate Perspective* Bull. Amer. Meteor. Soc., v. 101, no. 1, pp. S1–S128. https://doi.org/10.1175/BAMS-ExplainingExtremeEvents2020.1 (and prior years in this series)

Humlum, O., 2024: *Greenhouse Gases, Atmospheric carbon dioxide (CO_2)*, Climate4you. http://www.climate4you.com/

Humlum, O.; K. Stordahl and J-E Solheim, 2013: *The phase relation between atmospheric CO_2*

and global temperature, Global and Planetary Change, v. 100, pp. 51-69. http://dx.doi.org/10.1016/j.gloplacha.2012.08.008

Iacono, M. J., J. S. Delamere, E. J. Mlawer, M. W. Shephard, S. A. Clough, and W. D. Collins, 2008: *Radiative forcing by long-lived greenhouse gases: Calculations with the AER radiative transfer models*, J. Geophys. Res., v. 113, D13103 pp. 1-8. https://doi.org/10.1029/2008JD009944

Idso, C. D., R. M. Carter and S. F. Singer (Eds), 2013: *Climate Change Reconsidered II: Physical Science*, Chicago Il. The Heartland Institute http://climatechangereconsidered.org/climate-change-reconsidered-ii-physical-science/

Imbrie, J. and K. P. Imbrie, 1979: *Ice Ages: Solving the Mystery*, Harvard University Press, Cambridge, Mass.

IPCC AR6, 2021: Masson-Delmotte, V., P. Zhai, A. Pirani, S.L. Connors, C. Péan, S. Berger, N. Caud, Y. Chen, L. Goldfarb, M.I. Gomis, M. Huang, K. Leitzell, E. Lonnoy, J.B.R. Matthews, T.K. Maycock, T. Waterfield, O. Yelekçi, R. Yu, and B. Zhou (eds.), *Climate Change 2021: The Physical Science Basis. Contribution of Working Group I to the Sixth Assessment Report of the Intergovernmental Panel on Climate Change*. Cambridge University Press, Cambridge, United Kingdom and New York, NY, USA. Chapter 7, pp. 923-1054. doi: 10.1017/9781009157896.009, https://www.ipcc.ch/report/ar6/wg1/

IPCC, AR5*, 2013:* Stocker, T.F., D. Qin, G.-K. Plattner, M. Tignor, S.K. Allen, J. Boschung, A. Nauels, Y. Xia, V. Bex and P.M. Midgley (eds.). *Climate Change 2013: The Physical Science Basis. Contribution of Working Group I to the Fifth Assessment Report of the Intergovernmental Panel on Climate Change,* Cambridge University Press, Cambridge, United Kingdom and New York, NY, USA, (2014)1535 pp. ISBN 9781107661820. https://www.ipcc.ch/report/ar5/wg1/

IPCC, AR4, 2007: Solomon, S., D. Qin, M. Manning, Z. Chen, M. Marquis, K. B. Averyt, M. Tignor and H. L. Miller (eds.), *Climate Change 2007: The Physical Science Basis. Contribution of Working Group I to the Fourth Assessment Report of the Intergovernmental Panel on Climate Change,* Cambridge University Press, Cambridge, United Kingdom and New York, NY, USA. https://www.ipcc.ch/report/ar4/wg1/

IPCC, TAR, 2001: Houghton, J.T., Y. Ding, D.J. Griggs, M. Noguer, P.J. van der Linden, X. Dai, K. Maskell, and C.A. Johnson (eds.), *Climate Change 2001: The Scientific Basis. Contribution of Working Group I to the Third Assessment Report of the Intergovernmental Panel on Climate Change*, Cambridge University Press, Cambridge, United Kingdom and New York, NY, USA, 881 pp. https://www.ipcc.ch/site/assets/uploads/2018/03/WGI_TAR_full_report.pdf

IPCC, SAR, 1995: Houghton, J. T.; L.G. Meira Filho, B.A. Callander, N. Harris, A. Kattenberg and K. Maskell (Eds), *Climate Change 1995, The Science of Climate Change*, Cambridge University Press, Cambridge, 1996. https://www.ipcc.ch/site/assets/uploads/2018/02/ipcc_sar_wg_I_full_report.pdf

IPCC FAR, 1990: Houghton, J. T., G. J. Jenkins and J. J. Ephraums (Eds.), *Climate Change, The IPCC Scientific Assessment*, Cambridge University Press, New York. https://www.ipcc.ch/site/assets/uploads/2018/03/ipcc_far_wg_I_full_report.pdf

Jaworowski, Z., 2007: *CO_2: The greatest scientific scandal of our time*, Executive Intelligence Review (EIR) Science, v. 34, no. 11, March 16. https://www.larouchepub.com/eiw/public/2007/eirv34n11-20070316/38_711_science.pdf

Jones, P. D., T. M. L. Wigley, C. K. Foland, D. E. Parker, J. K. Angell, S. Lebedeff and J. E. Hansen, 1988: *Evidence for global warming in the past decade*, Nature, v. 332, p. 790. https://doi.org/10.1038/332790b0

Jones, P. D., T. M. Wigley and P. B Wright, 1986: *Global temperature variations between 1861 and 1984*, Nature, v. 323, no.31, pp. 430-434. https://www.nature.com/articles/322430a0

Kandel, R. and M. Viollier, (2010): *Observation of the Earth's radiation budget from space,* Comptes Rendus Geoscience, v. 342, no. 4-5, pp. 286-300. https://doi.org/10.1016/j.crte.2010.01.005

Keeling, 2023: *The Keeling Curve*. https://scripps.ucsd.edu/programs/keelingcurve/

Knutti, R. and G. C. Hegerl, 2008: *The equilibrium sensitivity of the Earth's temperature to radiation changes*, Nature Geoscience, v. 1, pp. 735-743. https://www.nature.com/articles/ngeo337

Koll, D. D. B and T. W. Cronin, 2018: *Earth's outgoing longwave radiation linear due to* H_2O *greenhouse effect*, *PNAS*, v. 115, no. 41, pp. 10293-10298. https://www.pnas.org/doi/10.1073/pnas.1809868115

Kottek, M., J. Grieser, C. Beck, B. Rudolf and F. Rubel, June 2006: *World Map of the Köppen-Geiger climate classification updated*, Meteorologische Zeitschrift, v. 15, no. 3, pp. 259-263. https://w2.weather.gov/media/jetstream/global/Koppen-Geiger.pdf

Koutsoyiannis, D., 2024: *Net Isotopic Signature of Atmospheric* CO_2 *Sources and Sinks: No Change since the Little Ice Age*, Sci V. 6, 17 pp. 1-27. https://doi.org/10.3390/sci6010017

Lettau, H. H. and B. Davidson, 1957: *Exploring the Atmosphere's First Mile. Proceedings of the Great Plains Turbulence Field Program, 1 August to 8 September 1953* Volume II, Site Description and Data Tabulation, Oxford, Pergamon Press. Available at: https://books.google.com/books?hl=en&lr=&id=5bcJAQAAIAAJ&oi=fnd&pg=PA377&dq=Lettau,+H.H.+and+B.+Davidson,+Exploring+the+atmosphere%E2%80%99s+first+mile.+Oxford:+Pergamon+Press,+1957.&ots=N0vbpjURx3&sig=sSTz9EMWpwi0XysXHTcWcLNxWv0#v=onepage&q&f=false

Lewis, N. and J. Curry, 2018: *The Impact of Recent Forcing and Ocean Heat Uptake Data on Estimates of Climate Sensitivity*, J. Climate, v. 31, pp. 6051-6070. https://journals.ametsoc.org/view/journals/clim/31/15/jcli-d-17-0667.1.xml

Lindzen, R., 2024: *What is Climate?* Watts Up with That, Jan. 20. https://wattsupwiththat.com/2024/01/20/what-is-climate-richard-lindzen/

Lorenz, E. N., 1973: *On the Existence of Extended Range Predictability* J. Applied Meteorology and Climatology, v. 12, no. 3, pp. 543-546. https://journals.ametsoc.org/view/journals/apme/12/3/1520-0450_1973_012_0543_oteoer_2_0_co_2.xml?tab_body=fulltext-display

Lorenz, E.N., 1963: *Deterministic nonperiodic flow*, Journal of the Atmospheric Sciences, v. 20, no. 2, pp. 130-141. https://journals.ametsoc.org/view/journals/atsc/20/2/1520-0469_1963_020_0130_dnf_2_0_co_2.xml

MacCracken, M. C. and F. M. Luther (Eds.), 1985: *Detecting the climatic effects of increasing carbon dioxide*, US Department of Energy Report DOE/ER-0235. https://doi.org/10.2172/6264945

MacCracken, M. C. and F. M. Luther (Eds.), 1985: *Projecting the climatic effects of increasing carbon dioxide* US Department of Energy Report DOE/ER-0237. https://doi.org/10.2172/5885458

Manabe, S. and F. Möller, 1961: *On the radiative equilibrium and heat balance of the atmosphere*, Monthly Weather Review, v. 89, no. 12, pp. 503-532. https://doi.org/10.1175/1520-0493(1961)089<0503:OTREAH>2.0.CO;2

Manabe, S. and R. J. Stouffer, 1980: *Sensitivity of a global climate model to an increase of* CO_2 *concentration in the atmosphere*, J. Geophys Res., v. 85, no. C10, pp. 5529-5554. https://doi.org/10.1029/JC085iC10p05529]

Manabe, S. and R. J. Stouffer, 1979: *A* CO_2*-climate sensitivity study with a mathematical model of the global climate*, Nature, v. 282, pp. 491-493.

https://www.nature.com/articles/282491a0.pdf

Manabe, S. and R. F. Strickler, 1964: *Thermal Equilibrium of the Atmosphere with a Convective Adjustment*, J. Atmospheric Sciences, v. 21, pp. 361-385. https://climate-dynamics.org/wp-content/uploads/2016/06/manabe64a.pdf

Manabe, S. and R. T. Wetherald, 1975: *The effects of doubling the CO_2 concentration in the climate of a general circulation model*, J. Atmos. Sci., v. 32, no. 1, pp. 3-15. https://journals.ametsoc.org/view/journals/atsc/32/1/1520-0469_1975_032_0003_teodtc_2_0_co_2.xml?tab_body=pdf

Manabe, S. and R. T. Wetherald, 1967: *Thermal equilibrium of the atmosphere with a given distribution of relative humidity*, J. Atmos. Sci., v. 24, pp. 241-249. http://www.gfdl.noaa.gov/bibliography/related_files/sm6701.pdf

Mass, C., 2022: *The Colorado Wildfire and Global Warming: Is there a Connection?* Watts Up with That, Jan. 6. https://wattsupwiththat.com/2022/01/06/the-colorado-wildfire-and-global-warming-is-there-a-connection/

Math, F. A., Feb. 1934: *Battle of the chinook wind at Havre, Mont.*, Monthly Weather Review, pp 54-57. https://doi.org/10.1175/1520-0493(1934)62<54:BOTCWA>2.0.CO;2

McFarlane, F., 2018: *The 1970s Global Cooling Consensus was not a Myth*, Watts Up With That, Nov. 19. https://wattsupwiththat.com/2018/11/19/the-1970s-global-cooling-consensus-was-not-a-myth/

Mearns, E., 2017: *The Vostok Ice Core and the 14,000 Year CO_2 Time Lag*, Energy Matters, June 14. http://euanmearns.com/the-vostok-ice-core-and-the-14000-year-co2-time-lag/

Meehl, G. A., G. J. Boer, C. Covey, M. Latif and R. J. Stouffer, 1997: *Intercomparison Makes for a Better Climate Model*, Eos, v. 78, no. 41, pp. 445-451 October 14. https://doi.org/10.1029/97EO00276

Meehl, G. A.; C. Covey, T. Delworth, M. Latif, B. McAvaney, J. F. B. Mitchell, R. J. Stouffer and K. E. Taylor, 2007: *The WCRP CMIP3 Multimodel Dataset: A New Era in Climate Change Research*, Bull. Amer. Met. Soc., v. 88, no. 9, pp. 1383-1394. https://doi.org/10.1175/BAMS-88-9-1383

Messiah, A., 1999: *Quantum Mechanics*, Chapter IV, Dover Publications Inc., Mineola, NY.

Milankovitch Cycles, 2022: Wikipedia. https://en.wikipedia.org/wiki/Milankovitch_cycles

MODTRAN, 2024: *Infrared Atmospheric Radiation Code*. https://climatemodels.uchicago.edu/modtran/

Monckton, C, July 2008: *Climate Sensitivity Reconsidered*, Physics and Society, v. 37, no.3, pp. 5-19. https://engage.aps.org/fps/resources/newsletters/newsletter-archives/july-2008

Morice, C. P., J. J. Kennedy,N. A. Rayner and P. D. Jones, 2012: *Quantifying uncertainties in global and regional temperature change using an ensemble of observational estimates: The HadCRUT4 data set*, J. Geophysical Res. Atmospheres, v. 117, D08101, pp. 1-22. https://doi.org/10.1029/2011JD017187

NASA, 2017: *Smoke and fire in S. California*, Earth Oservatory, Terra-MODIS Satellite Image, Dec. 5, 2017. https://earthobservatory.nasa.gov/images/91379/smoke-and-fire-in-southern-california

NOAA, 2023: *Koppen-Geiger climate classifiation map*. https://www.noaa.gov/jetstream/global/climate-zones/jetstream-max-addition-k-ppen-geiger-climate-subdivisions

NRL, 2021: Naval Research Laboratory, HYCOM consortium for Data-Assimilative Ocean Modeling. https://www7320.nrlssc.navy.mil/GLBhycomcice1-12/

O'Neill, P., R. Connolly, M. Connolly, Willie Soon, B. Chimani, M. Crok, R. de Vos, H. Harde,

P. Kajaba, P. Nojarov, R. Przybylak, D. Rasol, O. Skrynyk, O. SkrynykP. Štěpánek, A. Wypych and P. Zahradníček, 2022: *Evaluation of the Homogenization Adjustments Applied to European Temperature Records in the Global Historical Climatology Network Dataset*, Atmosphere, v. 13, no. 2, 285, pp. 1-21. https://doi.org/10.3390/atmos13020285

Oke T. R., 2006: *Initial guidance to obtain representative meteorological observations at urban sites*, Instruments and Observing Methods, Report No. 81, WMO/TD-No. 1250, World Meteorological Association, pp. 47. https://www.researchgate.net/publication/265347633_Initial_guidance_to_obtain_representative_meteorological_observations_at_urban_sites

Otto, A., F. E. L. Otto, O. Boucher, J. Church, G. Hegerl, P. M. Forster, N. P. Gillett, J. Gregory, G. C. Johnson, R Knutti, N. Lewis, U. Lohmann, J. Marotzke, G. Myhre, D. Shindell, B. Stevens and M. R. Allen, 2013: *Energy budget constraints on climate response*, Nature Geoscience, v. 6 no. 6, pp. 415-416. ISSN 1752-0894. http://eprints.whiterose.ac.uk/76064/7/ngeo1836(1)_with_coversheet.pdf

Otto Ibid, Supplementary Material. https://static-content.springer.com/esm/art%3A10.1038%2Fngeo1836/MediaObjects/41561_2013_BFngeo1836_MOESM299_ESM.pdf

PDO, 2022: *Pacific Decadal Oscillation*. https://www.ncdc.noaa.gov/teleconnections/pdo/

Peterson, T. C., W. M. Connolley and J. Fleck, 2008: *The myth of the 1970's global cooling consensus*, Bull. Amer. Meteor. Soc., v. 86, pp. 1325-1337. https://doi.org/10.1175/2008BAMS2370.1

Plass, G. N., 1956a: *The influence of the 15-micron carbon dioxide band on the atmospheric infrared cooling rate*, Quarterly Journal of the Royal Meteorological Society, v. 82, pp. 310-324. https://doi.org/10.1002/qj.49708235307 Available at: http://www.rescuethatfrog.com/wp-content/uploads/2017/02/Plass-1956c.pdf

Plass, G.N., 1956b: *The Carbon Dioxide Theory of Climatic Change*, Tellus, v. 8, no. 2, pp. 140-154. https://onlinelibrary.wiley.com/doi/abs/10.1111/j.2153-3490.1956.tb01206.x

Pouillet, M., 1837: *Memoir on the solar heat, on the radiating and absorbing powers of the atmospheric air and on the temperature of space.* In: Scientific Memoirs selected from the Transactions of Foreign Academies of Science and Learned Societies, edited by Richard Taylor, v. 4, pp. 44-90. http://nsdl.library.cornell.edu/websites/wiki/index.php/PALE_ClassicArticles/archives/classic_articles/issue1_global_warming/n2-Poulliet_1837corrected.pdf

Original publication, 1836: *Mémoire sur la chaleur solaire: sur les pouvoirs rayonnants et absorbants de l'air atmosphérique et sur la température de l'espace,* Comptes Rendus des Séances de l'Académie des Sciences, Paris. v. 7, pp. 24-65.

Quayle, R. G.; D. R. Easterling, T. R. Karl and P. Y. Hughes, 1991: *Effects of recent thermometer changes in the cooperative station network*, Bull Amer Met Soc., v. 72, no.11, pp. 1718-1723. https://doi.org/10.1175/1520-0477(1991)072<1718:EORTCI>2.0.CO;2

Ramanathan, V. 1975: *Greenhouse effect due to chlorofluorocarbons: Climatic implications*, Science, v. 190, pp. 50-52. https://www.science.org/doi/abs/10.1126/science.190.4209.50

Ramanathan, V. and W. Collins, 1991: *Thermodynamic regulation of ocean warming by cirrus clouds deduced from observations of the 1987 El Niño*, Nature, v. 351, pp. 27–32. https://doi.org/10.1038/351027a0

Ramaswamy, V., W. Collins, J. Haywood, J. Lean, N. Mahowald, G. Myhre, V. Naik, K. P. Shine, B. Soden, G. Stenchikov and T. Storelvmo, 2019: *Radiative Forcing of Climate: The Historical Evolution of the Radiative Forcing Concept, the Forcing Agents and their Quantification, and Applications* Meteorological Monographs v. 59, Chapter 14. https://doi.org/10.1175/AMSMONOGRAPHS-D-19-0001.1

Rasool, S. I. and S. H. Schneider, 1971: *Atmospheric carbon dioxide and aerosols: Effects of large increases on global climate*, Science, v. 173, pp 138-141. https://www.science.org/doi/10.1126/science.173.3992.138

Raval, A. and V. Ramanathan, 1989: *Observational determination of the greenhouse effect*, Nature, v. 342 pp. 758-761. https://doi.org/10.1038/342758a0

Revelle, R. and H. E. Suess, 1957: *Carbon dioxide exchange between atmosphere and ocean and the question of an increase of atmospheric CO_2 during the past decades*, Tellus v. 9, pp. 18-27. https://doi.org/10.3402/tellusa.v9i1.9075

Riches, M. R. and F. A. Koomanoff, 1985: *Overview of the Department of Energy Carbon Dioxide Research Program*, Bull. Amer. Met. Soc., v. 66, no. 2, pp. 152-158. https://doi.org/10.1175/1520-0477(1985)066<0152:OOTDOE>2.0.CO;2

Salby, M. and H. Harde, 2022a: *What causes increasing greenhouse gases? Summary of a Trilogy*, Science of Climate Change, v. 2, no. 3 pp. 297-301. https://doi.org/10.53234/scc202212/16

Salby, M. and H. Harde, 2022b: *Theory of increasing greenhouse gases*, Science of ClimateChange, Vol. 2, No. 3, pp. 212-238, https://doi.org/10.53234/scc202212/17.

Salby, M. and H. Harde, 2021a: *Control of atmospheric CO2 - Part I: Relation of carbon 14 to the removal of CO_2*, Science Climate Change, v. 1, no. 2, pp. 177-195. https://doi.org/10.53234/scc202112/30.

Salby, M. and H. Harde, 2021b: *Control of Atmospheric CO_2 - Part II: Influence of Tropical Warming*, Science of Climate Change, v. 1, no.2, pp. 196-212. https://doi.org/10.53234/scc202112/12.

Schwendike, J., G. J. Berry, K. Fodor, M. J. Reeder, 2021: *On the Relationship Between the Madden-Julian Oscillation and the Hadley and Walker Circulations*, JGR Atmospheres, v. 126, no. 4, 10.1029/2019JD032117, pp. 1-28. https://doi.org/10.1029/2019JD032117

Shaman, J., R. M. Samelson and E. Skyllingstad, 2010: *Air–Sea Fluxes over the Gulf Stream Region: Atmospheric Controls and Trends*, J. Climate v. 23, no. 10, pp. 2651-2670. https://doi.org/10.1175/2010JCLI3269.1

Soden, B. J. and I. M. Held, 2006: *An assessment of climate feedbacks in coupled ocean-atmosphere models*, J. Climate, v. 19, pp. 3354-3360. https://doi.org/10.1175/JCLI3799.1

SOI, 2022: *Southern Oscillation Index* http://www.bom.gov.au/climate/enso/soi/

Stone, H. M. and S. Manabe, 1968: *Comparison among various numerical models designed for computing IR cooling*, Monthly Weather Review, v. 96, no. 10, pp 735-741. https://doi.org/10.1175/1520-0493(1968)096<0735:CAVNMD>2.0.CO;2

Stott, P.A., S.F.B. Tett, G.S. Jones, M.R. Allen, J.F.B.Mitchell and G.J. Jenkins, 2000: *External control of twentieth century temperature variations by natural and anthropogenic forcings*, Science, v. 290, pp. 2133-2137. https://www.science.org/doi/abs/10.1126/science.290.5499.2133

Stouffer, R. J., V. Eyring, G. A. Meehl, S. Bony, C. Senior, B. Steven, S, and K. E. Taylor, 2017: *CMIP5 scientific gaps and recommendations for CMIP6*, Bull. Amer. Met. Soc., v. 98, no.1, pp. 95-105. https://journals.ametsoc.org/doi/pdf/10.1175/BAMS-D-15-00013.1

Taylor, K. E., R. J. Stauffer and G. A. Meehl, 2012: *An overview of the CMIP5 and the experimental design*, Bull. Amer. Met. Soc., v. 93, no. 4, pp. 485-498. https://doi.org/10.1175/BAMS-D-11-00094.1

Terando, A., D. Reidmiller, S. W. Hostetler, J. S. Littell, T. D. Beard, Jr., S. R. Weiskopf, J. Belnap and G. S. Plumlee, 2020: *Using information from global climate models to inform policymaking—The role of the U.S. Geological Survey*, U.S. Geological Survey Open-File Report 2020–1058, 25 pp. https://doi.org/10.3133/ofr20201058

Tett, S.F.B., G.S. Jones, P.A. Stott, D.C. Hill, J.F.B. Mitchell, M.R. Allen, W.J. Ingram, T.C.

Johns, C.E. Johnson, A. Jones, D.L. Roberts, D.M.H. Sexton and M.J. Woodage, 2000: *Estimation of natural and anthropogenic contributions to 20th century temperature change*, Hadley Centre Tech Note 19, pp 52, Hadley Centre for Climate Prediction and Response, Meteorological Office, RG12 2SY, UK., https://adsabs.harvard.edu/full/2000ESASP.463..201T/0000201.000.html

TRITON, 2024: *TRITON Buoy Data*. https://www.pmel.noaa.gov/tao/drupal/disdel/

Tyndall, J., 1861: *On the Absorption and Radiation of Heat by Gases and Vapours, and on the Physical Connexion of Radiation, Absorption, and Conduction*, Philosophical Transactions of the Royal Society of London, v. 151, pp. 1-36. https://royalsocietypublishing.org/doi/pdf/10.1098/rstl.1861.0001

Tyndall, J., 1863: *On radiation through the Earth's atmosphere*, Proc. Roy. Inst., Jan 23, pp. 200-206.

UAH, 2022: *tlt temperature series*, University of Alabama, Huntsville. https://www.nsstc.uah.edu/data/msu/v6.0/tlt/uahncdc_lt_6.0.txt

Vinos, J., 2022: *Climate of the past, present and future*, Critical Science Press, Madrid. https://www.researchgate.net/profile/Javier-Vinos/publication/363669186_Climate_of_the_Past_Present_and_Future_A_scientific_debate_2nd_ed/links/63296077071ea12e36487da9/Climate-of-the-Past-Present-and-Future-A-scientific-debate-2nd-ed.pdf

Wagner, F.; B. Aaby and H. Visscher, 2002: *Rapid atmospheric CO_2 changes associated with the 8,200-years-B.P. cooling event*, PNAS, v. 99, no.19, pp. 12011-12014. https://doi.org/10.1073/pnas.182420699

Wang, W. C. and G. A. Domoto, 1974: *The radiative effect of aerosols on the earth's atmosphere*, J. Appl. Meteorology, v. 13, no. 5, pp. 521-534. https://doi.org/10.1175/1520-0450(1974)013<0521:TREOAI>2.0.CO;2

Wang, W. C., Y. L. Yung, A. A. Lacis, T. Mo and J. E. Hansen, 1976: *Greenhouse effects due to man-made perturbations of trace gases*, Science, v. 194, pp. 685-690. https://pubs.giss.nasa.gov/docs/1976/1976_Wang_wa07100z.pdf

Watts, A., 2021: Media FAIL on reporting the Pacific Northwest Heatwave, Watts Up With That, June 30. https://wattsupwiththat.com/2021/06/30/major-media-fail-on-reporting-the-pacific-northwest-heatwave/

Watts, A., 2020: *Climate Change? Temperature Hits 100 Degrees above Arctic Circle, Just Like 100 Years Ago*, Watts Up with That, July 23. https://wattsupwiththat.com/2020/06/23/climate-change-temperature-hits-100-degrees-above-arctic-circle-just-like-100-years-ago/

Wijngaarden, W. A. van and W. Happer, 2022: *IR Forcing by Greenhouse Gases*, CO_2 Coalition publication, June 10. https://co2coalition.org/wp-content/uploads/2022/03/Infrared-Forcing-by-Greenhouse-Gases-2019-Revised-3-7-2022.pdf

WRCC, 2022: *Western Region Climate Center*. https://wrcc.dri.edu/sod/arch/hbF.html

Yu, L., (2007): *Global variations in oceanic evaporation (1958-2005): The role of the changing wind speed*, J. Climate v. 20, no. 21, pp. 5376-5390. https://doi.org/10.1175/2007JCLI1714.1

Yu, L., X. Jin, and R.A. Weller, Jan. 2008: *Multidecade global flux datasets from the objectively analyzed air-sea fluxes (OAFlux) project: latent and sensible heat fluxes, ocean evaporation, and related surface meteorological variables,* Woods Hole Oceanographic Institution, OAFlux project technical report OA-2008-01, 64 pp. http://apdrc.soest.hawaii.edu/doc/OAFlux_TechReport_3rd_release.pdf

Zachos, J., M. Pagani, L. Sloan, E. Thomas and K. Billups, 2001: *Trends, rhythms and aberrations in the global climate, 65 Ma to present*, Science, v. 292, pp. 86-693. https://www.science.org/doi/abs/10.1126/science.1059412

Zelinka, M. D., T. A. Myers, D. T. McCoy, S. Po-Chedley, P. M. Caldwell, P. Ceppi, S. A. Klein and K. E. Taylor, 2020: *Causes of Higher Climate Sensitivity in CMIP6 Models*, Geophysical Research Letters, v. 47, e2019GL085782, pp. 1-12. https://agupubs.onlinelibrary.wiley.com/doi/pdf/10.1029/2019GL085782